Contents

1 Ultra-relativistic heavy ion collisions and the formation of Quark-Gluon Plasma (QGP) 1

1.1 Introduction . . . 1
1.2 Geometry and kinematics . . . 2
1.3 Transverse Energy distribution and estimate of Energy Density . . . 3
1.4 Baryon content . . . 6
1.5 Temperature . . . 7
1.6 Global features: summary . . . 7
1.7 Space-time evolution and Signatures of QGP . . . 7
1.8 J/Ψ Suppression . . . 9
1.9 J/Ψ Production mechanism . . . 12

2 The NA50 Experiment 16

2.1 The muon spectrometer . . . 16
2.2 The trigger hodoscopes . . . 17
2.3 The proportional wire chambers . . . 19
2.4 The absorber . . . 20
2.5 The active target . . . 21
2.6 Centrality detectors . . . 23
2.6.1 The electromagnetic calorimeter . . . 23
2.6.2 The zero–degree calorimeter . . . 24
2.6.3 The multiplicity detector . . . 25
2.7 NA50 beam line . . . 25
2.7.1 The beam hodoscope . . . 25
2.8 Trigger selection . . . 26
2.9 DAQ system and data recording . . . 26

3 The NA50 multiplicity detector 30

3.1 Introduction . . . 30
3.2 MD components . . . 34
3.3 The Silicon Microstrip Detectors . . . 34
3.4 The Front–end VLSI circuits . . . 36
3.4.1 The FABRIC . . . 37

3.4.2 The CDP . . . 40
3.5 The BOARDs . . . 41
3.6 The auxiliary boards and cables . . . 45
3.6.1 The EXTCARD . . . 46
3.7 Front–End Control Modules . . . 48
3.7.1 The CCTD module . . . 48
3.7.2 The BUSIF module . . . 51
3.8 Power supply . . . 51
3.9 Data synchronization . . . 53

4 Laboratory tests on MD components **57**
4.1 Introduction . . . 57
4.2 Test of detectors . . . 57
4.3 Test of front-end chips . . . 58
4.3.1 Testing FABRICs . . . 58
4.3.2 FABRIC Mass tests . . . 60
4.3.3 Testing CDPs . . . 61
4.3.4 CDP mass tests . . . 62
4.4 Test of BOARDs . . . 62
4.5 Assembling and testing of BOARDs . . . 63
4.6 Final assembly and proton beam tests . . . 64
4.7 Pb–Pb data taking: radiation problems and possible solutions . . . 65
4.7.1 Radiation damage on detectors . . . 66
4.7.2 Radiation damage on digital chips . . . 70

5 The MD data analysis **74**
5.1 Definition of MD global variables . . . 74
5.2 The evaluation of multiplicity . . . 75
5.3 Definition of dead and noisy strips . . . 76
5.4 Definition of MD efficiency ϵ . . . 78
5.4.1 Silicon detectors efficiency . . . 78
5.4.2 Analog chips efficiency . . . 80
5.4.3 Digital chips efficiency . . . 81
5.5 Efficiency corrections . . . 83
5.6 The MD target identification algorithm . . . 85
5.6.1 Corrections for radiation damage . . . 87

6 The MD as a centrality detector: data analysis and results **88**
6.1 Raw Data treatment and event selection . . . 88
6.2 Event selection in centrality bins . . . 89
6.2.1 Centrality selection in E_t bins . . . 90
6.2.2 Centrality selection in multiplicity bins . . . 93
6.3 The dimuon mass spectra analysis . . . 95

6.3.1 Contributions to invariant mass spectrum 96
6.3.2 The fit procedure 101
6.4 Results 102
6.4.1 E_t bins 102
6.4.2 Multiplicity bins 103
6.4.3 Comparison with lighter systems 103
6.5 Conclusions 104

List of Figures

1.1 *Schematic representation of nucleus-nucleus central and pheripheral collisions* . . . 3
1.2 *Cross section measurements $d\sigma/dE_T$ for different targets* . . . 4
1.3 *Fit to the E_T cross section from NA34 data with a geometrical parametrization considering indipendent nucleon-nucleon collisions. For different values of E_T the model gives the number NN of nucleon-nucleon collisions, the number N_p of projectile participants, the impact parameter b and the fraction of the total geometrical cross section σ below a given E_T* . . . 5
1.4 *Sketch of interaction volume in ion-ion collision* . . . 6
1.5 *Space-time diagram for nucleus-nucleus collision, showing the various stages of the evolution of the expanding matter.* . . . 8
1.6 *Drell-Yan mechanism* . . . 10
1.7 *J/Ψ suppression in proton-nucleus and nucleus-nucleus collisions* . . . 12
1.8 *J/Ψ production mechanism through the colour singlet $c\bar{c}$* . . . 13
1.9 *J/Ψ production mechanism through the colour singlet $c\bar{c}g$* . . . 13

2.1 *The muon spectrometer* . . . 17
2.2 *Different views of NA50 magnet* . . . 18
2.3 *Shape of magnetic field* . . . 18
2.4 *The trigger hodoscopes* . . . 19
2.5 *The different dimensions of blades in the first set of hodoscopes* . . . 20
2.6 *The Multi Wires Proportional Chambers* . . . 21
2.7 *The absorber* . . . 22
2.8 *The active target* . . . 23
2.9 *The Zero Degree Calorimeter* . . . 24
2.10 *The NA50 general DAQ system (excluding the MD)* . . . 27

3.1 *Scheme of the NA50 target region* . . . 31
3.2 *Picture of one plane of the Multiplicity Detector* . . . 31
3.3 *Particle hit on the Multiplicity Detector* . . . 32
3.4 *The Multiplicity Detector structure: a) superposition of BOARD1 and BOARD2 to form a complete module, b) different position of the modules on the 2 MD faces* . . . 35

3.5 *Block diagram of the MD read–out chain* . . . 37
3.6 *Scheme of the FABRIC* . . . 38
3.7 *Scheme of a CDP* . . . 40
3.8 *Scheme of a BOARD1* . . . 42
3.9 *Scheme of a BOARD2* . . . 43
3.10 *Schematic drawing of a MD module: BOARD1+BOARD2* . . . 44
3.11 *Scheme of the EXTCARD* . . . 47
3.12 *Scheme of the read–out synchronization* . . . 49
3.13 *Scheme of the CCTD module* . . . 50
3.14 *Scheme of a BUSIF module* . . . 52

4.1 *The behaviour of detector leakage currents along the data taking period* 66
4.2 *The absolute value of effective doping cocentration calculated from depletion voltage as a function of 350 MeV/c pion fluence.* . . . 68

5.1 *Sketch of the possible choice of strips to be used for different pseudo-rapidity ranges on MD1 and MD2* . . . 75
5.2 *Number of dead channels versus threshold value* . . . 77
5.3 *Number of dead strips vs run number* . . . 78
5.4 *Number of noisy channels vs run number* . . . 79
5.5 *Detector bias voltage scans on 2 detectors: occupancy vs bias for different strips, from internal ones (5-65) to outermost ones (85-125)* . . . 80
5.6 *Detector bias voltage scans: depletion voltage vs strip number for different detectors* . . . 81
5.7 *Number of counts for a given group of strips versus threshold value: intergral and differential curves* . . . 81
5.8 *Distribution of multiplicity vs trigger delay for CDP1* . . . 82
5.9 *Hit-maps of two different efficiency sectors* . . . 84
5.10 *Schematic drawing of the MD target identification algorithm geometry* 86
5.11 *Distributions of the target estimator highest value* . . . 87

6.1 *Schematic drawing of the L variable* . . . 89
6.2 *E_t distribution for 1995 data: the white circles correspond to double blade information, the black ones to single blade information* . . . 90
6.3 *E_t vs E_{ZDC} for events with identified target (1996 data)* . . . 91
6.4 *E_t vs E_{ZDC} with the graphic cut (1996 data)* . . . 91
6.5 *E_t distribution for different event selection methods, and ratio between the different curves.* . . . 92
6.6 *Mul2 distribution and bin selection* . . . 93
6.7 Differential cross section versus multiplicity . . . 95
6.8 Impact parameter b versus multiplicity . . . 96
6.9 Simulated impact parameter b versus multiplicity . . . 97
6.10 *Dimuon invariant mass spectrum and the analitical shapes of the different contributions* . . . 98

6.11 *Combinatorial background spectra for the different configurations* . . . 99
6.12 *Example of the fit to a background spectrum* 100
6.13 *Example of the step one fit to the signal distribution* 102
6.14 *Example of the step two fit to the signal distribution* 103
6.15 *Example of the global fit to the signal distribution* 104
6.16 $J/\Psi/DY$ *cross sections versus* E_t 106
6.17 $J/\Psi/DY$ *cross sections versus* N_ch 107
6.18 J/Ψ *width values for different* E_t *bins* 107
6.19 J/Ψ *width values for different* N_{ch} *bins* 108
6.20 *Ratio between* J/Ψ *and DY cross sections,* E_t *bin selection and "banana cut" (open circles) and* E_t *bin selection and NOCIMD cut (black circle), compared to NA38 data* 108
6.21 *Ratio between* J/Ψ *and DY cross sections,* N_{ch} *bin selection and NOCIMD cut (black circle), compared to NA38 data* 109

List of Tables

2.1 The SpS cycles for different beams 25

3.1 Main components of the MD in the target region 33
3.2 Low Voltage channels for the Multiplicity Detector 55

6.1 Multiplicity bins, average multiplicity and different contributions to the signal 94
6.2 E_t bins, average E_t and different contributions to the signal 105

Chapter 1

Ultra-relativistic heavy ion collisions and the formation of Quark-Gluon Plasma (QGP)

1.1 Introduction

According to Quantum Chromodynamics (QCD), a transition from hadronic matter to a plasma of quarks and gluons should occur when nuclear matter is compressed to a sufficiently high density and temperature [1],[2]. The QCD potential, which in vacuum increases linearly with distance giving rise to a strong attractive force that confines quarks and gluons into hadrons, in dense matter goes to zero at large distances and consequently quarks and gluons are free. The condition for the transition from hadronic matter (HM) to the quark-gluon plasma (QGP) is that the density of the constituents is sufficiently high. Naively speaking, it is impossible to define $q\bar{q}$ or qqq as a specific hadron, since in any hadronic volume there are many other possible partners (Satz).

QCD lattice calculations predict this transition and provide estimates for critical values ranging from 140 to 180 MeV for the temperature and $2-3$ GeV/fm^3 for the energy density [3].

The QGP was the state of the matter in the first instants of the Universe (for time $t < 10^{-6}$s after the "big-bang"); it is possible that QGP is present in the core of neutron stars. In the laboratory, QGP can be obtained, as a transient state, by means of very high energy ion-ion collisions.

We are confident to have high energy densities in nucleus-nucleus collisions at high energy because in these interactions the degree of slowing-down (i.e. the stopping power) is quite large. In fact, in a central nucleus-nucleus collision there are many nucleon-nucleon interactions, and it was measured that the fraction of the incident momentum carried out by the outgoing proton has a mean value $< x > \approx 0.6$ in a p-p interaction at 100 GeV/c, therefore 40% of the incident momentum is lost [4].

Relativistic heavy-ion collisions are not the only way in which one can try to observe the QGP, and searches in hadron-hadron collisions are being actively pursued, but signals should be clearer when studying distances which are much larger than a nucleon size. Moreover, they are the only mean to create a strongly interacting system which can be studied in thermodynamical terms. To do so, the system under study has to consist of many particles, so that macroscopic variables can apply, have a size much larger than the mean free path of the constituents ($\approx 0.5 fm$ for quarks at densities of $\approx$ 2 GeV/fm^3), since several collisions per particle must occur, and finally have large energy density. Collisions of nuclei at ultrarelativistic energies have proven to fulfill these conditions: the system created in a Pb-Pb collision has a volume of the order of 1000 fm^3, consists of $\approx$ 1000 particles, shows clear evidence of rescattering (more than one collision/particle) and, at SpS energies, has an energy density $\approx$ 20 times larger than in a nucleus and $\approx$ 4 times larger than in a hadron.

High energy ion beams have been available for experiments since 1986 both at CERN and Brookhaven: ^{16}O and ^{32}S nuclei were accelerated up to a momentum per nucleon of 200 GeV/c at CERN till 1992, while a beam of ^{28}Si at 14.5 GeV/c was available at AGS. Accelerators were upgraded in order to produce heavy ion beams, leading up in 1993 to the gold beam of 12 A·GeV at the AGS and finally in 1995 to the lead beam of 158 A·GeV at the SpS.

1.2 Geometry and kinematics

A schematic picture of a collision between two relativistic nuclei is shown in fig. 1.1. The incoming nuclei are Lorentz-contracted: their transverse size is equal to the nuclear section, while their thickness is $\approx$ 1 fm. Given an impact parameter b, the nucleons can be separated into *participants*, which undergo primary nucleon-nucleon collisions, and *spectators*, which continue along their original direction with modest perturbation. Collisions with $b \approx 0$ are defined *central*. Collisions with $b \approx r_1 + r_2$ are defined *peripheral*.

In the laboratory system most secondary particles are emitted in the forward direction, but spectators and participants are emitted at different angles. While spectators are emitted at angles of the order of 0.5 mrad ($\theta_{spect} \approx p_{Fermi}/p_{beam} \approx$ 100 MeV/200 GeV $\approx$ 0.5 mrad), participants are emitted at larger angles: $\theta_{partic} \approx p_x/p_z \approx 500$ MeV/$\beta\gamma m \approx$ 500 MeV/10 GeV $\approx$ 50 mrad. They can therefore be separated with a detector covering only the very forward direction (ZDC=Zero Degree Calorimeter).

To describe the final state, since secondary particles can be classified as target fragments, beam fragments or particles produced in collisions of the participant nucleons, it is important to define a variable which transforms additively under a Lorentz transformation, because for such a variable the shape of the distribution is invariant going from a reference system to another. This variable is the *rapidity* of

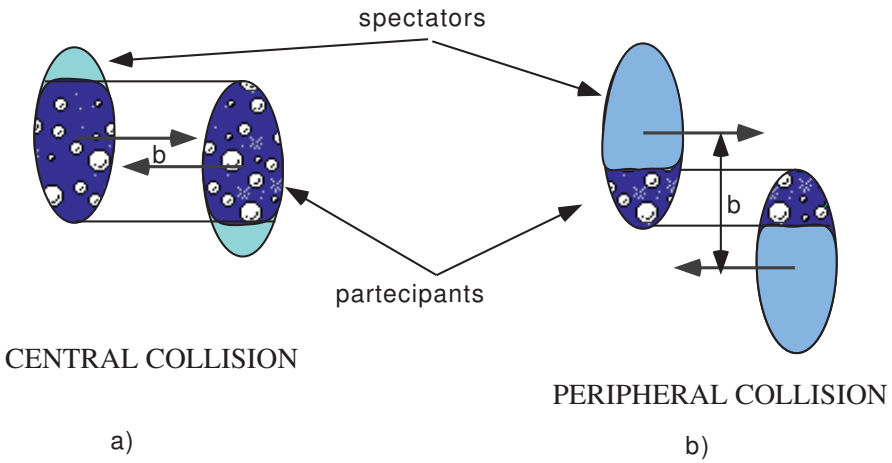

Figure 1.1: *Schematic representation of nucleus-nucleus central and pheripheral collisions*

the particles, defined as:

$$y = 0.5\ ln[(E + p_z)/(E - p_z)] \tag{1.1}$$

or its approximation for relativistic momenta, the *pseudorapidity*:

$$\eta = -ln\ tan(\theta/2) \tag{1.2}$$

The beam and target fragments will be found close to the beam and target rapidities, y_P and y_T respectively, while the particles produced in the collision at large angles will populate the central rapidity region. The greater the incident energy, the greater the separation between y_P and y_T.

1.3 Transverse Energy distribution and estimate of Energy Density

The energy which is lost by the incident nucleus reappears mainly in the form of many "soft" mesons, mostly pions. It is convenient to describe the many particles produced by a global variable which is directly measurable and closely related to the energy density produced. This is the transverse energy defined by:

$$E_T = \sum E_i sin\theta_i$$

where i is summed over all particles and θ_i is the emission angle of particle i in the laboratory reference frame.

So far, many experiments have measured the E_T distributions for several systems [4], using different beams, energies, projectiles and targets (fig. 1.2). The shape of

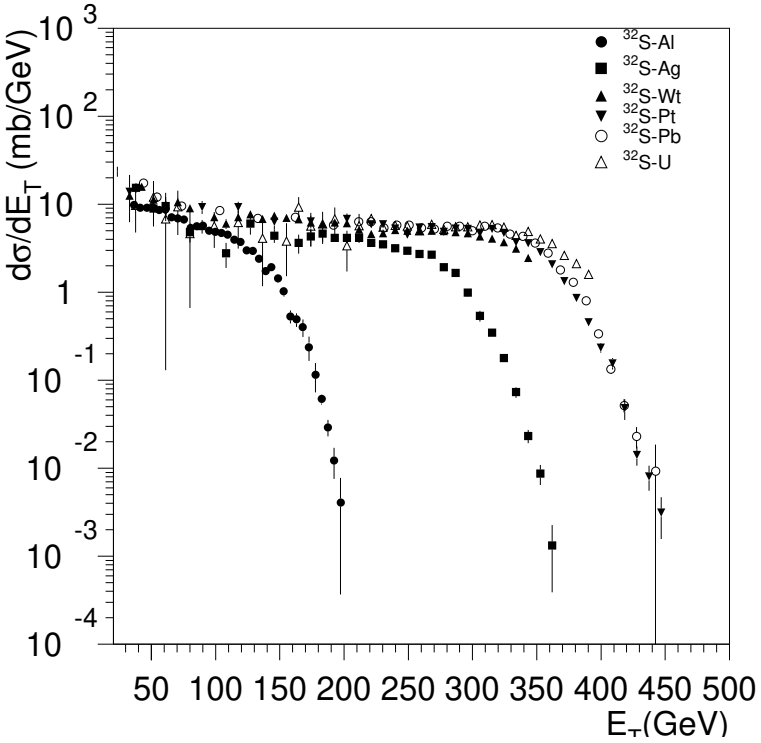

Figure 1.2: *Cross section measurements $d\sigma/dE_T$ for different targets*

the distributions is always the same, even if the maximum E_T reached is quite different. The shape in fact reflects the geometry of the interaction: it can be reproduced calculating the probability distribution of the number of possible nucleon-nucleon interactions, calculated as a function of the impact parameter from the overlap integral of the two interacting nuclei : $\Omega = \int \rho_1 \rho_2 dS$ (ρ_i=nuclear density distributions). Simple geometrical considerations allow thus to evaluate cross sections, number of participants and related kinematical quantities as shown in fig. 1.3.

Since only the stopped energy is significant, and this is re-emitted isotropically, the energy density ε can be estimated through the measurement of the transverse energy, making geometrical and dynamical assumptions. Two approaches can be taken, based on opposite hypothesis. The first one assumes that, as a consequence of the interaction between many nucleons, a "fireball" has been formed, which then explodes isotropically; the second one is based on the Bjorken hydrodynamical model [5], valid for an ultra-relativistic regime. At SpS energies, both models are inadequate to fit the situation: the rapidity distribution is not flat like it should be in the ultrarelativistic regime, nor bell-shaped like it should be in the low energy one. We are therefore aware of the fact that we can estimate only roughly the energy density.

- Low energy regime: the Fireball model

In this model, valid at lower energies, the transverse energy attained in the interaction is compared with the maximum observable E_T. The maximum energy

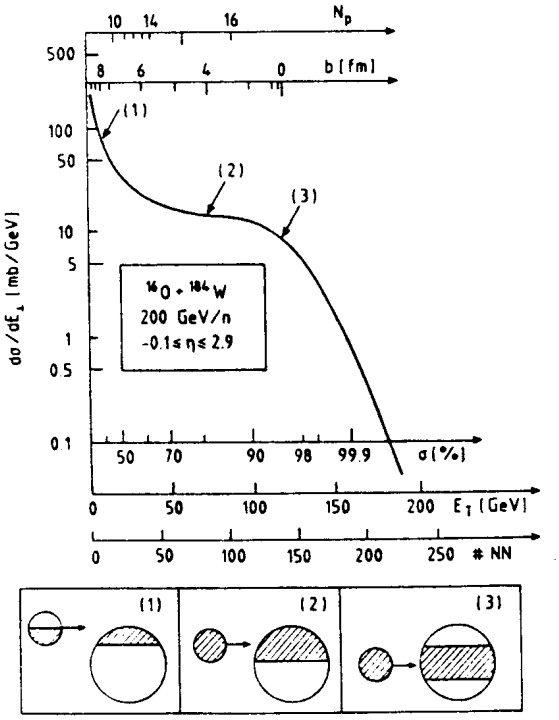

Figure 1.3: *Fit to the E_T cross section from NA34 data with a geometrical parametrization considering indipendent nucleon-nucleon collisions. For different values of E_T the model gives the number NN of nucleon-nucleon collisions, the number N_p of projectile participants, the impact parameter b and the fraction of the total geometrical cross section σ below a given E_T*

in the center of mass system (c.m.s.) for an interaction between n_P projectile and n_T target nucleons is

$$E^{max} = \sqrt{s} - m(n_P + n_T)$$

If this energy is emitted isotropically then:

$$E_T^{max} = \frac{E^{max} \int sin\theta d\Omega}{\int d\Omega} = \frac{\pi}{4} \cdot E^{max}$$

The ratio between the maximum experimentally observed E_T and E_T^{max} gives the so-called "stopping power". The maximum energy density will be

$$\varepsilon_{F.B.}^{max} = E_T^{max}/V$$

The volume V ($V = \pi R_o^2 n_P^{2/3} \cdot 2R_o n_T^{1/3}$) is the cilinder (see fig. 1.4) cut by the projectile in the target nucleus. It must be divided by the γ factor to take into account the Lorentz contraction: $\varepsilon_{F.B.}^{max} = \gamma E_T^{max}/V$. Assuming a linear dependence

of ε on E_T:

$$\varepsilon_{F.B.} = \varepsilon_{F.B.}^{max} E_T^{exp} / E_T^{max} \tag{1.3}$$

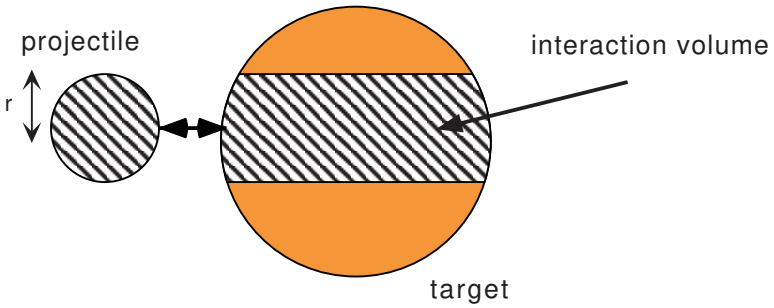

Figure 1.4: *Sketch of interaction volume in ion-ion collision*

- High energy regime: the Bjorken hydrodynamical model

The two interacting nuclei, in their c.m.s., appear as strongly contracted because of their relativistic speed: after the interaction these disks will move in opposite directions with speed $\approx c$, and the region between them will expand cylindrically. The energy will be deposited in the "interaction volume", defined, in the hypothesis of a central collision between two nuclei of radius R separated from a distance d, as the cylinder $\pi R^2 \cdot d$.

Particles (mainly pions) are not produced immediately: the time to reach equilibrium is estimated to be $\tau_o \approx 1 fm/c$. In a slice Δz around $z = 0$, at $t = \tau_o$ there are particles with $v_z \leq \Delta z/\tau_o = \Delta v_z$. The energy carried by these particles will be $\Delta E \approx \Delta E_T$. The energy density can therefore be calcuated as follows:

$$\varepsilon_{Bj} = \Delta E/V = \frac{\Delta E_T}{s \cdot \Delta z} = \frac{\Delta E_T}{s \tau_o \Delta v_z}$$

where s is the intersecting area of the two nuclei. Since $\lim_{p \to 0} y = \frac{v}{c}$ we get

$$\varepsilon_{Bj} = \frac{1}{s c \tau_o} \frac{\Delta E_T}{\Delta y} \tag{1.4}$$

The energy density, calculated in this way for S-S and S-Au collisions at 200 AGeV is 1.3 and 2.6 GeV/fm^3 while for Pb-Pb collisions at 158 AGeV it is 3.2 GeV/fm^3. Pb-Pb collisions at 158 AGeV provide up to now the highest initial energy density in the largest volume ($\sim$ 300 fm^3).

1.4 Baryon content

The baryon content of the interaction volume depends on the degree of stopping, therefore on the energy and A of the interacting nuclei. In case of full-stopping we

will have a baryon rich hadron gas, since all the participant nucleons are stopped, while at very high energy ($E \sim$ TeV) the slowed down baryons after the collision can still have enough momentum to proceed forward, and move away from the region of collision, so that the central rapidity region is populated only by mesons. At AGS energies the degree of stopping is very high: in Au-Au collisions at 14.5 AGeV the number of nucleons in the interaction volume can be as high as 400, while the number of pions is $\sim$ 700 and $\frac{dN^{\pi}_{ch}}{dy} \sim 150$. At SpS energies, with Pb-Pb collisions, the number of nucleons in the interaction volume will be a few tenth.

1.5 Temperature

The temperature can be extracted from the transverse momentum spectra, which, for 0.2 GeV/c $< p_T <$1 GeV/c, exibit a typical thermal spectrum

$$f(p_t) \propto exp(-m_t/T)$$

where m_T is the transverse mass, defined as $m_T = \sqrt{P_t^2 + m^2}$. Lower p_T are polluted by resonance decays, and larger ones by initial state scattering. Measuring the inverse slope of the m_T distribution, one can obtain T.

1.6 Global features: summary

Summarizing what has been said until now, we look for QGP in relativistic heavy ion interactions because they consist of many nucleon-nucleon collisions, and the energy lost in each of these collisions is high. We are interested in *central* collisions because these are the interactions in which the energy density is the highest, and therefore we need a good measurement of the impact parameter. This can be done using the very forward energy (through a Zero Degree Calorimeter), the transverse energy and the charged multiplicity.

The transverse energy (or the multiplicity) per rapidity unit allows to estimate the energy density reached in the interaction. Unfortunately one always needs a model: in heavy ion interactions two models are usually used, based on opposite hypothesis and therefore valid in different situations: the Fireball model, more suitable for low energy regime and the Bjorken model, valid in a ultrarelativistic regime.

From the measurements done until now, at SpS energies, on systems going up to Pb-Pb, it seems that the energy densities predicted for the deconfinement have already been reached.

1.7 Space-time evolution and Signatures of QGP

The space-time evolution of a central collision at high energy is shown in fig. 1.5. In the first instants, nucleon-nucleon collisions redistribute a fraction of the original

energy into other degrees of freedom, materializing into quarks and gluons after a time $\tau_o \approx 1$ fm/c (formation time). Parton-parton interactions might then lead to the formation of a QGP. If created, the QGP would rapidly cool down via expansion and evaporation, going through a "mixed phase" in which hadrons and "blobs" of plasma would coexist, and finally condensate into a state of ordinary hadrons, first interacting and finally decoupling (freezout). The final state reflects the complex evolution of the system, and different observables carry information on its different aspects and stages.

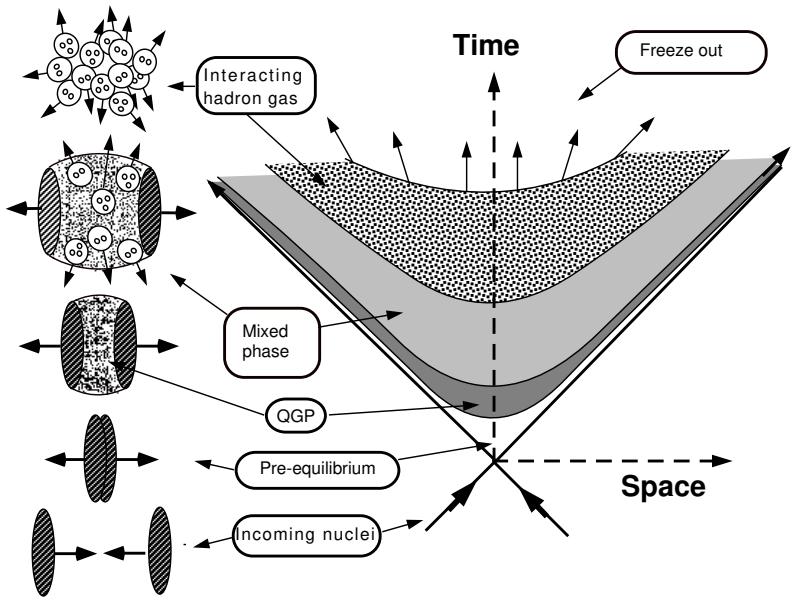

Figure 1.5: *Space-time diagram for nucleus-nucleus collision, showing the various stages of the evolution of the expanding matter.*

Initial conditions. The measurement of global event features is necessary to specify the initial conditions. As explained before, from E_{ZDC}, E_T and multiplicity one can derive, in a more or less model-dependent way, the impact parameter and the energy density.

Thermodynamic variables. The *phase diagram* of hot hadronic matter can be derived from the measurement of energy density and temperature. A phase transition involving a large latent heat would manifest itself in a characteristic shape of the T vs ε dependence: the T would first grow with ε, then remain constant while the additional energy goes into the latent heat, and finally grow again. Dileptons (originated by real or virtual photons) which decouple at early times, represent the black body thermal radiation of the system. They are the most direct measure of the system temperature, but are extremely difficult to measure. The space-time evolution of the system, and in particular the freeze-out volume, can be measured via identical particle interferometry (HBT). Finally, multiplicity fluctuations could signal the critical phenomena linked to a phase transition.

Chiral symmetry restoration. In QGP, the quarks should lose the effective mass which they carry when confined in a hadron, and recover their "bare" mass. In other words, with the quark masses small and almost equal, the QGP would be chirally simmetric. This should manifest itself in a change in strangeness production (strangeness enhancement), and in changes of the hadron masses. Mass, width and decays of particles such as ρ, ω and φ should undergo sharp modifications.

Deconfinement. As a sufficiently dense ordinary plasma can prevent the formation of atoms by electromagnetic screening of nuclei from electrons (the "Mott transition"), so would a QGP screen the colour force between quarks. Ordinary mesons, being bound states of (abundantly produced) light quarks, would not suffer such suppression. But the heavy charm-anticharm pairs necessary to make J/Ψ or Ψ' mesons are produced only rarely, in very hard quark collisions that can happen only in the initial instants of a nuclear collision. If such a pair is eventually produced in a state of deconfined quarks and gluons, ideally a QCD plasma, the evolution of an initial $c\bar{c}$ pair towards its final J/Ψ or Ψ' state could be blocked. A suppression of J/Ψ and Ψ' in central nuclear collisions, in comparison with the yield derived from the first generation nucleonic collisions, was thus expected in a dynamics proceeding via a deconfinement phase.

In the following we will describe in detail the physics of the J/Ψ and Ψ' production and the possible explanation of their suppression. The study of these resonances through their decay in two muons is the aim of the NA50 experiment and the subject of this thesis. The dimuons coming from J/Ψ or Ψ' decays have to be compared with muon pairs produced by the Drell-Yan mechanism [6], because the latter are not affected by the medium in which they are produced and thus can be used as a reference.

As shown in fig. 1.6, in the Drell-Yan process a valence quark q of a nucleon interacts with an antiquark $\bar{q}$ of the sea of a nucleon of anthoter nucleus. The q and the $\bar{q}$ annihilate creating a virtual photon that subsequently decays in a dilepton. The virtual photon interacts only electromagnetically with its surroundings, therefore it is not sensitive to the hadronic medium.

1.8 J/Ψ Suppression

The original idea of J/Ψ suppression was proposed by Matsui and Satz in 1986 [7] considering quark deconfinement. One year later the collaboration NA38 presented evidence of suppression in the ratio $(J/\Psi)/Continuum$ [8] comparing experimental data in p-U and O-U collisions and studying the O-U interactions in different intervals of transverse energy E_T. These results have been confirmed some years later by S-U interactions data. Although the interpretation of these data as a signal of QGP formation was one of the most promising, many theoretical calculations explain J/Ψ suppression in a dense hadron gas, as due to absorption and rescattering processes.

All models assume that the $c\bar{c}$ pair which should become a J/Ψ meson as a

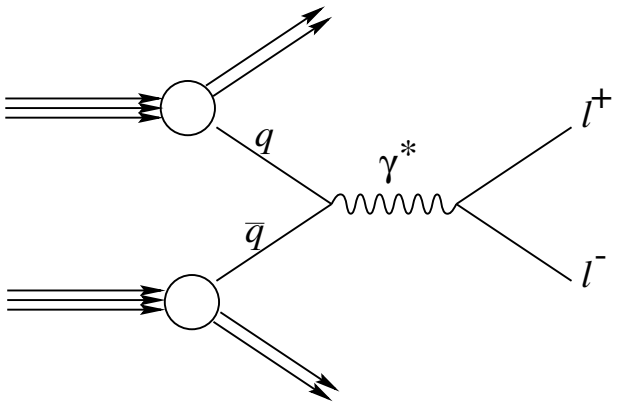

Figure 1.6: *Drell-Yan mechanism*

bound state is produced at a very early stage of the collision. By taking the mass of the charm quark $m_c \approx 1.5$ GeV, the time for the production of the $c\bar{c}$ pair in its rest frame is $\tau_p \approx 0.06$ fm/c, which corresponds to a time $t_p \approx 0.4 - 1.2 fm/c$ in the laboratory system. The time of the formation of the bound state, that is the time needed to increase the $c\bar{c}$ distance and reach the J/Ψ binding radius $r_{J/\Psi} \approx 0.45$ fm, is $t_f \approx 10 - 60$ fm/c in the laboratory system, which is much longer than t_p. Even when the target is a nucleus with a large size, most of the J/Ψ are formed outside the nucleus because the $c\bar{c}$ pair has to travel around $10 - 60 fm$ before the bound state forms. In order to explain J/Ψ suppression we can think that the plasma prevents the $c\bar{c}$ of becoming a bound state (the quark colour charges are screened) or alternatively that the dense hadronic matter prevents the J/Ψ to be formed because the c and $\bar{c}$ interact with the normal mesons of the matter. The two classes of suppression mechanisms give different predictions.

We summarize now the original model proposed by Satz and Matsui for the J/Ψ suppression in a QGP state and then we present some alternative models considering the suppression due to normal hadronic matter.

The potential binding $c\bar{c}$ to J/Ψ in vacuum is given by :

$$V(r) = \sigma r - \frac{\alpha}{r} \tag{1.5}$$

where σ is the string tension, r the separation between quark and antiquark, and the term α/r describes the Coulomb part. In a medium, the presence of other colour charges leads to a screening of the colour force and the potential becomes :

$$V(r) = \sigma r(\frac{1 - e^{-\mu r}}{\mu r}) - \frac{\alpha}{r} e^{-\mu r} \tag{1.6}$$

where $\mu = 1/r_c$ the inverse of the colour screening radius is related to the temperature of the system ($\mu \propto \sqrt{T}$).

In the case in which the state is deconfined, the first term of the potential disappears because $\sigma = 0$ while the second term has a finite range of interaction of the order r_c. The potential binding the $c\bar{c}$ in a QGP state becomes :

$$V(r)_{QGP} = -\frac{\alpha}{r} e^{-\mu r} \tag{1.7}$$

When the temperature of the system increases and μ is so large that $r_c < r_{J/\Psi}$ the range of the interaction is so small that prevents the formation of the $c\bar{c}$ bound states. The temperature predicted for this effect is $T \approx 200$ MeV.

If the plasma is formed, the c and $\bar{c}$ at the hadronisation time are usually too far to bind together, and the quarks u, d and s are present in so large numbers that can easily recombinate to form open charm hadrons. The c and $\bar{c}$ created at the early stages of the collision have thus a great probability of coupling with ligth quarks, originating charmed particles. Therefore a deconfining medium suppresses the J/Ψ and somewhat enhances the D and $\bar{D}$ (open charm mesons) production.

The J/Ψ binding radius is $r_{J/\Psi} \approx 0.45$ fm while the dimension of the other state of the charmonium system, the Ψ', is larger ($r_{\Psi'} \approx 0.88$ fm), therefore the Ψ' is expected to be suppressed at energy densities lower than those necessary for J/Ψ suppression.

As written before, some models try to explain the suppression in terms of J/Ψ absorption in a dense hadronic matter. The study of $p-A$ collisions is fundamental to estimate the J/Ψ absorption in nuclear matter because in these interactions the plasma state is not formed. One of the most interesting results of the last years, coming from the analysis of the quarkonium states, is that experimental data exhibit an attenuation in charmonium production also in proton-nucleus collisions that increases with the size of the target nuclei.

The data of the attenuation are well reproduced by a phenomenological absorption law proposed by Gerschel and Hufner [9] :

$$S_o = e^{-\rho_o \sigma_{abs} L_A} \tag{1.8}$$

in which ρ_o is the baryon density ($0.15 fm^{-3}$), σ_{abs} is the absorption cross section and L_A is a scale of the average length traversed by the initially produced $c\bar{c}$ pairs in nuclear target. As we can see in fig. 1.7 all the data of proton-nucleus collisions are well fitted by this law with a value of the absorption cross section $\sigma_{abs} = (6.2 \pm 0.3)$ mb

Analysing the NA38 data in O-Cu and S-U collisions at 200 GeV per nucleon, supposing that J/Ψ interacts only with nucleons in a hadron gas without the formation of a QGP, an absorption cross section $\sigma_{abs} = (5.8 \pm 1.8)$ mb has been obtained in agreement with the proton-nucleus data. The fact that the suppression for nucleus-nucleus collisions, up to S-U, has the same law of proton-nucleus data is an indication that QGP was not formed.

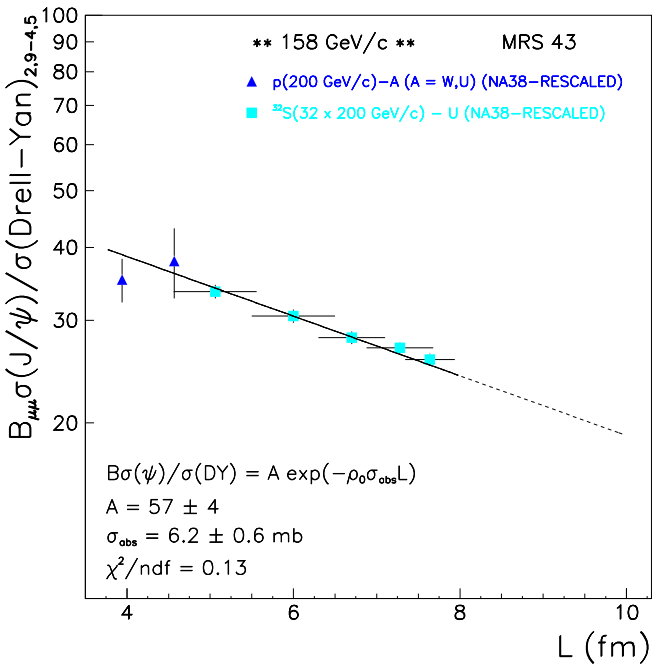

Figure 1.7: *J/Ψ suppression in proton-nucleus and nucleus-nucleus collisions*

1.9 J/Ψ Production mechanism

The value of the absorption cross section obtained fitting the experimental data is not in agreement with the simplest theoretical models that predict a cross section around $2-3$ mb. To explain these data theoretically we have to improve the usual hadronisation mechanism $q\bar{q} \rightarrow J/\Psi$.

The main mechanism for J/Ψ production in hadronic collisions is gluon fusion, as described pictorically in fig. 1.8. Two gluons interact in a hard process to form a $c\bar{c}$ pair that is a colour octet, this state neutralizes its colour radiating or absorbing a gluon thus becoming a colour singlet, subsequently the c and $\bar{c}$ increase their distance producing the bound state J/Ψ. In this model, in which the J/Ψ is a colour singlet $(c\bar{c})_1$, the cross section for $(c\bar{c})_1$-nucleus interactions is $\sigma_{abs} \approx 2-3$ mb, that is, half the experimental one.

To explain the experimental data a new model of J/Ψ formation has been formulated. The J/Ψ meson could be described (like every meson) by the superposition of several states in Fock space :

$$\mid \Psi >= a \mid (c\bar{c})_1 > + b \mid (c\bar{c})_8 g > + ... \qquad (1.9)$$

in which every state is a colour singlet, also if $c\bar{c}$ is not neutral. In most of the mesons it has been proved that $a \gg b$ and the colour singlet $(c\bar{c})_1$ is the dominant term, while in J/Ψ production at high energy the second term, that is an octet $(c\bar{c})_8$ state coupled to a gluon, is prominent. In this model, called "Colour Octet

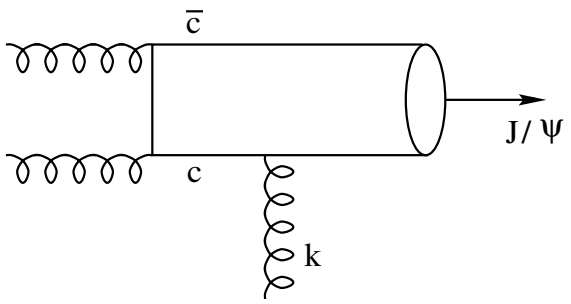

Figure 1.8: *J/Ψ production mechanism through the colour singlet $c\bar{c}$*

Model", the $(c\bar{c})_8$ crosses the nuclear matter together with a collinear gluon that neutralizes its colour. This pre-resonant state $c\bar{c}g$ can either be absorbed by the surrounding matter or it can happen that after a time $\tau_8 = 1/\sqrt{2m_c E_g}$ (E_g is the energy of emitted or absorbed gluon), the $(c\bar{c})_8$ absorbs the gluon thus becoming a colour singlet $(c\bar{c})_1$ and subsequently the J/Ψ meson (see fig. 1.9).

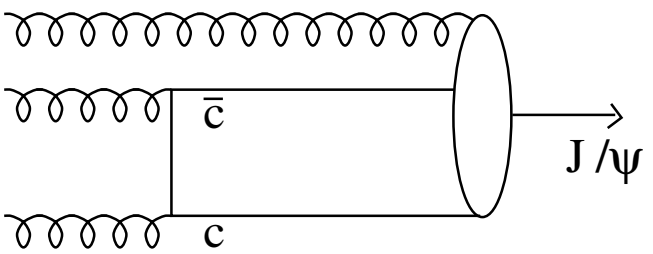

Figure 1.9: *J/Ψ production mechanism through the colour singlet $c\bar{c}g$*

To evaluate the J/Ψ absorption in this model, we have to consider the cross-section for $c\bar{c}g - nucleon$ interactions and suppose that this pre-resonant state is absorbed. With these assumptions, the calculated absorption cross section of the J/Ψ is $\sigma_{abs} \approx$ 6-7 mb, in good agreement with the result of the phenomenological fit of experimental data.

Therefore the data obtained by NA38 up to S-U collisions on J/Ψ suppression can be explained by this absorption model, from which one can conclude that no evidence of the existence of QGP has been found by this experiment.

Considering these results and the fact that the suppression remains a promising signature of the creation of a deconfined phase, the next experimental step is to reach the conditions which favour the formation of the plasma. These conditions can be obtained increasing the temperature and the energy density of the system

with respect to those achivied by NA38 and observing if the J/Ψ suppression can be interpreted only in terms of QGP formation. This is the aim of the NA50 experiment in which the suppression is measured by studying Pb-Pb collisions at 158 GeV/nucleon. For these collisions, at very low impact parameters, one expects to achieve densities $\approx 35\%$ greater than those obtained in S-U collisions, along with other conditions more favourable to the formation of a QGP.

Bibliography

[1] C.Y. Wong, Introduction to High-Energy Heavy-Ion Collisions, World Scientific, 1994.

[2] J. Cleymans et al., Phys. Rep. 130, 217-292, 1986

[3] E. Laermann, Nucl. Phys. A 610, 1c-12c, 1996

[4] H.R. Schmidt and J. Schukraft, J Phys. G19, 1993

[5] J.D. Bjorken, Phys. Rev. D 27, 140, (1983)

[6] S.D. Drell and T.M. Yan, Phys. Rev. Lett. 25, 316, 1970

[7] T. Satz and T. Matsui, Phys. Rev. Lett. B 178, 416, 1986

[8] C. Baglin et al. Phys. Lett. B 220, 471-478, 1989

[9] C. Gerschel and J. Hufner, Nucl.Phys. A544, 513, 1992

Chapter 2

The NA50 Experiment

The NA50 experiment studies the production of dimuon pairs in ultrarelativistic interactions of proton and Pb ions. It is a fixed target experiment and it uses the CERN SpS proton and Pb beams [1].

The experimental set–up is based on the old NA10 spectrometer, upgraded at the end of the 80's for the NA38 experiment. NA50 uses in fact the same set-up of NA38 with some new detectors for the determination of the centrality of the interaction. They are an electromagnetic calorimeter (EMC), a zero degree calorimeter (ZDC) and a multiplicity detector (MD). These three detectors are uncorrelated, which means that it is possible to check the validity of the results obtained using each of them in independent way.

NA50 has an active target made of 7 lead subtargets plus an interaction recognition system (quartz blades) which allows the identification of the subtarget in which the interaction took place.

In the following sections I will present a brief description of the different detectors used in NA50 for the muon track reconstruction, the trigger and the centrality determination. For what concerns the NA38 and NA51 experiments, whose data will be shown for comparison in the final chapter, I will not describe the experimental set–up. Details about this can be found in [1], [2].

2.1 The muon spectrometer

The muon spectrometer, which constitutes the main body of NA50 (see fig. 2.1), measures the kinematic variables which characterise the dimuons produced in the interaction of a proton or of a lead ion in the lead target. It is made of a muon absorber, followed by the toroidal field magnet (see fig. 2.2). Both upstream and downstream of the magnet there are 4 planes of plastic scintillator hodoscopes used for the trigger and 8 planes of proportional wire chambers used for the muon track reconstruction. The magnetic field is generated by 6 solenoids, each of them occupying an azimuthal angle of 18^o, in which flows a current of 7000A. The value of the current has been enhanced passing from NA38 (4000A) to NA50 in order to improve

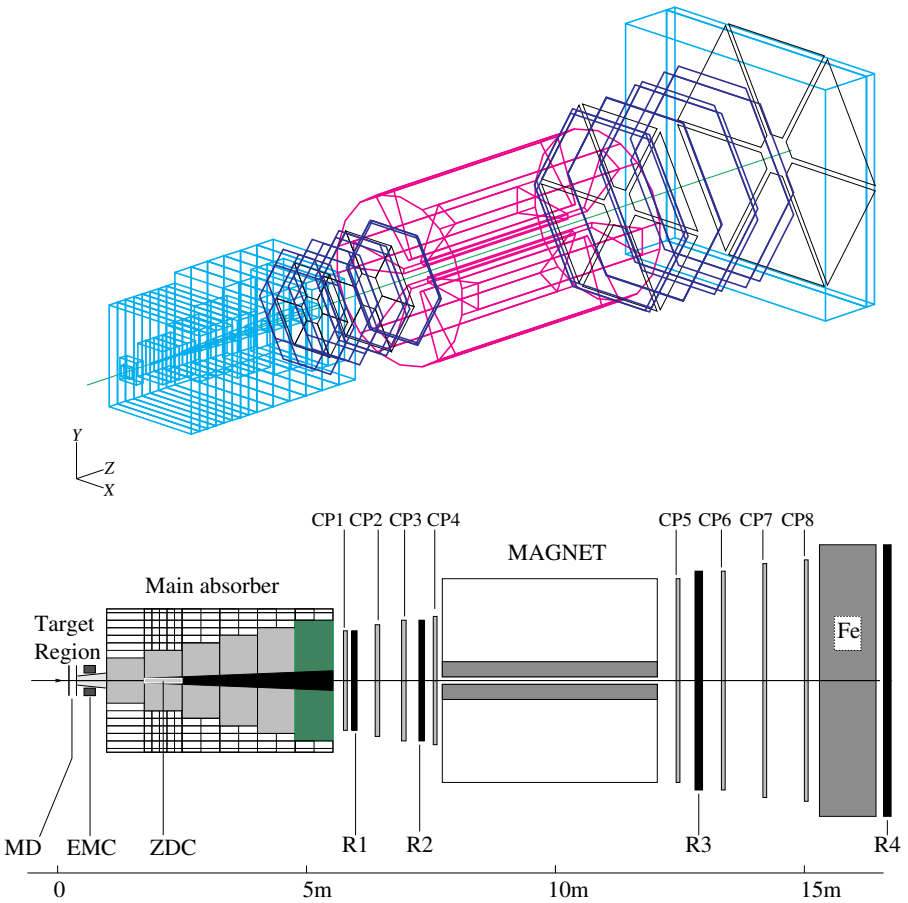

Figure 2.1: *The muon spectrometer*

the mass resolution and to get rid of a large number of low momentum particles expected in lead–lead collisions. The frequency of the current is synchronized to the SpS beam extraction cycle.

The shape of the field is given by the formula:

$$B(r) = \frac{B_0}{r} e_\Phi \tag{2.1}$$

where B_0 is $0.383T \cdot m$ in NA50 (see fig. 2.3). In this way the charged particles generated in the interaction are kept in the same azimuthal plane but they are deflected by an angle $\Delta\Theta$ inversely proportional to their transverse momentum p_T.

2.2 The trigger hodoscopes

The trigger signal for the experiment is provided by two sets of scintillator hodoscopes (see fig. 2.4). Each set is made of two hexagonal planes of plastic scintillators. The two first hodoscopes, called R_1 and R_2, are placed between the main

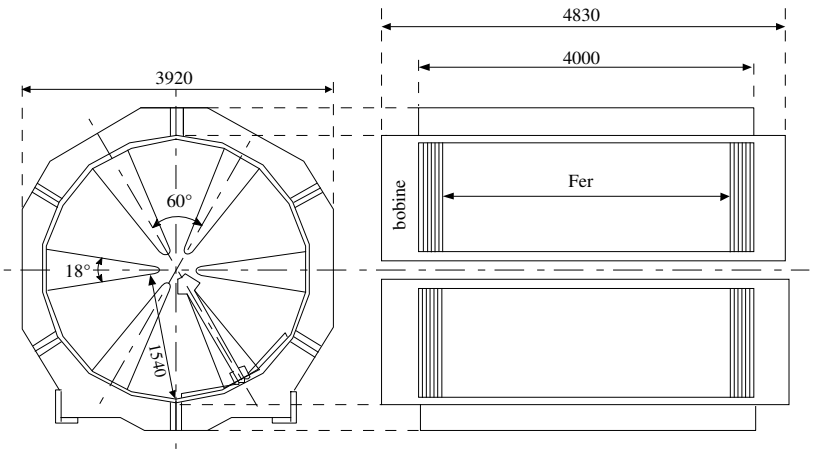

Figure 2.2: *Different views of NA50 magnet*

absorber and the magnet, while the other two - R_3 and R_4 - are placed after the magnet, one before and the other after the iron wall. Each hodoscope is made of 6 azimuthal units divided in 30 scintillator blades. On R_1 and R_2 the dimension of the each blade grows going further from the beam axis, and R_2 is the homothetic copy of R_1 with respect to the position of the central subtarget (see fig. 2.5). According to this geometry, the trajectory of a particle crossing the blades R_1^i and R_2^i (or R_2^{i-1}) comes directly from the interaction vertex. The second set is made of blades of the

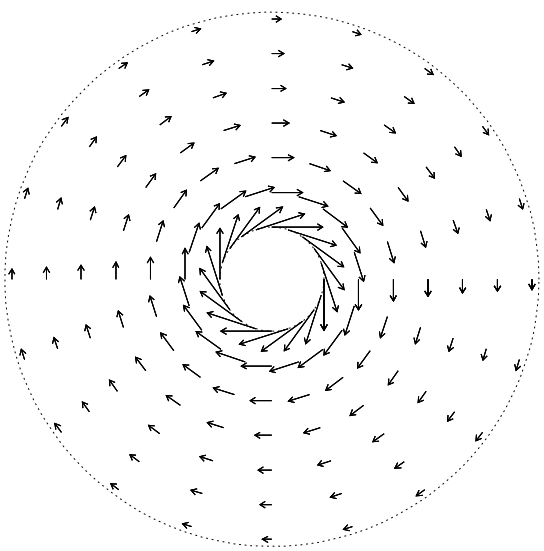

Figure 2.3: *Shape of magnetic field*

same dimension (5.5 cm), and the coincidence between blades before and after the magnet allow an estimate of the particle trajectory after the deflection inside the magnet. Two other hodoscopes named P_1 and P_2 are placed before the magnet

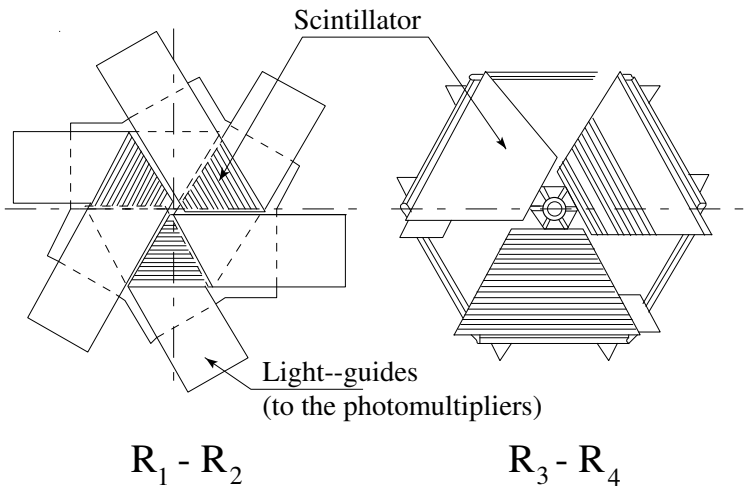

Figure 2.4: *The trigger hodoscopes*

(P_1) and after the iron wall (P_2). They are used as an indipendent trigger system used to control the efficiency of the main trigger system.

2.3 The proportional wire chambers

The reconstruction of the dimuon tracks is done by means of two sets of four MWPC (Multi Wire Proportional Chambers) (see fig. 2.6). The first set of chambers, namely $CP_{1,2,3,4}$, is placed immediatelly after the absorber and is used to reconstruct the trajectories before the deflection due to the magnetic field; these chambers have a radius of 1.3 m. The second set ($CP_{5,6,7,8}$) is placed after the magnet, and is used to reconstruct the trajectory after the deflection due to the magnetic field; each of the chambers has a radius of 3 m. The detectors have hexagonal geometry and are made of 3 planes of wires with different orientation with respect to the horizontal axis: 0, 60 and 120 degrees. The total number of wires in the smaller chambers is 749, while it is 1229 in the bigger ones. They are filled with a mixture of Argon (80%), Isobutane (19.8%) and Freon (0.2%). The precision in the determination of the direction reached with this system is of some tenth of mrad.

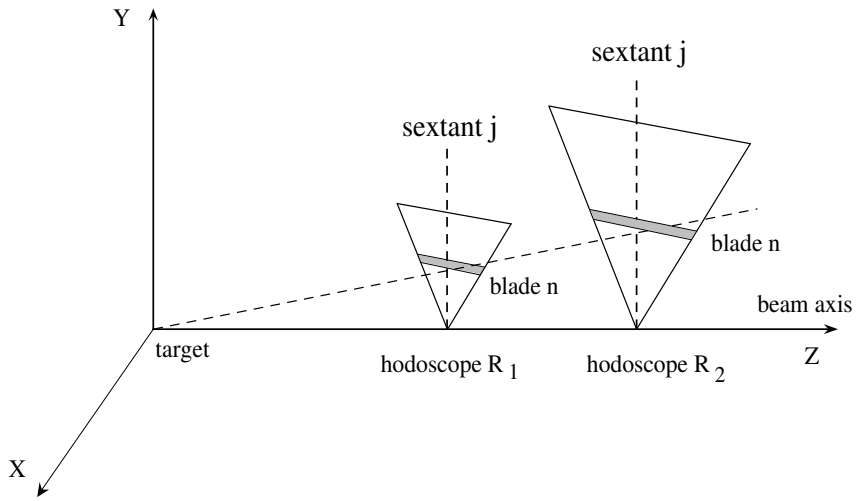

Figure 2.5: *The different dimensions of blades in the first set of hodoscopes*

2.4 The absorber

The absorber is used to reduce the muon background due to the decays of particles produced in the collisions (in particular K and π mesons). It can be divided into 3 main parts:

- the plug: an internal body with a conical geometry, made of tungsten and uranium, 3.6 m long. It is used to absorb the projectile spectators and the beam particles that did not interact in the target. The central heavy core is placed 165 cm downstream from the central subtarget to avoid the creation of new dimuons in the spectrometer acceptance.

- a 4.8 m long absorber that covers the spectrometer acceptance (32-116 mrad). It is used to stop the products of the interaction which are not muons, without affecting the trajectory of muons crossing it. It is made of a block of 4 m of carbon followed by 80 cm of iron. Another absorber made of berillium oxide is placed behind the EMC. It is used to stop all the charged π and K, before they decay into muons.

- a thick wall of iron and concrete (see fig. 2.7) in which all the previous parts are placed

A wall of iron 1.2 m thick, placed between the last set of MWPC and the last hodoscope R_4, absorbs the mesons which crossed the spectrometer in order to avoid non-muonic triggers.

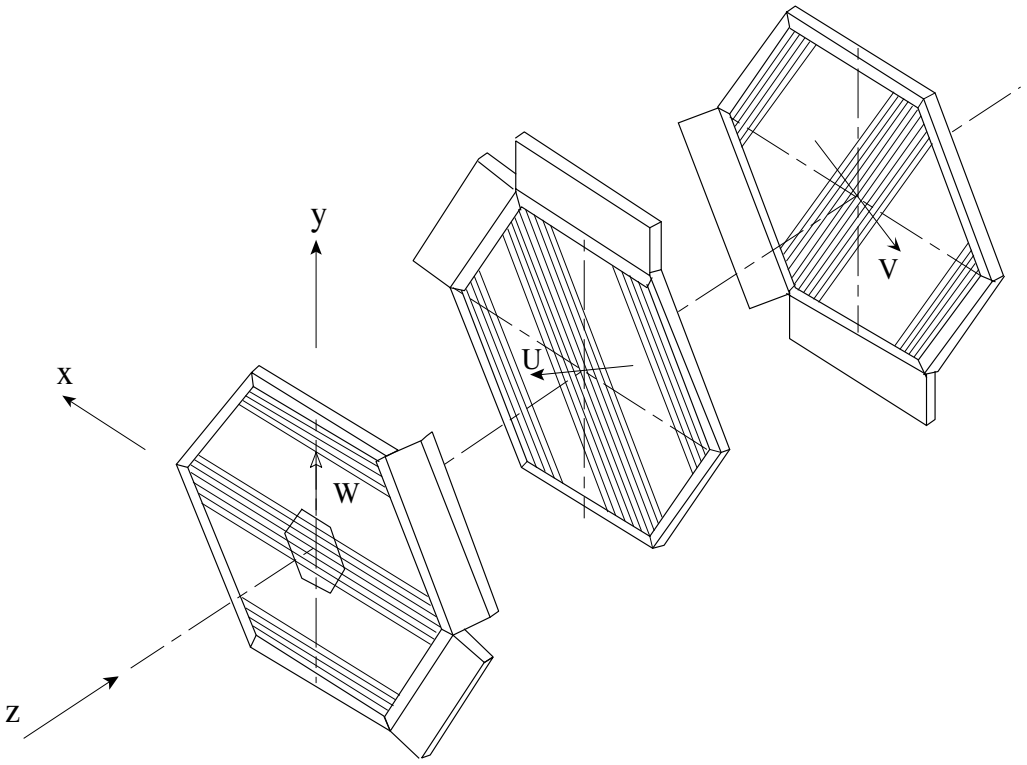

Figure 2.6: *The Multi Wires Proportional Chambers*

2.5 The active target

The requirements of the NA50 target are:

- have a length of at least $18\%\lambda_I$ to reach the luminosity required to study J/Ψ and Ψ'
- avoid reinteraction of fragments
- have a good identification of the vertex position
- be radiation resistant.

A segmented target featuring detectors to identify the vertex of the interaction has therefore been implemented (see fig. 2.8). In particular, the lead target was

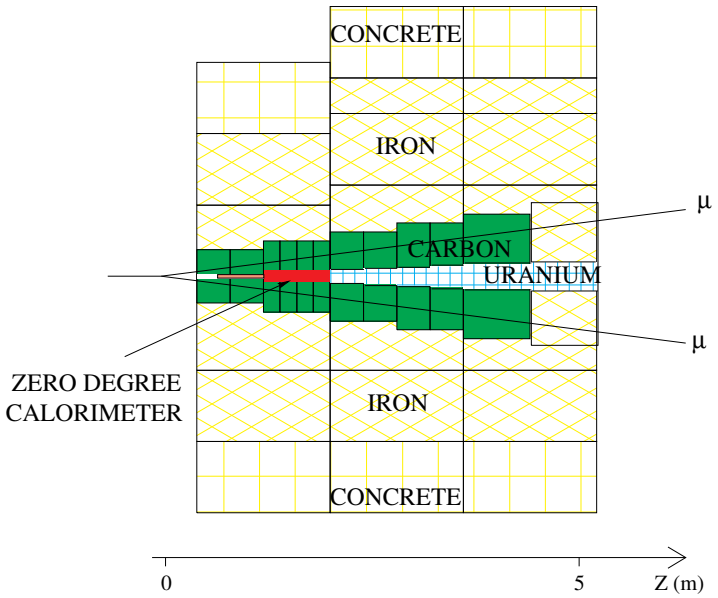

Figure 2.7: *The absorber*

divided in 7 subtargets, each of them being sufficiently thin to minimize reinteractions. They are placed along the beam line at regular intervals of z=25 mm. In the 1995 run their size was 1.5 x 1.5 x 1 mm^3, for a total length corresponding to $18\%\lambda_I$. In the 1996 run, 5 subtargets were thicker (2 mm instead of 1) and the total length was $30\%\lambda_I$.

Due to the high level of radiation in the target region, NA50 chose to change the target recognition system used in NA38 (scintillators). The new system is made of quartz blades placed on both sides of each subtarget (see fig. 2.8). This material has been chosen for its good radiation resistance. The quartz blades collect the Cerenkov light produced by high energy pions crossing them and can identify the subtarget in which the interaction took place. A couple of blades placed before the first target is used to recognize interactions which took place in the air before the target system. The thickness of the blades (1 mm) minimizes the production of secondary particles. In addition, a couple of anti-halo counters is used to get rid of ions interacting out of a 3 mm diameter cylinder, since the beam dimensions are $\sigma_x \approx \sigma_y \approx 0.4$ mm. For what concerns the p-A runs, the active target is not used and it is substituted by a monolithic block of the desired material.

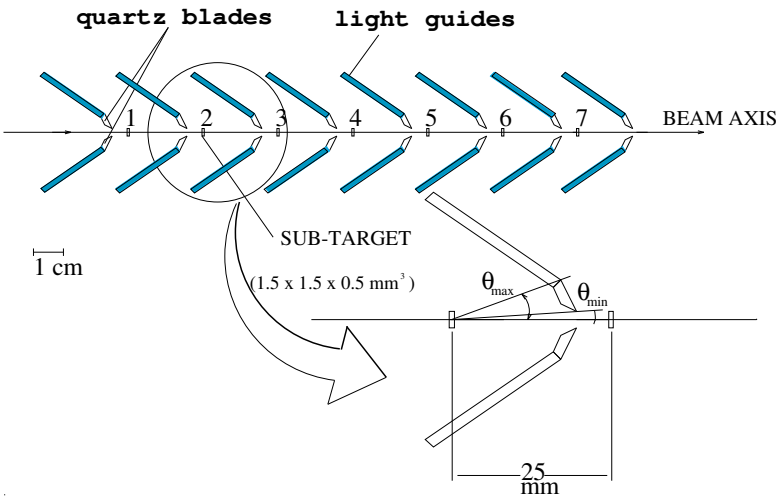

Figure 2.8: *The active target*

2.6 Centrality detectors

The measurement of the centrality is very important in case of Pb-Pb interactions. In NA50 it is done using 3 independent detectors: the electromagnetic calorimeter (EMC), the zero degree calorimeter (ZDC), and the multiplicity detector (MD), which has been mounted in its final version in the 1996 Pb-Pb run. The EMC measures the transverse energy of the interaction (E_t), the ZDC measures the residual energy of projectile fragments and the MD measures the total number of charged particles produced. Each of these quantities is related to the impact parameter of the collision, b. Actually, the number of interacting nucleons grows with centrality. Hence, also E_t and the multiplicity grow, being themselves proportional to the number of participant nucleons. On the opposite, the number of projectile fragments reaching the ZDC decreases, and so does the forward energy E_{ZDC}.

2.6.1 The electromagnetic calorimeter

It is made of polystyrene scintillating fibers (diameter=2 mm), parallel to the beam direction and embedded into an alloy of lead and bismuth. The ratio fiber/alloy is equal to 1/2. This device is very compact (14 cm long) and corresponds to 15.5 interaction lengths. It is positioned 32 cm downstream with respect to the center of the target. The central hole has a radius of 8.2 cm, while the external radius is equal to 24.2 cm. The total coverage in pseudorapidity is $1.1 < \eta < 2.3$ in the

laboratory reference frame. The EMC has the same hexagonal azimuthal geometry of the spectrometer and is divided into four crowns, each of them covering a pseudo-rapidity interval $\Delta\eta$=0.34. The EMC measures the total neutral transverse energy produced in the collision with a resolution of 5% for E_t close to 200 GeV.

2.6.2 The zero–degree calorimeter

It measures the energy of the spectator fragments of the projectile and allows us to know the energy deposited in the interaction (E_{dep}=E_{beam}-E_{ZDC}).

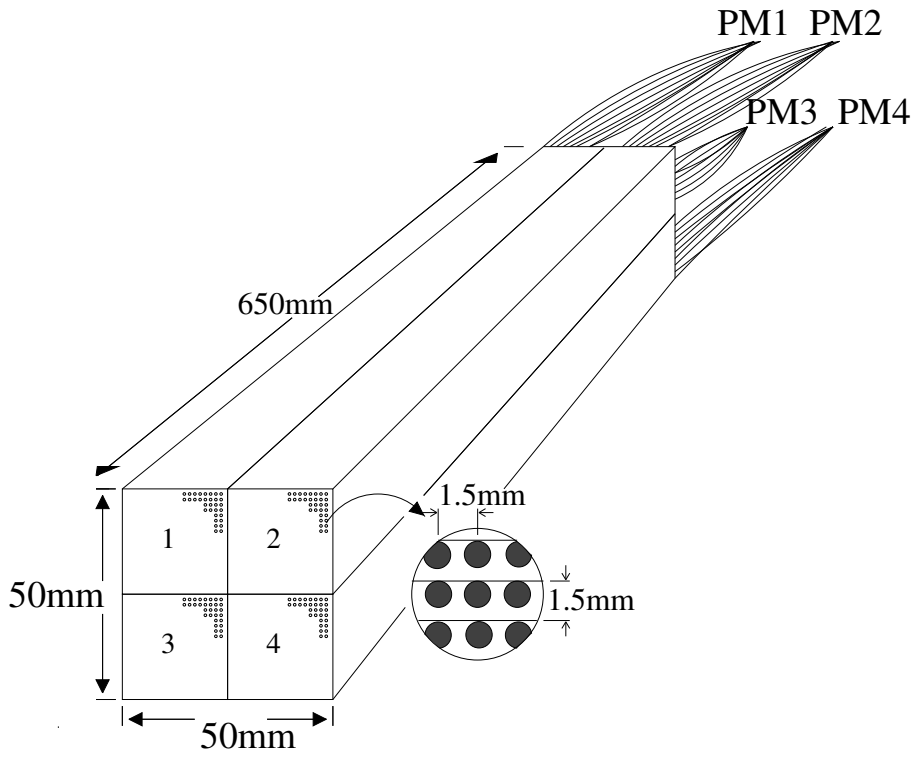

Figure 2.9: *The Zero Degree Calorimeter*

It is placed 165 cm downstream of the target, it has a cross section of 5 x 5 cm^2 and it is 65 cm long. It measures the Cerenkov light produced into 900 of quartz fibers with a diameter of 365 μm embedded into 30 tantalum blades 1.56 mm thick. The ratio Si/Ta is equal to 1/17. The fibers are 1.8 m long. For the first part (65 cm) they are placed parallel to the beam axis and constitute the active part of the detector, the rest (1.15 m) is bent and used as a light guide towards 4 photomultipliers (see fig. 2.9). The fibers are divided into 4 groups each one read by one of the 4 photomultipliers in order to have a beam position sensitive detector. The resolution of the ZDC is σ_E/E=5% in case of a 158 $\cdot A\cdot$ GeV Pb beam.

Beam	intensity (part/sec)	burst time(sec)	interburst time (sec)
Pb	5.10^7	4.3	14.8
p	10^{11}	2.5	11

Table 2.1: The SpS cycles for different beams

2.6.3 The multiplicity detector

The multiplicity detector is used to measure the number of charged particles produced in the collision. The next chapter is devoted to a detailed description of this detector.

2.7 NA50 beam line

The NA50 experiment is placed on the ECN3 line of CERN SpS. Two kinds of beam are used for our experiment:

- a proton beam with a maximum number of particles per burst of 10^{11} and an energy of 450 GeV/nucleon
- a Pb^{82+} beam with an average number of particles per burst of $5 \cdot 10^7$ and an energy of 158 GeV/nucleon.

The cycle is different for the two beams, and its characteristics, the burst duration (t_{burst}) and the time between two bursts ($t_{IntBurst}$) constraint the data acquisition timing and the maximum available time for the data transfer. In tab. 2.1 are shown the specifications of each beam.

2.7.1 The beam hodoscope

The beam hodoscope BH is located 33 m upstream from the target, in a region where the beam spot is large enough so that individual incoming ions can be tagged. It is made of one plane of 16 quartz blades (2 raws of 8 each) associated with photomultipliers detecting the Cerenkov light produced by incident ions in the quartz. The efficiency reached using quartz blades is better than 99%.

The thickness of each blade is 1 mm, and the transverse size is adapted to the beam intensity profile so that each counter sees about 1/16 of the total beam intensity. Standard TDCs record the precise time of arrival of the ions within a given gate, appropriately timed with respect to the ion that has triggered the apparatus. The information is used to tag beam pile–up. We talk about beam pile–up when two incoming ions are separated in time by less than 40ns. In addition, a few scintillators are placed after the BH off the beam axis to tag possible interactions of the Pb in the BH itself. During the proton runs the quartz BH is replaced by a conventional scintillator.

2.8 Trigger selection

In the NA50 experiment 3 different types of trigger are used:

- DIMUON TRIGGER: it is the main trigger and it has been developed to select events in which a couple of muons (a dimuon) has been produced. In particular we are interested in those events in which the dimuon has been produced directly in the interaction and not in those coming from K and π decays or interactions in the absorber, which are eliminated as soon as possible.

  There are 2 levels of trigger; the first one selects events in which 2 tracks originated in the target region have crossed the spectrometer in 2 different sextants. This trigger is based on the coincidence between the scintillators of R_1 and R_2 hodoscopes. In this way we get rid of those muons that have been deflected strongly in the absorber because of multiple scattering. The signal thus obtained is then put in coincidence with the R_3 and R_4 hodoscopes.

  The trigger system furnishes also a rough value of the deflection angle of each muon and then the transverse momentum p_T.

  The signal obtained in this way is called TSJ (Trigger Sans Jitter): it has a time instability of about 1 ns. Another trigger called T0J (Trigger Zero Jitter) is obtained with a synchronization with the BH signals. For this trigger the jitter is less then 0.5 ns. The second level trigger selects events according to their kinematical and dynamical characteristics. It is computed by a CAB microprocessor and allows us to select events according to the invariant mass of the dimuons, to their transverse energy and the number of scintillators hit. This trigger makes the data acquisition system (DAQ) and the tape recording active.

- ZDC TRIGGER: The trigger signal is generated each time the ZDC signal is higher than a fixed threshold. For this threshold a very low value (60 mV) has been chosen in order to a have a signal each time something gets into the ZDC. Most of these triggers are events in which a lead ion did not interact in the target and then deposited all its energy (33 TeV) in the calorimeter.

- LASER TRIGGER: for this trigger a signal is sent to the EMC photomultipliers and it is used especially to evaluate the different detectors pedestals, that is, the answer of an ADC when there are no inputs to the detector.

2.9 DAQ system and data recording

The detailed description of the DAQ system of the NA50 experiment is reported in [4]. We just recall here some concepts that will be useful in the next chapters.

The total number of data to be transferred and recorded is given by summing the amount of data coming from each detector:

- 2 Mb/burst for the MWPC
- 2 Mb/burst for the hodoscopes
- 4 Mb/burst for the beam hodoscope, the EMC and the ZDC
- 8 Mb/burst for the multiplicity detector.

These values correspond to a maximum number of 5000 events per burst and the total is 16 Mb, to be transferred and recorded in about 15s, the interburst time of SpS lead cycle. The scheme of the general NA50 DAQ system (excluding the Multiplicity Detector) is shown in fig. 2.10.

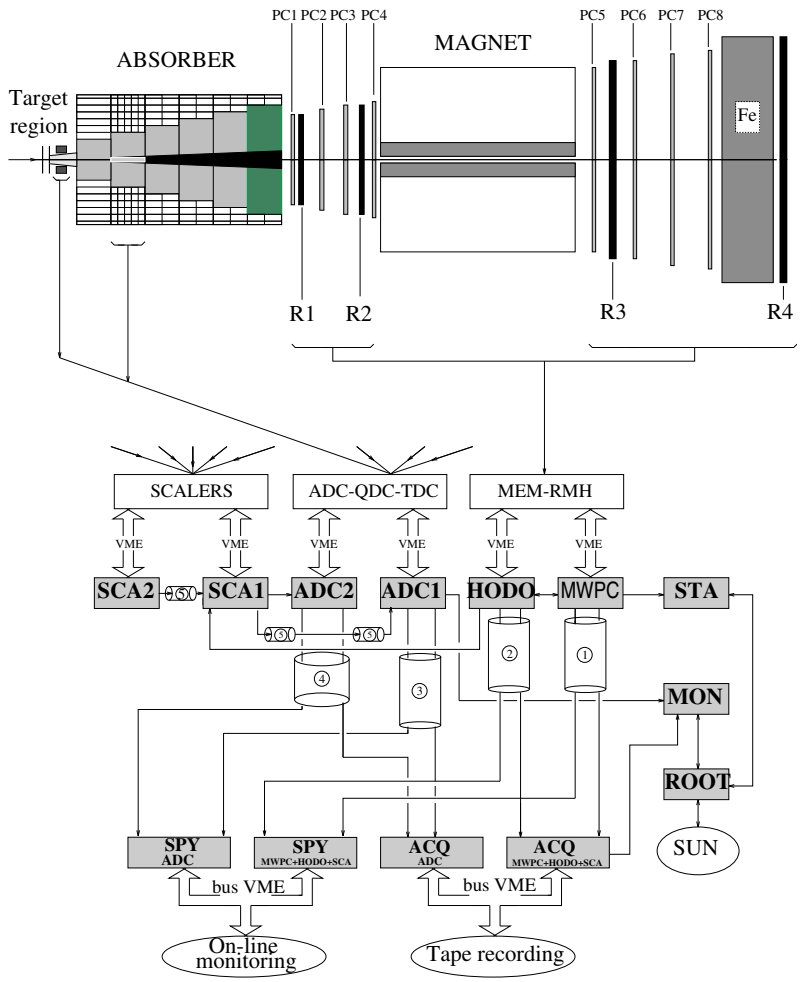

Figure 2.10: *The NA50 general DAQ system (excluding the MD)*

The NA50 collaboration chose to transfer data to the final memory burst by burst and not event by event. During each burst the data are stored in special intermediate memory. At the end of each burst the data are transferred to the final

memories. In fact NA50 chose to duplicate the final memory, creating separated ACQUISITION and SPY memories. The last one is very important, because it allows checks of the behaviour of single detectors during the data taking period (without slowing down the acquisition) and, if necessary, to repair hardware failures before the end of the run.

The ACQUISITION memory is connected to the tape recording system. If all the detectors are correctly read, each 200 MBytes tape takes about 20 minutes to store the collected data. This amount of time is defined as a RUN and this definition will be frequently used later on in this thesis.

Bibliography

[1] C.Lourenco, Ph.D. Thesis, LIP, Lisbon, Portugal (1995).

[2] B.Espagnon, Ph.D. Thesis, Blaise Pascal University, Clermont-Ferrand, France (1995)

[3] Study of Muon Pairs and Vector Mesons Produced in High Energy Pb-Pb Interactions, Proposal CERN/SPSLC 91-05, SPSLC/P 265, October 1991

[4] V.Capony, Ph.D. Thesis, Savoy University, Annecy-Le-Vieux, France (1996)

Chapter 3

The NA50 multiplicity detector

3.1 Introduction

The multiplicity detector is a silicon strip detector used to measure the angular distribution and the multiplicity of charged secondaries produced in high–energy Pb–Pb interactions over a wide angular coverage which includes the NA50 muon spectrometer coverage. It is used to characterize the events according to their centrality in the NA50 experiment.

Since the experiment takes data at very high rate, and the silicon detectors operate in the high–radiation area close to the target, the detector has to be very fast (dead time below 50 ns), radiation resistant (up to the Mrad level as dose and up to 10^{14} particles/cm^2 as non–ionizing damage) and of high granularity. The conditions on noise, speed and radiation hardness are comparable to the ones foreseen at the future Large Hadron Collider at CERN.

The overall layout of the NA50 target region is shown in fig. 3.1, including targets, target identification system and the multiplicity detector units. The target system has to be placed very close to the absorber in order to limit the decay background in the dimuon spectrum, and therefore the space available for the multiplicity detectors is limited to about 10 cm in the longitudinal direction. Due to various constraints (presence of a set of 7 targets distributed along the beam line, beam width and divergence, need to minimize secondary interactions and photon conversions in the targets) the measurement is done with two identical detector units (MD1 and MD2), each serving one half of the total number of targets.

One of the two faces of MD1 is shown in fig. 3.2. Each detector unit is a disc of inner radius 4.4 mm and outer radius 86 mm, segmented both azimuthally and radially so as to have almost constant occupancy per sensitive element ($\Delta\eta \approx 0.02$, $\Delta\phi = 10^0$). The total number of independent channels is 13824, which keeps the local occupancy below 30% at the highest expected multiplicities. The detector provides

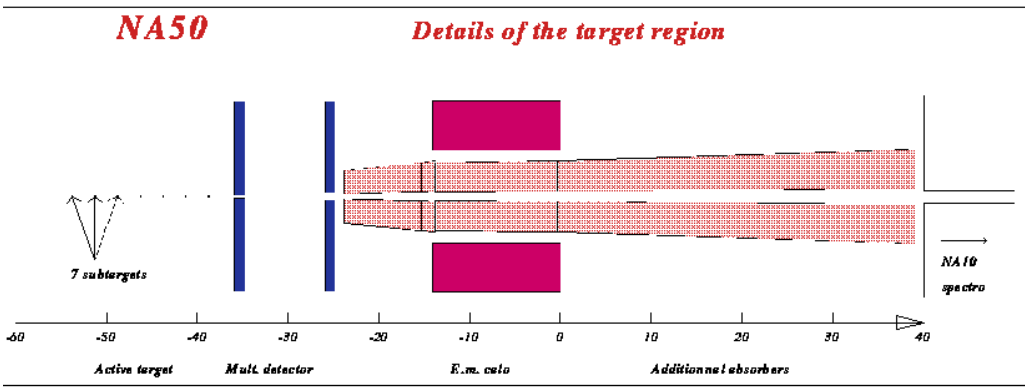

Figure 3.1: *Scheme of the NA50 target region*

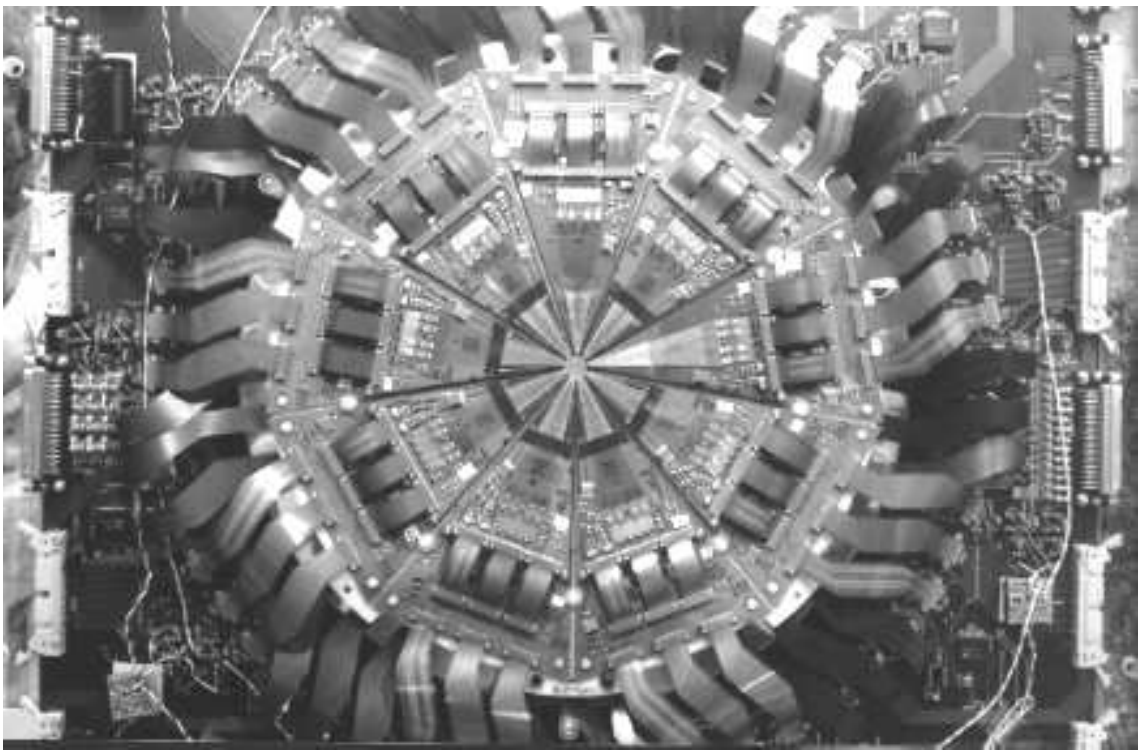

Figure 3.2: *Picture of one plane of the Multiplicity Detector*

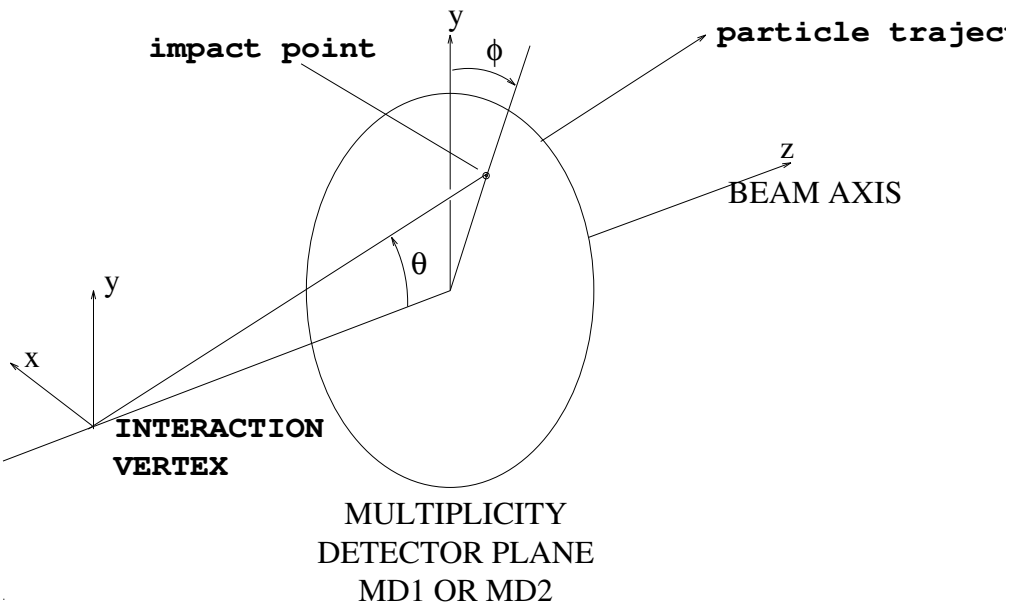

Figure 3.3: *Particle hit on the Multiplicity Detector*

a single–point measurement of the particle's angles (see fig. 3.3) using the vertex position derived from the knowledge of the target; the size of the rapidity step is matched to the uncertainty on the angle which derives from the beam size and the multiple scattering in the target. From GEANT simulations the expected resolution on the charged multiplicity is better than 10% for central events, dominated by secondary interactions and conversions in the target. The multiplicity detector is also used as a target recognition system, using an algorithm which evaluates the possibility of having a couple of strips on the two detectors hit by a particle coming from one of the 7 subtargets.

Since the multiplicity detectors are exposed to high, and non–uniform, radiation levels, reaching over 2 Mrads and more than 10^{14} particles/cm^2 at the innermost radii, each detector unit is built as a mosaic of silicon detectors, each assembled on an independent multilayer board together with its front–end electronics, so that they can be easily replaced in case of severe damage. The major components of the MD in the target region, namely individual detectors (two types), analog chips, digital chips, boards, bus cables and front–end control modules, are listed in table 3.1.

Component	Description of module	# channels per module	# modules (total)*
DET1	Detector crown 1	2x128	36
DET2	Detector crown 2	2x64	36
FABRIC[a]	Analog chip	64	216
CDP[b]	Digital chip	64	216
BOARD1	PC Board crown 1	4x64	36
BOARD2	PC Board crown 2	2x64	36
EXTCARD	External PC Board	–	2
BUSCABLE	Bus Cable	12x64	18
CCTD	Clock + Trigger Distr. (VME)	–	1
BUSIF	Bus Interface (VME)	3x12x64	6
FECRATE	Front End Crate (VME)	–	1
DETHV	Detector HV (CAEN A520)	16[c]	6
LV	Low Voltage (CAEN A516)	8	4
HVCRATE	High + Low Voltages (CAEN)	–	1

[a] Bipolar Amplifier and Comparator
[b] Clock Driven Pipeline
[c] only 12 actually used
* i.e., two MD units

Table 3.1: Main components of the MD in the target region

3.2 MD components

The MD is formed by two identical detectors, called MD1 and MD2. In fig. 3.1 you can see their placement in the target region of the NA50 apparatus. Each detector (MD1, MD2) is made up of 4 sensitive regions: two inner and two outer crowns.

The first inner crown (F001) has a sensitive area defined by: $r_{min} = 0.44cm \rightarrow r_{max} = 3.44cm$ (r is the distance from beam axis z). The silicon detector is glued to a multilayer printed circuit called BOARD1 which works also as a mechanical support. F001 is segmented into 36 azimuthal sectors: 18 are sensitive and 18 are used for fanout lines. Sectors are identified by a number (1 to 36) starting from horizontal axis. Sensitive (S) and non sensitive (F) sectors are in the following order: $1_F, 2_S, 3_S, 4_F, 5_F, 6_S, 7_S, 8_F, ...$ Each sensitive sector is subdivided into 128 strips. Each strip is identified by the sector number and by the *ring* number (i.e. its position going radially from the beam axis).

The first outer crown is called F002. It has sensitive area defined by: $r_{min} = 3.44cm \rightarrow r_{max} = 8.64cm$. The silicon detector is glued to a support called BOARD2. The azimuthal segmentation and the sequence of sensitive and non sensitive sectors is the same adopted for F001. Each sensitive sector is subdivided into 64 strips. The two crowns described above are repeated on both faces of MD1/MD2 (see fig. 3.4).

The only difference between the two faces of MD1 consists in the different order of sensitive sectors, that is: $1_S, 2_F, 3_F, 4_S, 5_S, 6_F, 7_F, 8_S, ...$ for the second face of MD1. In this way the ensemble F001/2+F003/4 provides a full azimuthal coverage.

The detectors are of two different kinds: in the innermost crown they are AC coupled to the front-end electronics; in the outermost one they are DC coupled. The reason of this choice will be explained in the next section. The crowns are built mounting the BOARD1s onto the BOARD2s using precision pins and then fixing the couples on a vetronite plane, that is finally installed in the mechanical support together with an outer multilayer circuit (EXTCARD), which provides the interconnections with the outside. The whole system can be moved vertically with a remote–controlled stepper motor.

3.3 The Silicon Microstrip Detectors

The design of the silicon detectors which constitute the active part of MD started in 1992. A number of detector parameters had to be specified for fabrication, and kept under control after irradiation. The main parameters taken into account in our design were: (i) input capacitance to preamplifier (includes strip and fanout line) which should not exceed $\sim$ 5 pF to ensure good signal/noise ratio (>20); (ii) leakage current which should not exceed 5 μA/strip *after irradiation* to limit shot noise; (iii) coupling capacitance (MOS capacitor made by metal/oxide and nitride/p–diffusion) which should be in excess of 100 pF/strip (20 pF would be acceptable for inner strips) to ensure correct signal collection by the preamplifier;

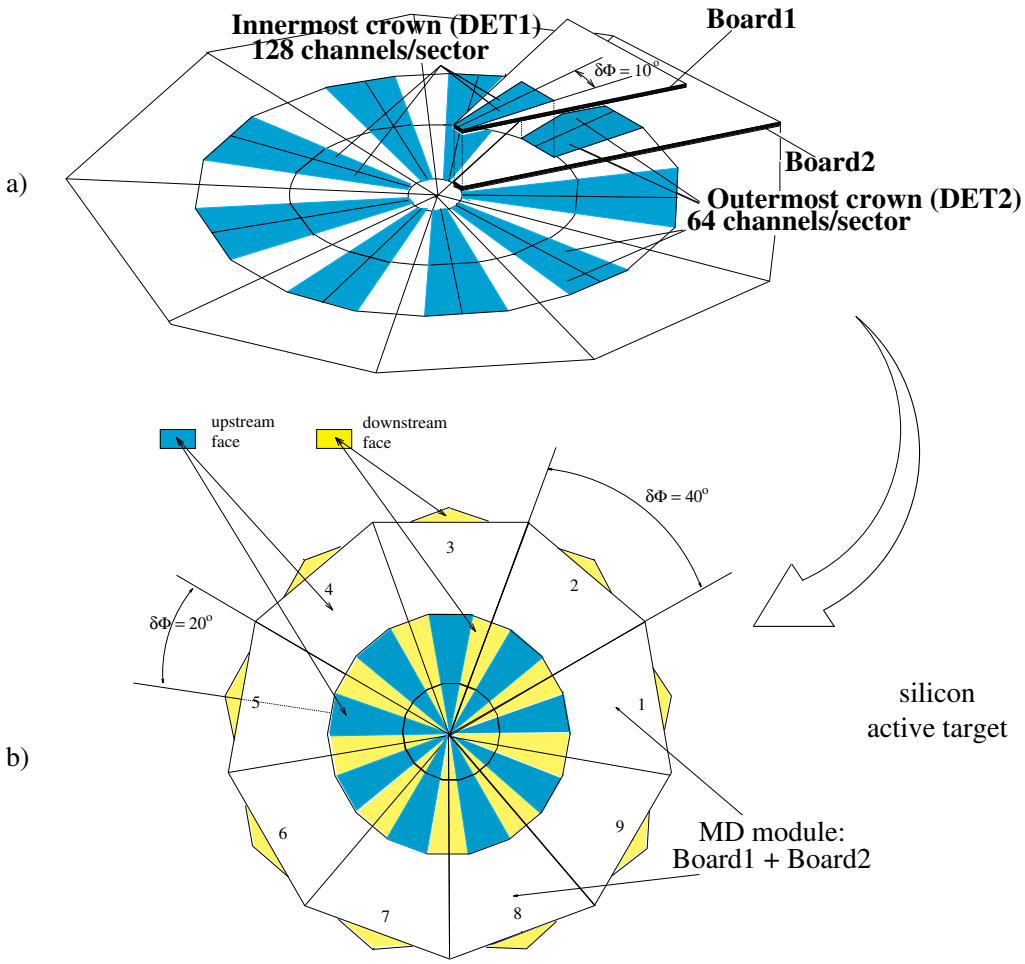

Figure 3.4: *The Multiplicity Detector structure: a) superposition of BOARD1 and BOARD2 to form a complete module, b) different position of the modules on the 2 MD faces*

(iv) bias resistance (made by polysilicon) >200 kΩ; (v) interstrip resistance which should be high enough to ensure isolation between strips. A few prototypes have been produced by S.I. to test the values reached for these parameters and then, taking into account the results of these tests, the final version of detectors has been designed and produced by Canberra. With the adopted concept for the mechanical support (modular) two detector types are needed: DET1 for the inner crown and DET2 for the outer crown. They are single side silicon strip detectors, where the strips are made of p^+ implantation on a n bulk. The ohmic contact is made of a n^+ diffusion and it is called backplane. The detector is reverse biased applying a negative voltage of about 100 V between the backplane and a bias bus, which sorrounds the sensitive area and is connected to each strip by means of integrated polysilicon resistors. Through these resistances, each of about 200 kΩ, flows the inverse current, one of the components of the leakage current. The other one, the surface current, is collected by the guard ring, a p^+ implantation which limits the sensitive area defining the shape of the electric field close to the physical edge of the detector. The AC coupling is made by MOS capacitors directly integrated on the surface of the detector by deposition of 250nm of silicon dioxide plus a layer of 1 micron of aluminum. The MOS contact prevents the leakage current to flow inside the first stage of the preamplifier which is connected throught glass fanouts bonded to the aluminum through special contacts called bonding pads.

In order to have the same pseudorapidity coverage in the whole detector, the area of the strips grows from the beam axis to the outer part of the MD. For this reason the number of strips varies in the two DETs: on each sector of DET1 there are 128 strips while on DET2 there are only 64, and DET2 is much bigger than DET1. Unfortunately, the industrial process for the SiO_2 deposition on silicon wafer is not under control, in the sense that a good homogeneity of the thickness of the dioxide cannot be guarateed by the producer on big surfaces. Hence we had to use DC coupled detectors for the DET2.

3.4 The Front–end VLSI circuits

Since only the hit/no hit information from the strips will be used, a binary readout scheme has been chosen, in which the signals are immediately discriminated and only the digital information is stored for transmission. A block diagram of the MD readout chain is shown in fig. 3.5.

The first VLSI chip, called FABRIC [2], is bonded directly to the glass fanouts and preamplifies, shapes and discriminates the signals. It is bonded to the second chip, CDP [3], which is a clock driven digital buffer working at 50 MHz and providing the storage of the information for the duration of the trigger latency of about 1 μs. The data are then stored for the whole burst (up to 5000 events) on memories in a local rack (BUSIF modules) and finally transferred to the NA50 counting room using optical links. A VME module (CCTD) generates the clock and provides the

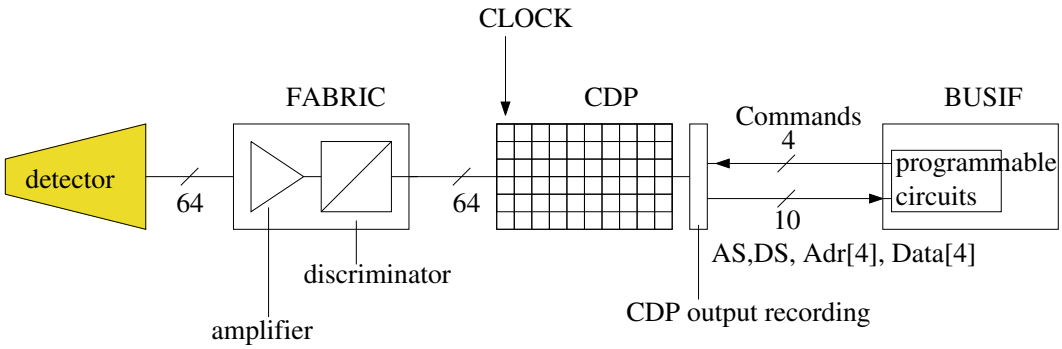

Figure 3.5: *Block diagram of the MD read–out chain*

calibration signals and the proper synchronization of the trigger signals.

The VLSI chips must have narrow channel pitch (50 μm) to limit the length of the fanouts, low–power consumption (so that local cooling could be avoided) and be radiation resistant. They were realized as full–custom 64-channel chips, FABRIC in bipolar (Tektronix) and CDP in rad–hard CMOS (Honeywell) technology. Both chips provide test–mode operation, allowing full test and calibration of the system: the FABRIC allows pulsing all channel inputs through individual 53 fF integrated capacitors, each connected to one of four calibration lines, while the CDP allows writing into the buffer through the address lines.

The maximum foreseen rates of 10^7 beam particles/s and 2x10^6 interactions/s, coupled with the high occupancy, make dead time and time resolution of primary importance for the front-end electronics. We fixed as design goals 50 ns for the dead time, based on the maximum the experiment can tolerate as loss of events for pileup protection [1], and 8 ns for the walk, to avoid losses in the digital buffer. In addition, we required that the channel to channel variation of gain and threshold values would not deteriorate significantly the system performance as compared to the single channel one.

3.4.1 The FABRIC

The working scheme of the FABRIC is shown in fig. 3.6. Since NA50 is a high–rate experiment, any gate protecting against pileup will result in a loss of events, and therefore must be kept as short as possible: as an example, at an average beam rate of 10^7 particles/s and with a target of 18% of an interaction length, the pileup of interactions is 8% in a time window of 20 ns. Given the high occupancy of the detector, the dead time must be comparably short: we obtained a value below 50 ns.

In addition, to guarantee that no losses will occur in the digital buffer which

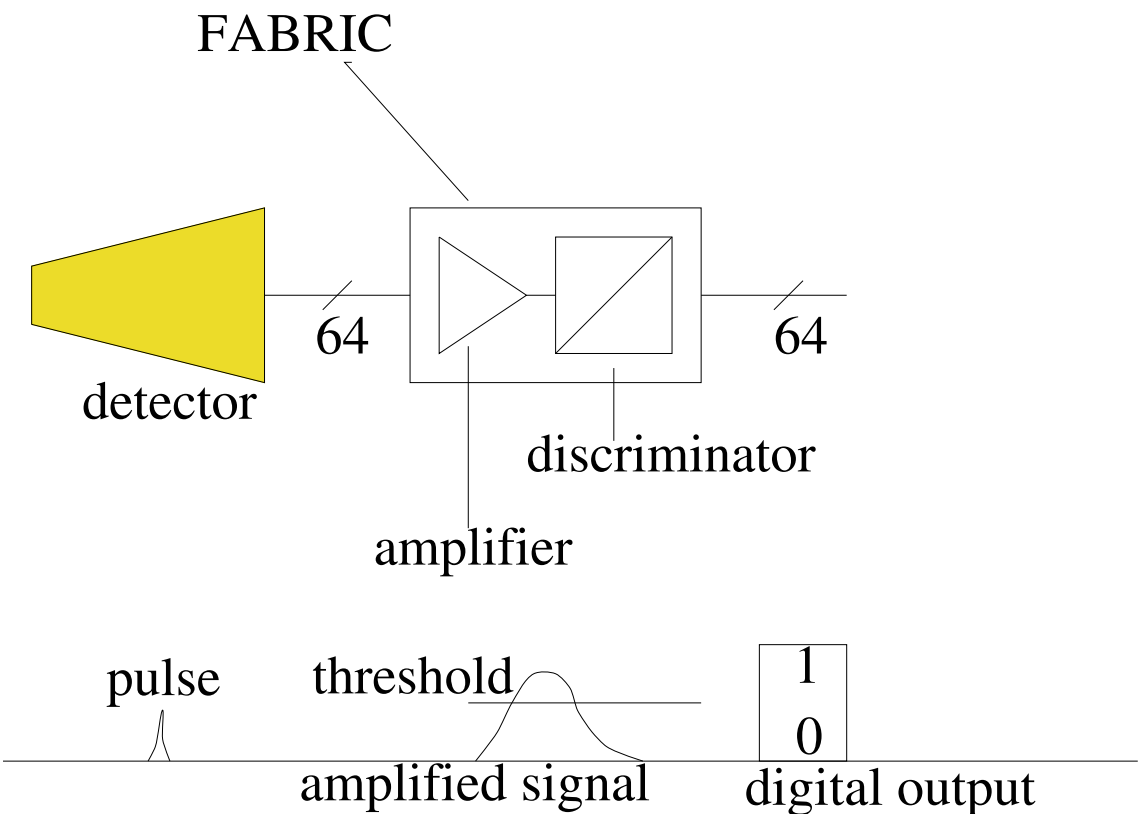

Figure 3.6: *Scheme of the FABRIC*

works at a frequency of 50MHz [3], the discriminator time walk must be kept below 8ns [1].

Let us note that both these requirements are more demanding than the corresponding ones for the front-end electronics for the LHC p-p experiments.

The layout of the NA50 silicon detectors, driven by the requirement of uniform occupancy per strip, is very unusual and results in strip capacitances ranging, including the fanout, from 0.5 pF to 5 pF within one detector chip, while the coupling capacitances, which are integrated on each strip, vary of about one order of magnitude [1]. Since there is no way to make the equivalent noise charge of a preamplifier independent of the input capacitance, the front-end electronics has been designed to satisfy the requirements on the noise at the largest input capacitance. At the same time the other parameters of the preamplifier (gain, peaking time) are kept insensitive to the input capacitance over the range mentioned above.

The duration of the current signal induced in a strip of a p-side silicon detector is equal to the hole collection time. For a 300 μm thick detector biased at 1.5 times the full depletion voltage, the collection time for the holes is approximately 25 ns, but half of the charge is collected within the first 5 ns [8]. To achieve a dead time of 50 ns, we need a shaping with effective peaking time of about 25 ns for the actual shape of the input current pulse. Our goal was to achieve a signal-to-noise ratio of 20 for minimum ionizing particles for an input capacitance of 5 pF. This value assures good detection efficiency at the lower limit of the Landau distribution of charge deposited in 300 μm of silicon by a minimum ionizing particle, i.e. 2 fC, even in presence of a significant effect of charge sharing between adjacent strips, as will be the case for the innermost strips.

At the very beginning of our project one of the ideas was to avoid implementation of local cooling system, which would be very difficult in the compact assembly of the detector, and so the limit for the power consumption was set to 100 mW per chip, i.e. 1.5 mW/channel. Taking into account the range of input capacitances, the required speed, the signal-to-noise ratio and this power constraint we concluded that a bipolar technology would be best suited for the circuit. We have chosen the full custom bipolar process SHPi by Tektronix [5] which has been proven by D. Dorfan and collaborators [6, 7] to be fully adequate for the design of low-power fast front–end electronics.

Another reason for selecting the bipolar technology is the need for good radiation resistance. Expected radiation levels for our detectors and front-end electronics in a 70–day running period [1] were up to 2 Mrad for the dose of ionizing radiation and up to 10^{13} n/cm^2 for the equivalent fluence of neutrons. Actually, values bigger than the expected ones were reached during 1996 Pb-Pb data taking period.

The output signal from the discriminator is transmitted further in a current mode and the circuit is ended up with a current mirror which has a high output impedance. This solution was chosen to reduce the possible crosstalk from the digital CMOS buffer and to reduce the level of the current signal driven by the output stage of the discriminator. A high output impedance of the discriminator is a critical point

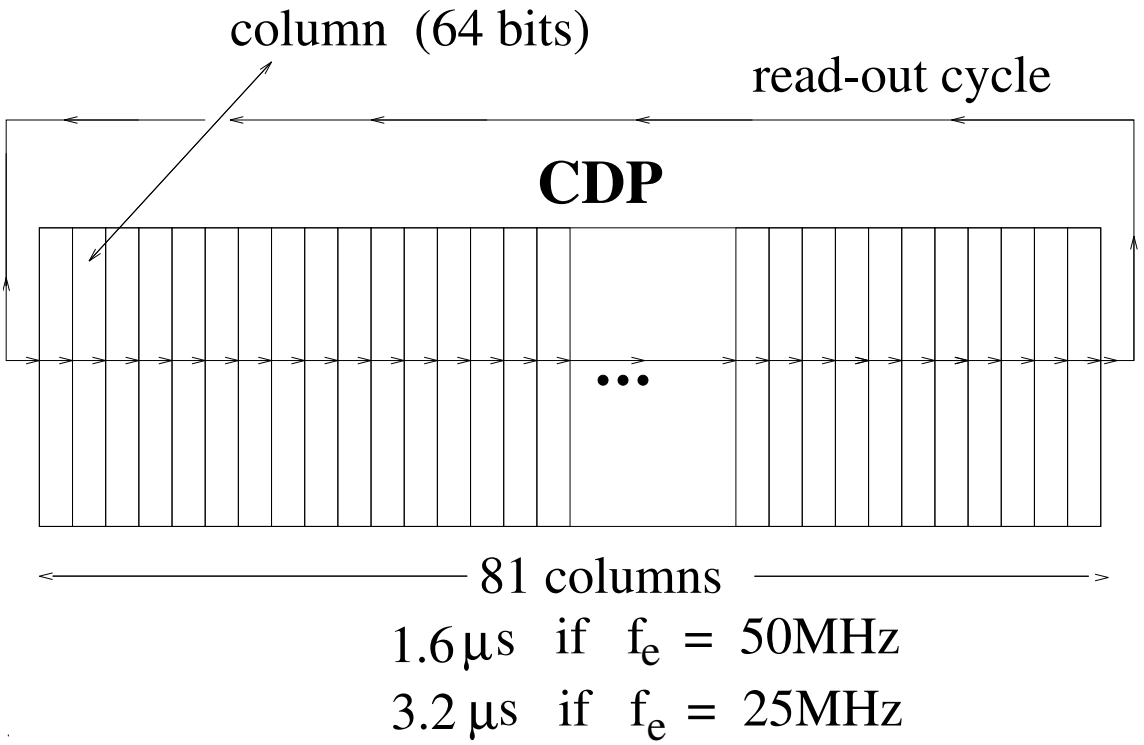

Figure 3.7: *Scheme of a CDP*

for the speed of the whole circuit and it is acceptable only for the case when the outputs of the analog front-end chip are bonded directly to the inputs of the digital CMOS buffer chip. Actually the output current mirror was designed having in mind a specific current CMOS receiver [3].

3.4.2 The CDP

The digital chip CDP (Clock Driven Pipeline) has been designed to provide the following functions:

- storage of hit pattern for the trigger latency period
- interface to the data acquisition bus

The design was completed by J. DeWitt in the summer of 1992 [3]. The functional diagram is shown in figure 3.7.

The read–out chip functions logically as a storage pipeline. The hit pattern from the FABRIC is sampled every clock cycle and passes through the pipeline. The pipeline depth is 81, and the width is 64 bits (corrisponding to the 64 output channels of the FABRIC). After the trigger latency period (see paragraph readout),

a record of the hit–pattern emerges from the far end of the pipeline and is loaded into the result register if a trigger occurs. To control the chip, the following groups of signals must be handled (all signals are in differential mode to ensure immunity from common mode noise):

- the **clock**,
- the 4–bit **command word** (cmd),
- the **bus signals**.

The command word (13 different commands out of the possible 16 are presently defined) controls the chip's operation and is executed unconditionally on the following clock cycle. On the other hand, the bus signals follow a protocol which requires a chip to be correctly addressed (i.e. the correct 4–bit chip ID code must be supplied) before any transfer of data can occur: this activity is independent from the command word.

The sampling of data present on the input pads (coming from the analog chip FABRIC) is made (or not) at every clock cycle, under the control of the command word. Usually (cmd=12) these data are written into a new RAM column. The transfer of data from a particular RAM column to the result register is also under control of the command word.

The CDP that was used in NA50 is a rad–hard version made by Honeywell. The first prototypes were processed at H.P. with 1.2 μm CMOS technology (through the MOSIS facility). The first chips were received in December 1992 and were extensively tested from January 1993. For the new version, the following changes were decided: the dynamic RAM was changed to a static RAM (better radiation resistance); the output swings were made symmetrical and increased; the accumulator register was extended to a few bits capacity.

A first rad–hard ($>$ 1 MRad) version (called UTMCCDP) was submitted to UTMC, Colorado (through the RMOSIS facility) in January 1993. This production was not satisfatory because of several problems in the production. Given the unclear prospects for future productions at UTMC, after this unsuccessful attempt we decided to discontinue production at UTMC. Another rad–hard version (called HONEYCDP) has been designed (by Joel DeWitt) and produced by Honeywell, Minnesota, U.S.A., using their 0.8 μm, three-metal rad–hard process, which seemed the most promising on the market. The external dimensions of the chip are 3.2 x 2.95 mm^2. The HONEYCDPs were successfully tested up to 50MHz clock frequency, see section 4.3.3.

3.5 The BOARDs

As written above, the silicon detectors are placed, together with the front-end electronics and electric components, on multilayer printed circuits called BOARDs. The

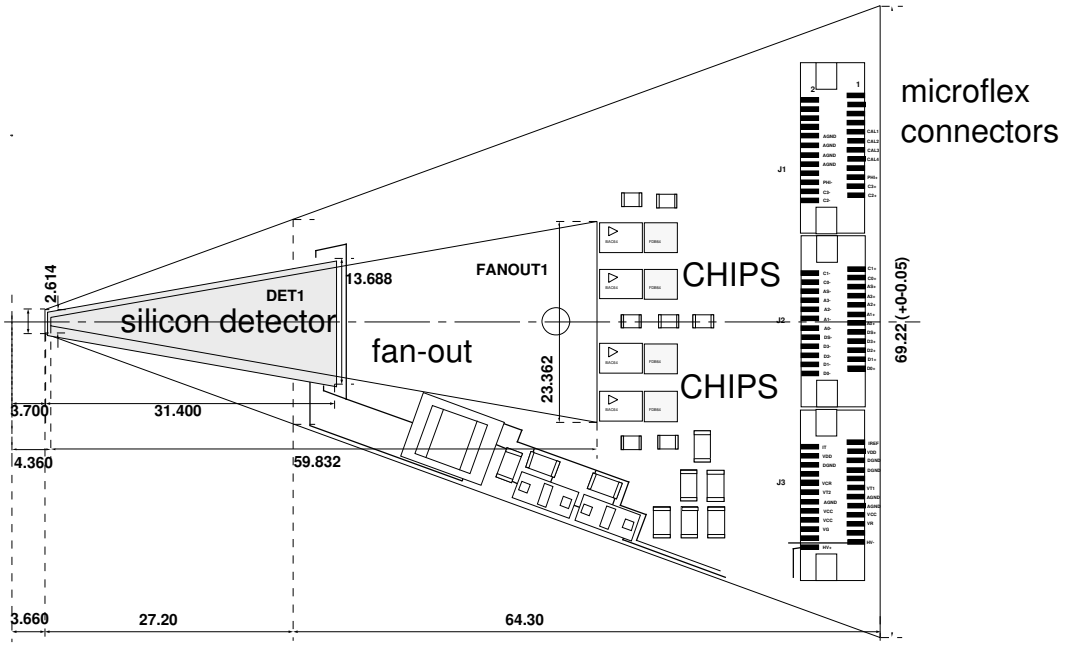

Figure 3.8: *Scheme of a BOARD1*

BOARD1 holds the inner crown detector (see fig. 3.8), while the BOARD2 holds the outer crown one (see fig. 3.9).

Mechanically, a BOARD1 is placed on top of a BOARD2 and fixed to it with precision pins. On each BOARD there are filter capacitors and other surface mounted components, as well as signal and power lines.

Each BOARD2 must relay all the signals from the overlying BOARD1 to an external distribution card (EXTCARD): this is done via a set of three kapton cables (KAPT1) which connect both to BOARD1 and BOARD2 by means of a surface–mounted connector (MICROFLEX). The BOARD2 is then connected to the EXTCARD via other kapton cables (KAPT2) and surface–mounted connectors.

A cross–section of the BOARD1 + BOARD2 assembly is shown in figure 3.10, where all thicknesses have been amplified by a factor 10 with respect to other dimensions.

The design of BOARD1 and BOARD2 has been done according to the following guidelines (from the electrical and mechanical points of view):

- the HV, Analog and Digital sections have been kept as separate as possible;
- filtering of the supply voltages is provided near the chips;
- an adequate number of wires is reserved for the high current lines (VCC and AGND, VDD and DGND) in order to avoid excessive voltage drops;

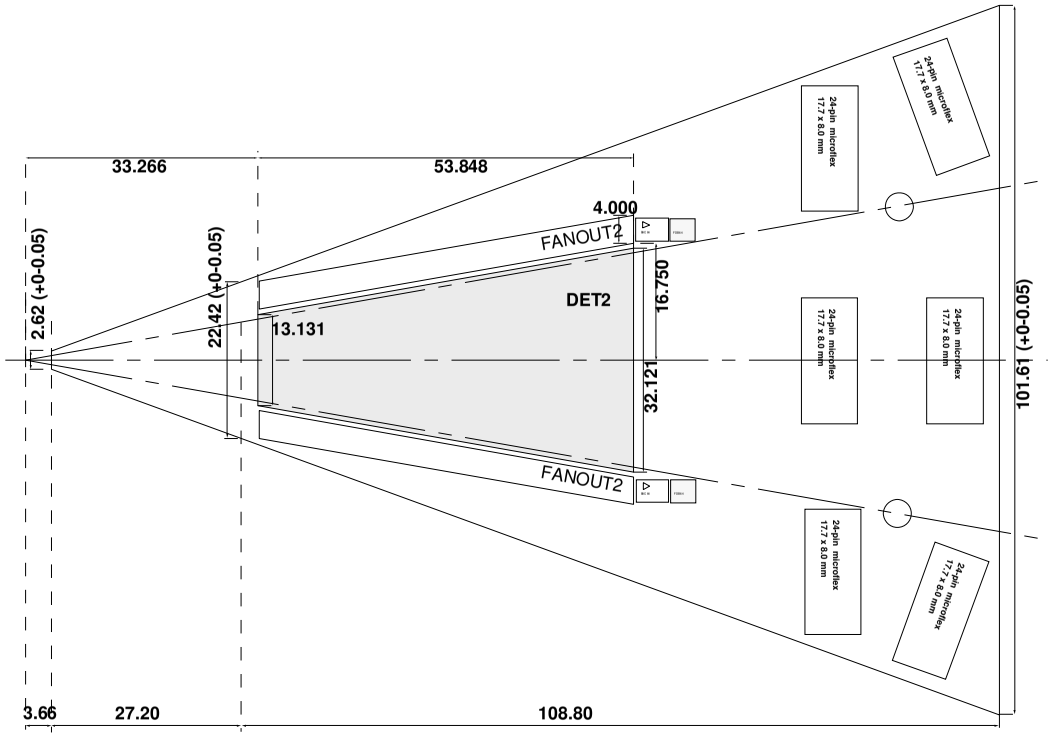

Figure 3.9: *Scheme of a BOARD2*

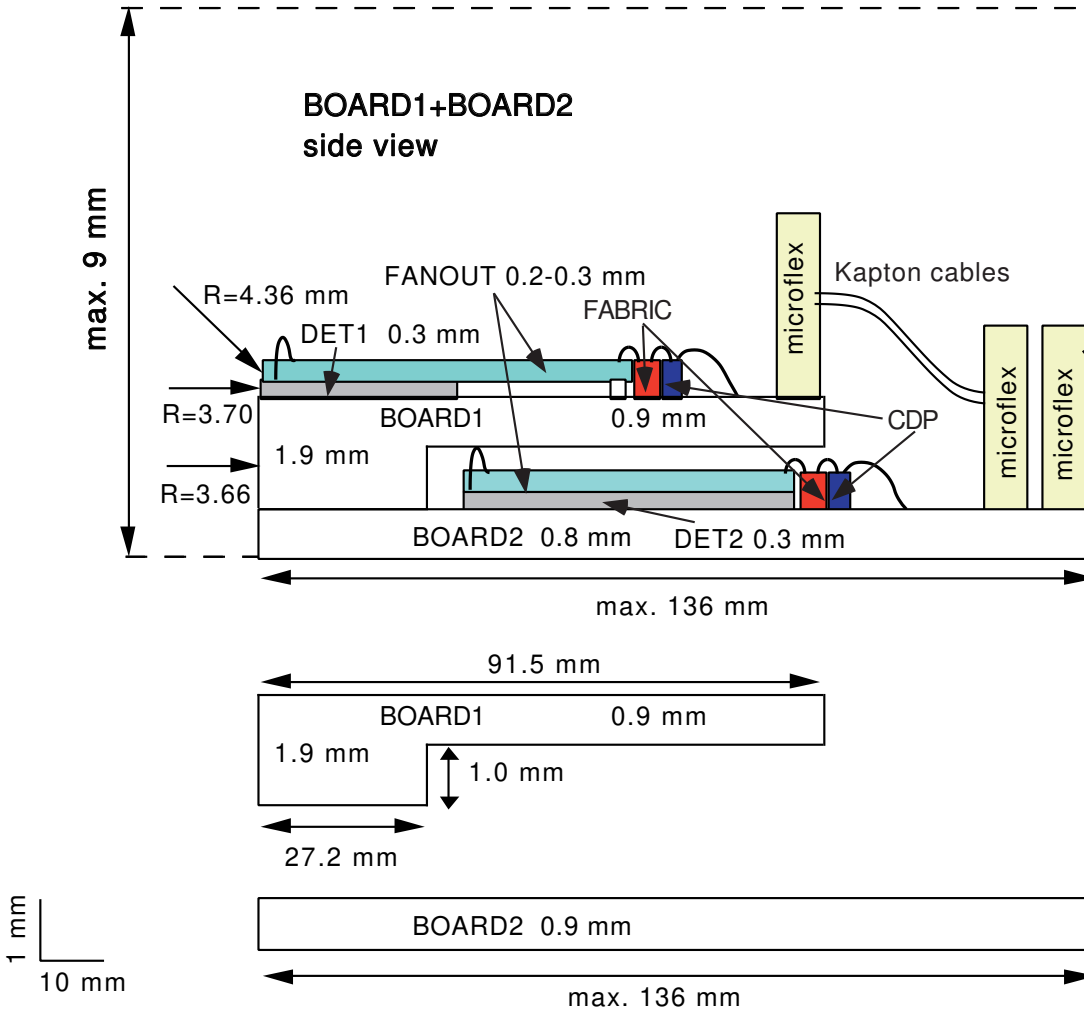

Figure 3.10: *Schematic drawing of a MD module: BOARD1+BOARD2*

- an individual analog calibration line is reserved for each calibration input of a FABRIC (this was later changed to: one independent calibration line every 2 or 4 calibration inputs located on different FABRICs);

- reference holes are provided to ensure good alignment inside a MD unit;

Both types of BOARDs have been designed in Torino and produced at CERN. Only a part of the produced BOARDs, namely 70% of BOARD1 and 90% of BOARD2 were properly working. The problems that we have encountered are presented in section 4.4. The final layout of BOARD1 is shown in fig. 3.8, while the layout of BOARD2 is shown in fig. 3.9.

3.6 The auxiliary boards and cables

Although up to 16 digital chips could be put on a single Bus Segment (thanks to the 4 bit chip address), we chose to group together 4(on a BOARD1)+2(on a BOARD2) chips from a 40° sector, and group further a front and a back sector, ending up with 12 chips per Bus Segment.

The connection from chip boards to BUSIF and CCTD modules is foreseen in a few steps, which require an auxiliary board, called EXTCARD:

- a short kapton cable (KAPT1) connects each BOARD1 to the underlying BOARD2;

- another kapton cable (KAPT2) connects each BOARD2 to the EXTCARD;

- on the EXTCARD, signal lines from a "front" and from a "back" BOARD2 are merged to form a single Bus Segment;

- each EXTCARD is connected to three BUSIF modules via Bus Cables (about 5 m long twisted pairs);

- each EXTCARD is connected to the CCTD with two cables providing the Clock and Calibration signals, respectively;

- each EXTCARD is connected to the low and high voltage power supply modules via four LV cables and three HV cables.

Due to the severe space limitations, and to the number of signals, all connections inside a MD unit up to the external cards (but excluding the Bus Cable connectors) must conform to a 0.020" pitch. This is implemented with kapton cables (designed by us) and surface–mounted connectors (Microflex from DuPont).

Sensitive signals (i.e. the clock and the analog calibration signals) are distributed via shielded cables from their source until (at least) the EXTCARD.

In order to minimize the number of wires and therefore the number of connectors, we need some fanout stages for signals and DC voltages. For signals, the fanout

may be either passive or active, depending on circumstances. In general, the fanout factors for **control/bus signals** and for **low voltages** are the following:

- 3x at BOARD2 (2 chips on board + 1 to BOARD1 via KAPT1)
- 4x at BOARD1 (4 chips on board)

Detector **high voltages** do not have any fanout, while **calibration signals** (one independent signal every two or four FABRIC calibration input) have their fanout implemented on EXTCARD via analog multiplexers.

In addition, the **clock** signal received on EXTCARD is translated there from ECL standard to the non–standard levels needed by the digital chip and sent to each of the 9 Bus Segments.

3.6.1 The EXTCARD

The geometrical layout of EXTCARD is shown in fig. 3.11. The purposes of this card are:

1. distribution of HV
2. distribution of LV
3. multiplexing and distribution of Calibration signals
4. level translation and distribution of Clock
5. distribution of Bus and Control signals

Each EXTCARD is connected to the CCTD, to three BUSIF modules, to two A516 modules and to three A520 modules. Each EXTCARD is also connected to 18 BOARD2 via 18 KAPT2 cables (in fact, each KAPT2 cable is physically realized with three separate 24-lead pieces of kapton).

The ground plane of EXTCARD represents the common ground point for a whole Multiplicity Detector unit. All low voltages are regulated by a couple of sense wires (see the Caen A516 manual for more details) up to the EXTCARD input. Due to the required precision on the two voltages determining the FABRIC threshold, namely VT1 and VT2, these two voltages are generated at three times the desired value at the power supply, and then divided by three on the EXTCARD.

The Calibration fanout (a factor of 9) and multiplexing (to one out of 16 possible destinations) is implemented on EXTCARD.

The Clock translation to the logic levels required by the CDP and the fanout (by a factor of 9) is also implemented on EXTCARD.

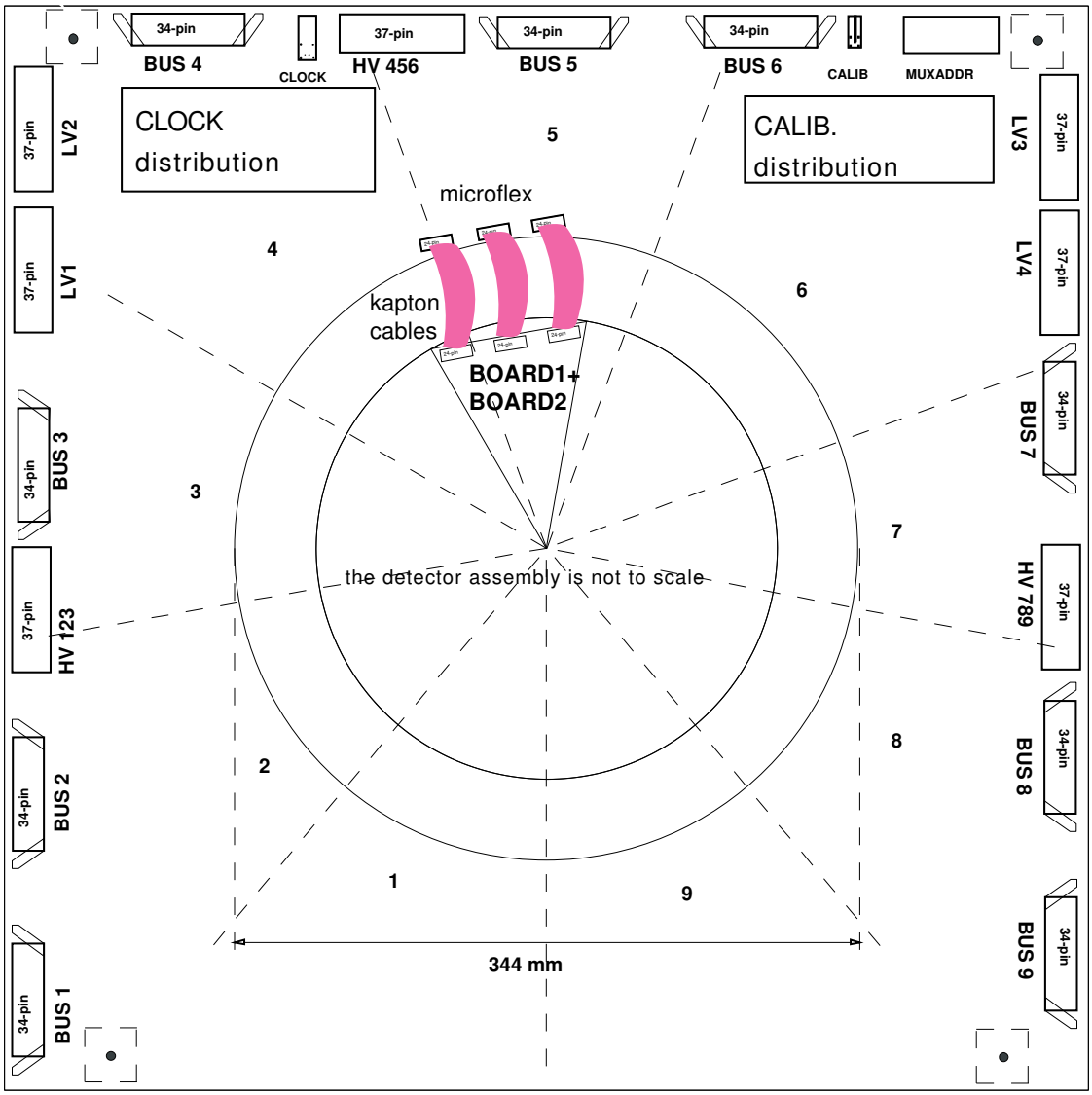

Figure 3.11: *Scheme of the EXTCARD*

3.7 Front–End Control Modules

The Front–End control modules provide the following functions:

1. transmission of DC voltages to detectors and chips;
2. generation and transmission of the clock (50 MHz) to digital chips;
3. generation and transmission of calibration signals to analog chips;
4. transmission of the trigger (by commutation of the control word) to digital chips;
5. generation of a readout sequence in response to a signal from the Data Acquisition System;
6. generation of a write/read back test sequence for the digital chips;
7. storage of event information for a whole burst in a buffer (5000 events maximum);
8. transfer of the burst buffer to the Data Acquisition System at end of burst.

These functions are performed by two kinds of VME modules, placed in one double–depth VME crate located a few m away from the detector units:

- the Calibration, Clock and Trigger Distribution (CCTD) module;
- the Bus Interface (BUSIF) module.

3.7.1 The CCTD module

The CCTD module (Calibration, Clock and Trigger Distribution) has been developed by INFN Torino, and controls two important features of the read–out: it generates a clock signal of frequency f_e (variable from 391 kHz to 50 MHz) which is responsible for the incrementation of the column pointer in the CDP; then it generates a trigger signal corrisponding to the general one delayed by a value equal to δt_{trig}. This delay can be fixed *a priori* since it is well known, and it is measured in column units (from 0 to 127). Then it is sent to the BUSIF module, and after another delay of about 20 ns a command is sent to the CDP and used to stop the sampling of the RAM. The time at which the signal gets to the CDP is called t_{trigMD} and in fig. 3.12 the scheme of different delays and CDP read–out synchronization is shown.

The CCTD module (see the block diagram in fig. 3.13) distributes the following signals: (a) Calibration Out, Clock and Multiplexer Address to EXTCARD, (b) Trigger Out to BUSIF modules, (c) Caltrig to the Trigger System. The CCTD receives a Trigger In signal from the Trigger System. The Calibration Out feature was

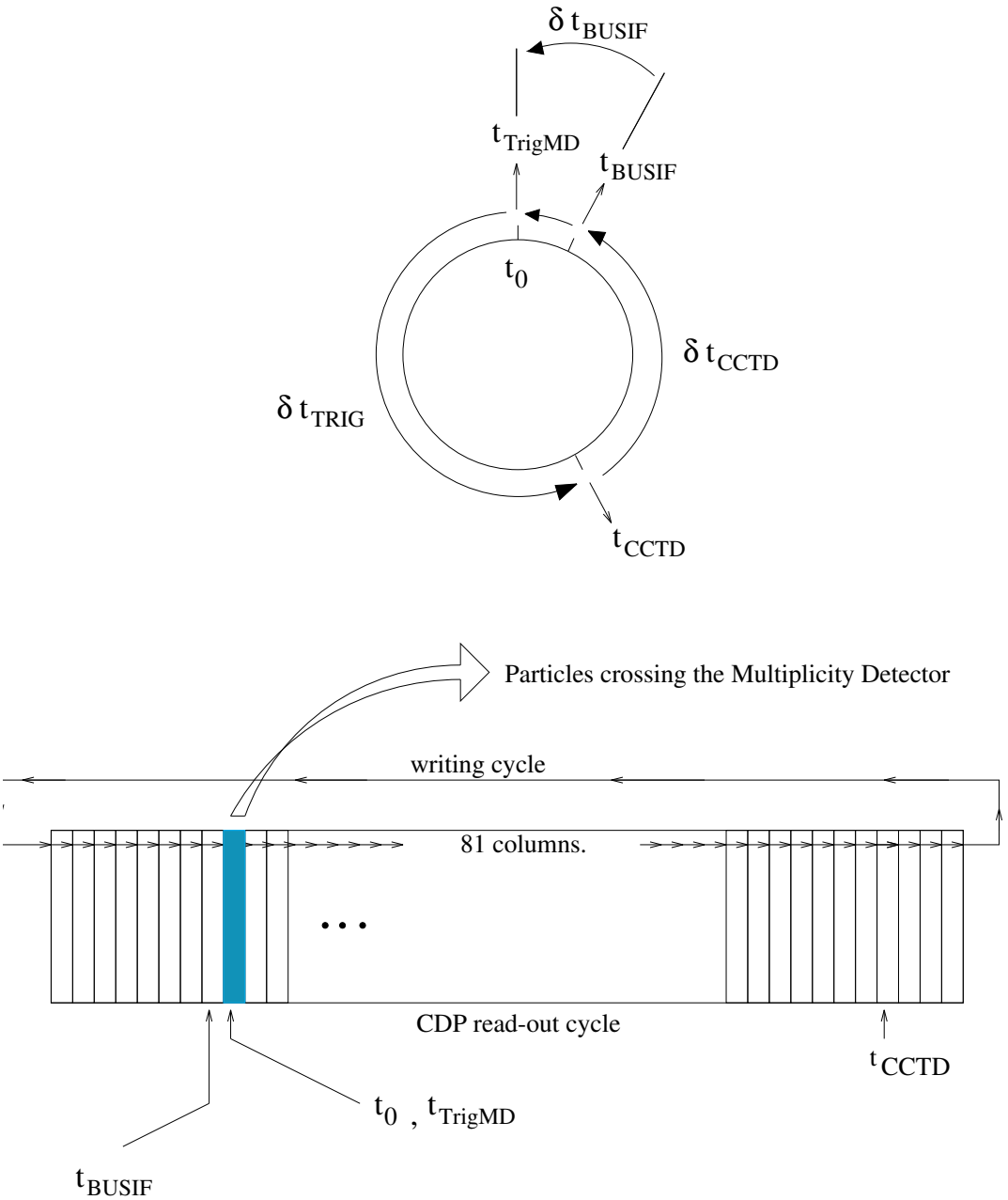

Figure 3.12: *Scheme of the read–out synchronization*

CCTD

Calibration, Clock and Trigger Distribution module

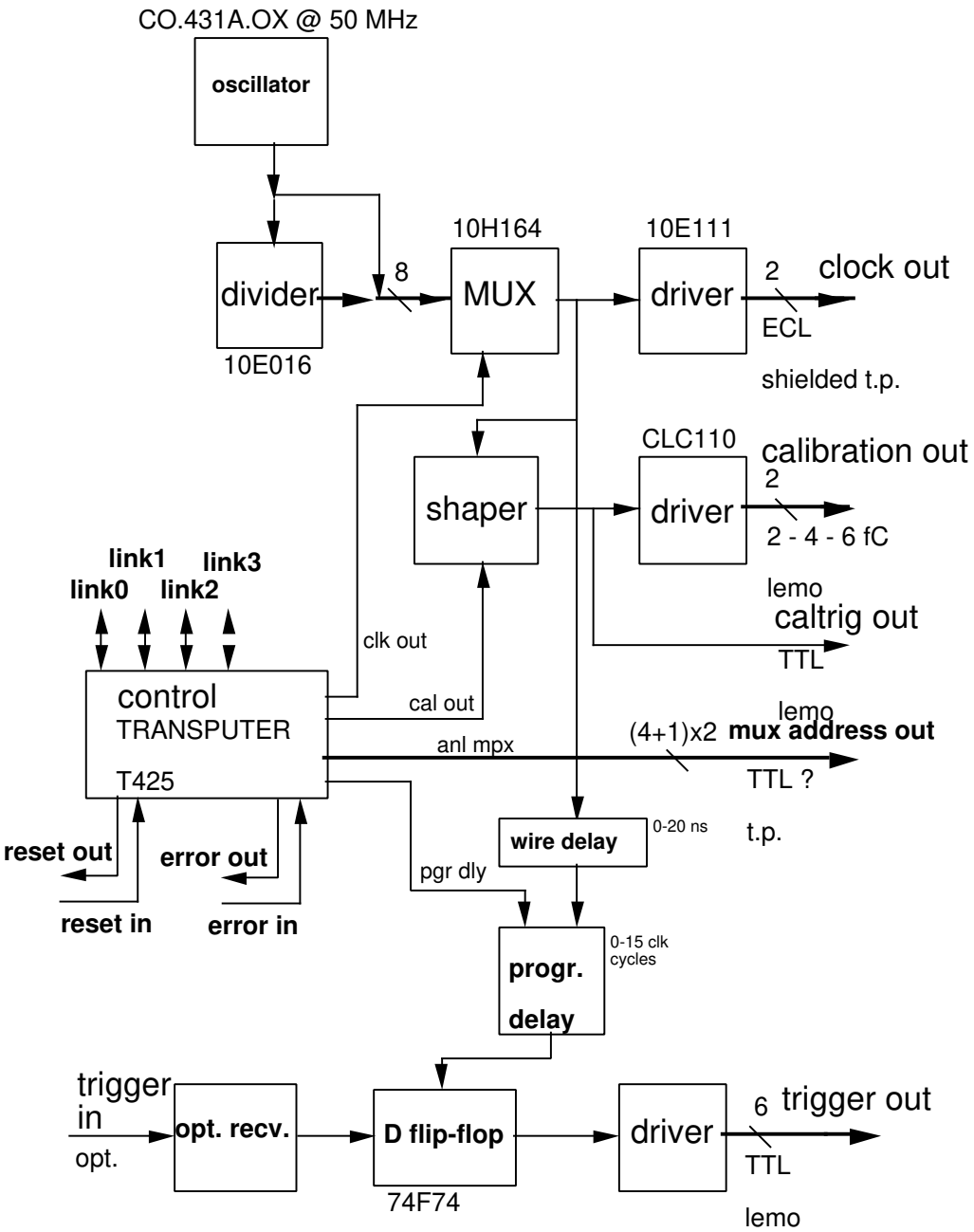

Figure 3.13: *Scheme of the CCTD module*

not used in the experiment due to the excessive noise introduced by the calibration pulse.

A T425 transputer inside the CCTD controls: (i) the clock frequency, (ii) the amplitude of the Calibration Out signal (providing analog chips with the equivalent charge of 0.5, 1.0 and 1.5 minimum ionizing particles), (iii) the Multiplexer Address (for routing of Calibration Out signals to different chip inputs) and (iv) the delay between Trigger In and Trigger Out.

The communication with the Data Acquisition System is provided via the four bidirectional Transputer Links available on the J2/P2 connector. These links will be used both for initial program loading at bootstrap and for program–to–program communication during acquisition.

3.7.2 The BUSIF module

The BUSIF (BusInterface) has ben developed by M. Forlen at L.A.P.P. Annecy and is used to read the data coming from the digital chips of the MD, the CDPs. It is the interface between the detector and the transputers of the data acquisition system.

Each BUSIF can be divided into two main parts:

- read–out component
- transfer component

The BUSIF is connected to the EXTCARD via twisted pair cables (BUSCABLEs) for the control and bus signals, and receives a Trigger from the CCTD. The BUSIF module houses a T425 transputer with four bidirectional 10 Mbit/s links. Each BUSIF module is dedicated to 3 Bus Segments (12 chips per Segment) and provides enough FIFO storage for a whole burst; 6 BUSIFs are thus necessary to read out the complete Multiplicity Detector (see fig. 3.14).

3.8 Power supply

The low voltage power requirements have been calculated from measured currents in the two chips, allowing for some safety margin.

The Low Voltage Power Supply is implemented with a CAEN SY527 mainframe and four A516 plug–in modules with 8 channels each at 12 V, 1.5 A.

The SY527 mainframe occupies a crate 19" (48.36 cm) wide, 8 units (36 cm) high and 69 cm deep; it can house up to 10 modules. The SY527 can be remotely controlled either via an RS232 port at 9600 baud (default) or via a half–duplex CAENET link on a 50 Ω coaxial cable.

During 1996 Pb-Pb run we used a remote control system based on a IBM–compatible PC placed in the NA50 counting room and also a direct manual control in the ECN3 experimental area. An A516 module provides 8 channels at 12 V, 1.5

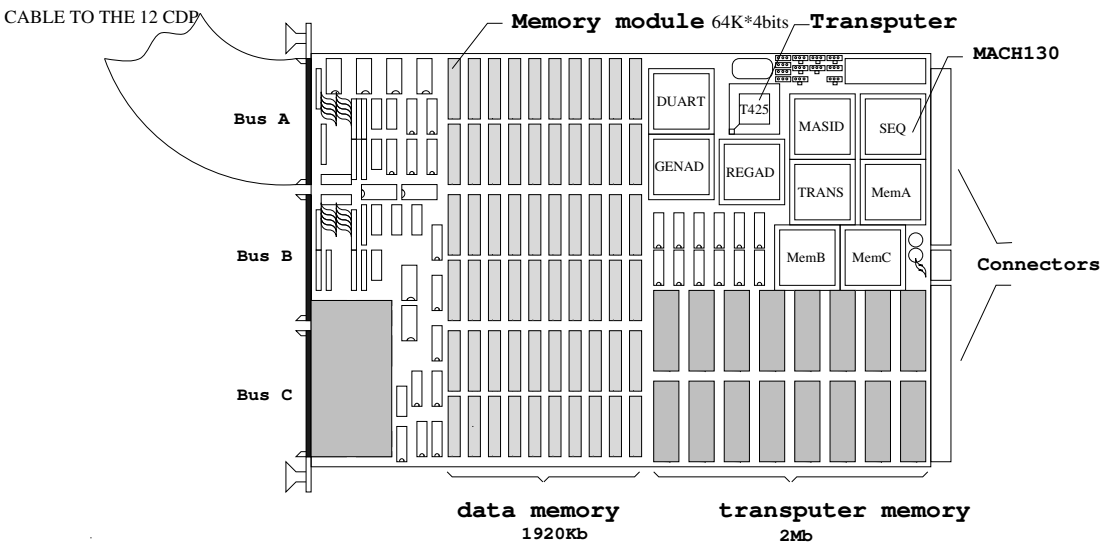

Figure 3.14: *Scheme of a BUSIF module*

A on two 37–pin D–type female connectors, for a total of 8x2 outputs and 8x2 sense inputs.

The LV channel assignment for MD1 is given in table 3.2, where the Slot number 6 or 7 refers to the A516 module position inside the SY527 crate; an identical setup is used for MD2, usign Slots 8 and 9. The VCEXT, VEEXT voltages are used by discrete components on the EXTCARDs and on the Adapters (VCEXT is duplicated due to the high current needed); the digital chip uses VDD as a supply voltage, and the remaining voltages are used by the analog chip.

The precision needed for the FABRIC threshold voltages VT1, VT2 is a little bit better than the A516 specifications; it is then achieved by using a higher voltage (3x) at the A516 level and a voltage divider on the EXTCARD.

The High Voltage Power Supply is implemented with the same CAEN SY527 mainframe as for the LV and A520 plug–in modules with 16 channels each at 200 V. Each detector is biased independently using a single channel; on each A520 module 12 channels are used for the detectors belonging to a group of 3 consecutive readout Bus Segments. The assignment of channels for MD1, which uses Slots 0, 1 and 2 of the mainframe, is listed in table 3.2; again, an identical setup is used for MD2 by using Slots 3, 4 and 5.

Is is seen that to power each unit of the MD three A520 HV modules and two A516 LV modules are needed, so that to power the whole MD one has to fill all the 10 available slots of a SY527 mainframe.

3.9 Data synchronization

In this section I will explain how the data coming out from the MD are read by the front–end chips and then sent to the acquisition system in the counting room. The NA50 $\mu\mu$ trigger is defined by the R_1, R_2, R_3, R_4 hodoscopes which are placed almost 6 m downstream the MD. Hence, if the products of the collision cross the MD at $t = t_0$, we will know this only after a certain time δt_{trig}. This value can be evaluated summing its different components:

$$\delta t_{trig} = T_{flight} + T_{R1} + T_{trig} + T_{send} \tag{3.1}$$

where

- T_{flight}=20 ns = time of flight of muons between MD and the trigger hodoscopes;
- T_{R1}=260 ns = time between data output from hodoscopes and input to discriminators;
- T_{trig}=300 ns = time between discriminators output and production of trigger signal in the counting room;
- T_{send}=356 ns = time needed to bring the signal down to the experimental area (80 m) via an optic fiber.

The sum of these times leads to a maximum value for δt_{trig} of 1000 ns. This time is called trigger latency time. Hence, during the time interval (t_0, $t_0 + \delta t_{trig}$) we must be able to memorize the MD data with the best possible time resolution. This is performed by the CDP.

Since the the duration of the FABRIC comparator signal is of 40 ns, the minimum value for the sampling frequency (f_e) is 25 MHz. This is the frequency used for 1995 run, while in 1996 we passed to 50 MHz. Starting from the trigger latency time (1000 ns), we can evaluate the minimum number of data array, called column (each one contains the 64 channels of a FABRIC) present in a CDP.

$$N_{min} = \delta t_{trig} x f_e \tag{3.2}$$

For a value of f_e = 50 MHz, N_{min}=50, but the CDP has 81 columns so it works perfectly even at this high frequency (see 3.4.2). In this way we have the possibility to remember the state of the MD during 1.6 μs at 50 MHz and 3.2μs at 25 MHz. These values are compatible with the trigger latency time. For each trigger generatd by the experiment only one column out of the 81 present in the RAM must be memorized: the one corrisponding to the passage of the particles into the MD. To store the right column we follow the following procedure:

- 1 stop the sampling of the RAM

- 2 identify the right column
- 3 store the data in a special memory.

All these operations are done sending *ad hoc* commands to the CDP by means of external modules: the BUSIF and the CCTD.

Cable	Slot	Channel	Assigned to module.bus.det	Nominal Voltage	Approximate Current limit
LV1	6	0	VCC.MD1.bus123	3.5 V	1.1 A
	6	1	VDD.MD1.bus123	5.0 V	1.1 A
	6	2	VR.MD1	1.8 V	10 mA
	6	3	VCR.MD1	2.0 V	0.65 A
LV2	6	4	VCC.MD1.bus456	3.5 V	1.1 A
	6	5	VDD.MD1.bus456	5.0 V	1.1 A
	6	6	VCEXT.MD1	5.2 V	1.0 A
	6	7	VEEXT.MD1	-5.4 V	1.5 A
LV3	7	0	VCC.MD1.bus789	3.5 V	1.1 A
	7	1	VDD.MD1.bus789	5.0 V	1.1 A
	7	2	VG.MD1	6.2 V	10 mA
	7	3	spare		
LV4	7	4	3VT1.MD1	9.6 V	100 mA
	7	5	3VT2.MD1	10.5 V	100 mA
	7	6	spare		
	7	7	VCEXT.MD1	5.2 V	1.0 A
HV123	0	0,2	HV.MD1.bus1.u/d.b1	120 V	
	0	1,3	HV.MD1.bus1.u/d.b2	80 V	
	0	4,6	HV.MD1.bus2.u/d.b1	120 V	
	0	5,7	HV.MD1.bus2.u/d.b2	80 V	
	0	8,10	HV.MD1.bus3.u/d.b1	120 V	
	0	9,11	HV.MD1.bus3.u/d.b2	80 V	
HV456	1	0,2	HV.MD1.bus4.u/d.b1	120 V	
	1	1,3	HV.MD1.bus4.u/d.b2	80 V	
	1	4,6	HV.MD1.bus5.u/d.b1	120 V	
	1	5,7	HV.MD1.bus5.u/d.b2	80 V	
	1	8,10	HV.MD1.bus6.u/d.b1	120 V	
	1	9,11	HV.MD1.bus6.u/d.b2	80 V	
HV789	2	0,2	HV.MD1.bus7.u/d.b1	120 V	
	2	1,3	HV.MD1.bus7.u/d.b2	80 V	
	2	4,6	HV.MD1.bus8.u/d.b1	120 V	
	2	5,7	HV.MD1.bus8.u/d.b2	80 V	
	2	8,10	HV.MD1.bus9.u/d.b1	120 V	
	2	9,11	HV.MD1.bus9.u/d.b2	80 V	

Table 3.2: Low Voltage channels for the Multiplicity Detector

Bibliography

[1] Study of Muon Pairs and Vector Mesons Produced in High Energy Pb-Pb Interactions, Proposal CERN/SPSLC 91-05, SPSLC/P 265, October 1991

[2] W. Dabrowski et al., Fast Bipolar front–end for binary readout of silicon strip detectors, Nucl. Instr. and Meth in Phys. Res. A 350 (1994) 548

[3] Joel DeWitt, A pipeline and bus interface chip for silicon strip detector read–out, Internal Note, SCIPP, Santa Cruz, CA.

[4] V.Capony, Ph.D. Thesis, Savoy University, Annecy-Le-Vieux Cedex, France (1996)

[5] Tektronix INC., Beaverton, OR 97077

[6] E.Barberis et al., Nucl. Phys. B, Proc. Suppl. 32 (1993)

[7] E.Barberis et al., IEEE tran. Nucl. Sci. 40 (1993), 740

[8] W. Dabrowski and M. Idzik, Second-order effects in front-end electronics, Technical Note RD20/TN/15, CERN, 1993

Chapter 4

Laboratory tests on MD components

4.1 Introduction

To verify the good quality of each component of the detector, we have performed detailed laboratory tests before assembling the detector in its final configuration. Then, after the Pb-Pb data taking period (Oct.-Nov. 1996) the detector has been dismounted and other tests have been made to verify the effects of radiation on chips and silicon detectors. In this chapter I will describe methods and results of these tests, including the problems that came across during the assembling procedure.

4.2 Test of detectors

The following tests have been performed on all detectors before assembly (i.e., before gluing to board and bonding to analog CHIP):

1. visual inspection under a microscope;

2. measurement of electrical parameters (C–V and I–V curves) at the probe station (Alessi mod. REL–3200) with shielded probes and picoprobes and the following instruments: (i) HP 4145B Semiconductor Parameter Analyser, (ii) Keithley 237 power supply, (iii) HP 4284A variable frequency (20 Hz – 1 MHz) LCR meter.

For a detailed description of the measurements see [2]. As told before the detectors have been produced by Canberra (Olen, Belgium) on NTD (Neutron Transmutation Doped) silicon bought from Chemitronic. From the results of the tests we can deduce that both materials and production process were of good quality. Actually only very few detectors (about 2%) had been discarded, and the main problem was that the corners were not well shaped, which caused an increase of the leakage current. In

addition, the working parameters (depletion voltage, leakage current) turned out to be very homogeneous among different strips of the same detector but also among different detectors. This allows us to polarize all the detector of the same kind at the same voltage. The found variations, of the order of 10%, can be related to the different conditions (mainly different temperature) in which the tests have been performed.

4.3 Test of front-end chips

Both initial debug and mass testing of the two CHIPs have been done at I.N.F.N. and COREP–LETEO (Available measuring instruments at COREP–LETEO: Schlumberger IDS 3000 Electron Beam Testing, HP 82000 IC Evaluation System) in Torino.

The available measuring instruments at I.N.F.N. Torino include:

- Alessi REL–4500 probe station (semiautomatic)
- HP 6626A precision power supply (4 channels)
- Tektronix PG2010 and HP 8082 pulse generators
- LeCroy 9109 function generator
- Tektronix TDS 520 and HP 54111D digital osciloscopes
- LeCroy 8901A CAMAC to GPIB interface.
- CAMAC modules: (i) CAEN C193 32–ch. ECL discriminator, (ii) LeCroy 4434 32–ch. ECL scaler, (iii) LeCroy 2229 8–ch. ECL 11–bit TDC (4 modules)
- Tektronix DAS 9200 logic state analyser

Most of the individual instruments and all the CAMAC equipment are controlled via Labview 2 software from the Macintosh.

4.3.1 Testing FABRICs

Tests for the analog chip included:

- noise by threshold scan, gain, time walk (all channels)
- dead time, output signal shape (few channels)
- cross–talk, calibration capacity homogeneity, gain and noise by TDC (few channels on few chips)

Comprehensive tests (for a few chips only) required the chip to be mounted on a specially designed board, while mass tests have done using a custom probe card mounted on the Alessi REL-3200 probe station.

1. **Test set-up for few units:**

   (a) pulsing and measurement chain including: precision power supply, pulse generator, switching matrix, discriminator, scaler, TDC;

   (b) chip under test mounted (i) on a dual–in–line 40–pin chip carrier (only a few channels may be connected) or (ii) on a Pin Grid Array or (iii) on a prototype experiment board (see also section 4.2)

2. **Set-up for Analog CHIP mass testing:**

   (a) the pulsing and measurement chain quoted above;

   (b) a probe card holder (M.A.T. mod. RAC–12 for 4.5" wide cards,

   (c) two probe cards: two versions are needed, each serving 32 channels out of 64, due to a practical limit of 100 μm pitch

The measurements of the basic parameters of the circuit show that they are very close to the simulations.

To test the stand alone chip it is necessary to provide pull-up resistors for the output stages. For the preliminary test the chip was mounted on a specially designed board providing filtering of the power supplies, mounting for capacitors to simulate the detector at the inputs and emitter followers to allow the outputs to be fed to standard electronics. The emitter follower has a rise time much slower than the one which would be obtained connecting the chip directly to the next stage as in the final configuration. The need to maintain short leads limits the number of followers on the board to four, so the whole chip was tested by subsequently bonding four channels at a time. A relatively small value of the pull-up resistors (1 kΩ) has been chosen to reduce the slowing effect of the stray capacitance at the output nodes. This value determines the amplitude of the signal at the discriminator output, but only for this particular test set-up. The obtained value of 100 mV confirms that the output current signal is of about 100 μA as was assumed in the design.

The simulation of the amplifier response for the described above pulser signal shows that the peaking time is by 4 ns longer and the amplitude is 10% lower compared with the situation when an ideal step voltage is applied.

The signals at the integrator and the discriminator outputs were taken directly from the chip by means of a picoprobe which introduces some additional, but negligible, capacitive load at the measured nodes.

The output of the discriminator was, however, loaded by the input capacitance of the emitter follower that was connected to the output node. The total capacitance at the output node in this test set-up was evaluated to be of about 10 pF, while in

the final set-up the expected total capacitance at the output node should be below 1 pF. For input signals from 1.5 fC up to 16 fC the time walk is below 8 ns.

The equivalent noise charge (ENC) of the circuit has been evaluated, as described in [1], by measuring of the counting rate as a function of the input charge at a fixed threshold of the discriminator. In this way we measure directly the error function of the noise at the amplifier output. Taking this measurement for two different values of the discriminator threshold we can evaluate also the gain of the amplifier. The average values are 440 e^- for the ENC, without external load, and 100 mV/fC for the gain. The above values for gain and noise include the ballistic deficit due to the non-zero rise time of the test pulse. For an ideal input step voltage we can expect the gain to be 5% higher and the noise 5% lower.

As it was mentioned before, for this design the uniformity of the parameters across the channels is as important as the parameters for an individual channel. Therefore we performed the measurements of all basic parameters, i.e. gain, noise, effective threshold and walk for all 64 channels of a chip. The measurements of the gain and noise in the tests are directly dependent on the values of the individual calibration capacitors belonging to individual channels. Thus, these capacitors have been measured first and a very good uniformity of 0.6% (1σ) has been found, i.e. below the level of 1σ of the noise.

The spread of the gain values is 5% (1σ) and that of the noise is 3.4%. The effective threshold of the discriminator is the difference of the dc potentials on both outputs of the differential amplifier (collectors of Q10 and Q11) and it is influenced by the output offset of the amplifier as well as by the input offset of the discriminator. The measurements have been done probing directly the probe pads placed at the amplifiers outputs; those, however, are open only in every third channel to not destroy too much the passivation layer and therefore we have a limited statistics of 22 channels. The spread of the threshold values is 2.4% (1σ) and it is small compared to the variation of gain (we have verified that the two are uncorrelated).

4.3.2 FABRIC Mass tests

A systematic check of gain and noise for each FABRIC has been performed. We used the set–up described above (for details see [3]) and the contacts on the chips were done using a custom probe card. At the beginning we planned to check all 64 channels, and for this reason we produced 2 probe cards, each serving half of the channels. Time problems led us to the choice of testing only 32 channels chip. The tests pointed out the fact that the characteristics of the chips had not a good homogeneity: in particular we noticed that the value of noise and gain were similar among chips close one to the other on the silicon wafer. It was possible to distinguish different areas on the same silicon wafer with different characteristics. For example, on some wafers, it is possible to recognise a zone in which all the chips had a very low gain. For other wafers the chips with high noise were localised mainly along the edge of the wafer. We had to fix a criterion to select the chips to be used in

the experiment. We chose to discard chips with a value of noise higher than 600 e^- and those with a gain less then 80 and bigger then 120. Following this criterion we discarded almost 30% of the tested chips.

4.3.3 Testing CDPs

Tests done on digital chips include:

- test of RAM + output register by writing a defined pattern using the data–acquisition bus (chip in test mode)
- test of the real operating mode by stimulating the inputs (chip in data–taking mode)
- test of the accumulator register

In general, the first few chips are tested in packaged form at full clock speed, and later on more chips are tested as bare dies, usually at reduced speed. Different test set-ups have been implemented:

1. **Test set-up for few units:** this is in place at COREP–LETEO, it includes the HP 82000 machine for stimulus and readout up to 25/50 MHz (chips must be bonded to a chip carrier) and the simultaneous possibility to observe signals on the CHIP with Schlumberger IDS 3000 (electron beam testing); of course the chips cannot be reused for the experiment. The latest version of the digital CHIP has been mounted on a 120–pin PGA (by Kyocera) and has been interfaced to the HP 82000 motherboard through a daughter board designed by us.
2. **Set-up for Digital CHIP mass testing:** this is being set up, using the semiautomatic Alessi REL–4500 probe station and a custom probe card. this test cannot be done at full clock speed due to the greater length of connections. A Tektronix 9220 logic state analyser has been used to drive the CHIP.

Results of the tests done on the first non rad–hard chip (HPCDP, fabricated by H.P. in 1.2 μm technology) are summarised in the following, for more details see the full reports [8] [9]. The chip was bonded to an easily available DIP chip carrier having only 40 pads, so that only 4 of the 64 input pads were connected.

The pin configuration was set up by software in the HP 82000 test machine, which allows to define the signal direction as seen from the chip (input or output), the logic "0" and "1" levels (for input pins), the logic "0" and "1" thresholds (for output pins), the signal format and the clock frequency (up to a maximum of 50 MHz).

The IREF pin was connected to V_{DD} through a 4.7 kΩ resistor, input pins were connected to the test machine through 1 kΩ resistors, DOUT and DS pins were connected to 2.5 V (the high–Z level) through a 500 kΩ resistor.

Several test patterns were developed, both to test the chip in **test mode** (writing the RAM via the bus) and in **data– taking mode** (writing the input pads), at 25 MHz and 50 MHz. The algorithm of a **data–taking mode** test pattern is the following:

1. CLEAR pointer (2 times, cmd+ = 1)
2. INCREMENT pointer, then WRITE into RAM (80 times, cmd+ = C)
3. CLEAR pointer (2 times, cmd+ = 1)
4. INCREMENT pointer, then WRITE into RAM (cmd+ = C)
5. READ RAM into result register (cmd+ = 8)
6. set cmd+ = 0 (NO-Operation) and addr+ = 0 (= chip ID)
7. set AS+ = 1 (38 cycles)
8. set AS+ = 0 (end of a readout sequence)
9. repeat the cycle 3–8 for another column, and so on

Later on, a full test of the RAM was performed by writing different data into columns 0–79 and reading back successfully. Also, a test of the accumulator (an additional RAM column which monitors the activity of the 64 input lines, acting like 64 1–bit scalers) was performed with success.

4.3.4 CDP mass tests

As already described for FABRICs, also CDPs have been tested before assembling. The final rad–hard version of the chip resulted to have the expected characteristics. The chips discarded were less then 10%, but many problems were find after the chips had been glued on the boards. In fact the input stages have not been tested before and they turned out to be the worst part of the chip. Almost 30% of the chips were discarded.

4.4 Test of BOARDs

The BOARDs were produced in CERN and tested before assembly in INFN Torino (after some problems were found during tests of assembled BOARDs). The 2 main problems that we found in the BOARDs themselves were the presence of short-circuits among adjacent lines or an interruption of one of these lines. In the first case it is impossible to recover the problem, in the second one sometimes it has been possible to substitute the missing line with an external one, namely soldering a wire

on the BOARD. Other problems were due to short–circuits among 2 adjacent pins of a micro flex connector or to a defective component (capacitor, filter) and this was easily recoverable.

4.5 Assembling and testing of BOARDs

The first step of the assembly is the phase of gluing detectors and chips on the boards. We use non-conductive glue for the chips and a conductive one for the detectors, to allow the electric contact to the back plane. Then the bonding phase starts: the manual bonder in INFN laboratory has been used. We also tried to use a semi-automatic one at CERN (courtesy O. Runolfsson), but the small distance between bonding pads in our chips led to some problems of short–circuits between adjacent pads. Hence those BOARDs had to be partially reworked in Torino. On each BOARD there are on average 1000 bonds: for this reason this part of the assembly job has required much time and attention.

Each bonded BOARD must be equipped with its kapton cables that allow the electrical connections. Each kapton cable, designed in Torino, produced in CERN and cut to final dimensions in Torino had to be tested to verify if there were shorts or cut lines.

The test set-up used for the tests on assembled BOARDs uses the following components:

1. an inspection microscope;
2. an IR diode (HFBR–1404 by Hewlett–Packard, wavelength $\sim$ 850 nm) with an optical fiber (50/125 μm with Amphenol 906 connector and 100/140 μm); the fiber is mounted close to the microscope objective by means of a special mechanical support.
3. a digital oscilloscope;
4. a read–out system similar to the one used in the experiment

The BUT (BOARD Under Test) is placed on a movable mechanical support identical to the one used in the experiment, and then connected by means of kapton cables to the EXTCARD. There is also a power supply unit CAEN SY527 to provide power supply to chips and detectors and a CCTD and a BUSIF to handle input and output signals. The whole system is controlled by a MacIIci Apple computer and an IBM PC. The trigger signal is simulated by a HP8082A pulse generator connected to the input of a second pulse generator whose output is used to trigger the laser diode. On the other hand, the trigger signal is sent to the CCTD that generates the clock signal and sends it to the BUSIF. To be synchronised with the time at which the laser signal gets to the detector, a delay box has been put before the BUSIF trigger input. The support on which the BUT is placed can be moved to

send the laser signal, whose spot covers over almost 6 strips in the central part of DET1 and 3 strips on DET2, on different parts of the surface of the silicon detector. The output of the detector is handled by the DAQ system and sent to the Micron -MacVEE interface (also used at CERN for the MD-SPY system). The resulting hit–maps are used to control if the BOARD presents any problem such as detector or chips having a big number of dead channels or the gain of the FABRICs not being homogeneous. If the hit–maps display some problems, a more detailed analysis of the single component performance is needed.

Usually we began by checking the state of the kapton cables. Actually this connection system, which was chosen because of its high density, turned out not to be very reliable. In fact both cables and connectors are very fragile and not suitable for a system in which one has to connect and disconnect cables very frequently. Together with cables we checked also bondings to verify if there were some wrong or missing ones.

The next step was the control of good CDP incrementation and addresses by inspecting the bus signals by means of a digital oscilloscope. These were the most serious problems that usually could be solved only by replacing the non–working chip. Of course this is a very delicate procedure because FABRIC outputs are bonded directly to CDPs inputs. Hence the non–working CDP must be disconnected from the corresponding FABRIC without destroying this one. For what concerns the FABRIC, the procedure to change one of them is much more complicated since they are connected to the glass fan–out lines and must be perfectly aligned to the fanout edge to allow bonding. The same alignment problem exists between FABRIC and CDP. Clearly, once the CDP position is fixed, few degrees of freedom remained to place the new FABRIC. For this reason BOARDs with serious problems on FABRICs were discarded, while those with CDPs problems were repaired.

After these extensive tests BOARD1s were coupled to BOARD2s and this complete module was re–tested to check if any damage occurred during the delicate coupling procedure.

4.6 Final assembly and proton beam tests

The final modules have been mounted on a stesalite mechanical support by means of precision pins and connected to the extcard with the kapton cables. After that, each extcard BUS, corresponding to 2 MD modules, one on one face of the detector and the second on the other face, has been checked with the final cables and read–out system in CERN ECN3 experimental area. As a result we discovered that the different BUSES on each BUSIF presented different timing features. For this reason we had to set a different trigger and clock delay for almost each BUSIF BUS, and we performed a series of delay scan for each BUSIF to determine the value leading to the best value for the BUSIF efficiency. The reason of this dishomogeneity has not been understood yet. Probably it is due to difference in the components of the

BUSIF, and this will be investigated before the 1998 run. After these preliminary checks MD1 and MD2 have been installed on the final mechanical support together with their extcards.

During 1996 and 1997 we had the chance to check the global performance of MD with the SpS proton beam. The tests performed can be divided into two main groups: tests with a target along the beam line, and tests with the beam impinging directly on the MD.

The first checks were done on the synchronisation of general trigger and MD system. In particular, using a tungsten target, varying the so called r_c (see section data synchronization) and looking at the hit–maps (i.e. the number of counts of some detectors), we determined the value of r_c for which the best efficiency was reached. In order to keep the synchronisation under control a TDC (Time to Digital Converter) was installed in the counting room and its output stored for off-line analysis. This output was also sent to the MD-SPY system so that we could check it during the Pb run. The results of the analysis of these data are presented in the next chapter.

Using the beam directly impinging onto the detector surface at very low intensity it is possible to carry on different studies:

- cluster size in different parts of the detector
- efficiency as a function of FABRIC thresholds (see fig. 5.7) and of HV scans
- alignment of MD1 and MD2 with respect to the beam

Some of the data of the proton beam tests must still be analysed. The results will be used to better understand the performances of our detector in 1996 run.

4.7 Pb–Pb data taking: radiation problems and possible solutions

As it was anticipated before, the environment in which NA50 takes place is comparable to the one foreseen for LHC experiments. In the 1996 Pb–Pb run the radiation fluences close to the beam axis reached the value of 10^{14} particles/cm^2, and this led to an irreversible damage of part of the Multiplicity Detector.

The main effects of radiation on silicon detectors and chips can be divided into 2 categories: surface effects and volume effects.

The surface effects are mainly due to ionizing radiations which can make permanent changes on the detectors surface. The most important effect is the creation of fixed charge zones in the oxide layer and at the interface between oxide and silicon and damages the MOS structures present on the AC detectors and the digital chips.

The volume effects are due to the interactions of heavy particles like neutrons, protons, pions with the lattice atoms. For a detailed description of the different

processes see [4]. I will resume here some features of radiation volume effects which are useful to understand what happened to the NA50 detectors. An example of the effects of radiations is plotted in fig. 4.1, where you can see the big increase of the values of the leakage current of some of the silicon detectors of MD during the 1996 Pb–Pb run.

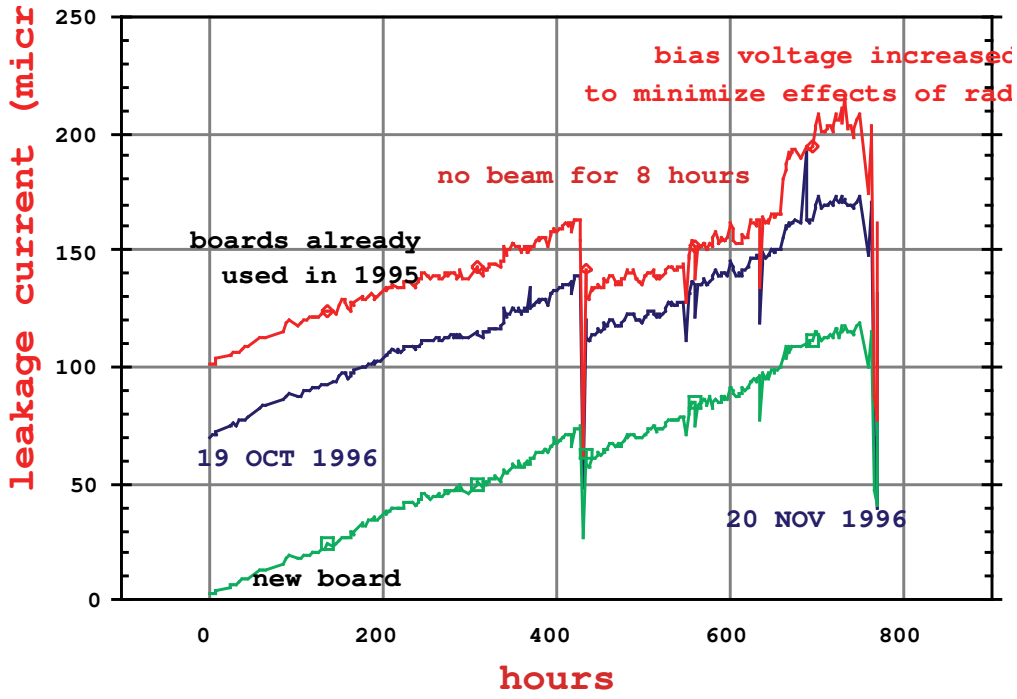

Figure 4.1: *The behaviour of detector leakage currents along the data taking period*

4.7.1 Radiation damage on detectors

The main responsible for volume damage is the non-ionizing (kinetic) energy loss which can dislocate silicon atoms from their lattice positions. The dislocated atom is called PKA (Primary Knock-on Atom) and can assume an intermediate position thus modifying the lattice structure. The empty space is called vacancy and the couple formed by one of these atoms and a vacancy is called Frenkel couple. This kind of defect is not stable at room temperature and can move inside the silicon, making stable complex with the phosphorus atoms. If the PKA has enough kinetic energy, it can dislocate other atoms and create an avalanche process which gives rise to a disordered region of the lattice called cluster.

The effect of the formation of these stable complexes and clusters is the creation of new energy levels in the forbidden gap and they can change the semiconductor characteristics in many different ways. A detailed description of these phenomena can be find in ref. [7].

There is a simple model that can explain the evolution of the defects caused by neutron irradiation on a silicon device. It has been observed that high fluence of heavy particles can vary the doping concentration in silicon detectors. It is possible that a $p^+ - n - n^+$ detector (as the ones used in NA50) can change into $p^+ - p - n^+$. This occurs for fluence values bigger than $10^{13} cm^{-2}$. In this case the junction is no more close to the surface of the detector but moves towards the back plane. This causes a loss in the efficiency of the detector because the electric field shape is varied and does not correspond anymore to the one needed to collect the charges deposited by a crossing particle in a short time. The production rate of these acceptor like impurities is constant and can be parametrized by

$$\frac{dN^V}{d\Phi} = \beta \tag{4.1}$$

where β (2.510^{-2} cm^{-1}is the probability for an hadron crossing the detector to create one acceptor like impurity per unit of path and Φ is the particle fluence. The resultant concentration of doping atoms N_{eff} is then

$$N_{eff} = N_{D,0} e^{-c\Phi} - N_{A,0} - \beta\Phi \tag{4.2}$$

where $N_{D,0}$ is the primitive donors concentration, c represents the cross section for the process of donor removal and $N_{A,0}$ is the primitive acceptors concentration. In fig. 4.2 it is clearly visible the type inversion point at $\Phi \approx 10^{13}$ hadrons/cm^2 in a detector irradiated with protons. From the macroscopic point of view, the change in the doping concentration leads to a change in the value of the depletion voltage of the silicon detector.

The dependence of N_{eff} on the depletion voltage is given by the formula

$$N_{eff} = (V_{dep} + V_{bi}) \frac{2\epsilon_0 \epsilon_r}{e d^2} \tag{4.3}$$

where V_{bi} is the built-in voltage, ϵ_0 and ϵ_r are the dielectric constants in vacuum and in the medium, e is the electron charge and d is the depleted zone thickness. Hence it is possible to extract the value of N_{eff} by measuring the depletion voltage of our detectors. In addition, the new energy levels in the forbidden gap contribute to the enhancement of the value of the leakage current according to the formula

$$\Delta I_{vol} = \alpha\Phi \tag{4.4}$$

where ΔI_{vol} is the variation of the leakage current per unit volume and α is a constant which varies according to the radiation type. In our analysis we used the α value reported in [6], $\alpha \approx 8.8 \cdot 10^{-2}$Acm^{-1}. The measurement of the leakage current can give us an estimate of the value of the fluence during the exposure to radiation. As we told before, the effects of radiations are time dependent. At the end of the exposure period, there is a first phase of annealing in which a reduction of the damages is seen, followed by a second phase of anti-annealing in which the bulk of the detector

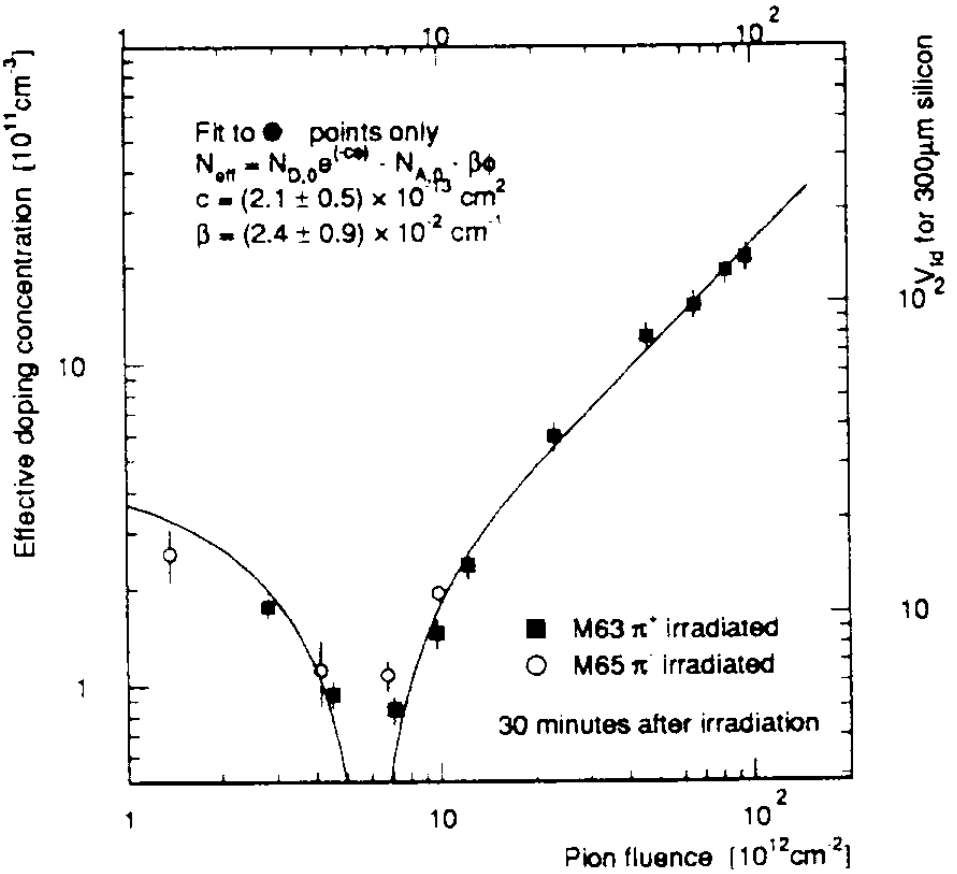

Figure 4.2: *The absolute value of effective doping cocentration calculated from depletion voltage as a function of 350 MeV/c pion fluence.*

changes rapidly to the p-type. The speed at which the anti-annealing phase takes place depends strongly on the temperature at which the irradiated devices are kept. It has been demonstrated experimentally that the anti-annealing process can be partially stopped by keeping the irradiated devices at low temperature.

The progressive damaging of the MD has been observed already during the 1996 Pb–Pb data taking period. In fact the on-line monitoring of leakage current and hit maps showed that the efficiency of innermost strips was decreasing. It could be in part recovered by increasing the polarization voltage, but unfortunately the value of the leakage current was too high and started to cause problems also for the front–end chips.

Actually in the DC coupled detectors of the outer crown (DET2), the leakage current flows inside the input stage of the FABRIC preamplifier. This fact leads to a variation of the working conditions of the chip and in particular to a decrease of the gain and an increase of the noise. The solution could be the raising of the

threshold value of the discriminator, but unluckily the threshold value is common to both types of detector, and increasing its value too much could lead to a loss of efficiency in DET1s.

For the 1998 run we have foreseen a change in the power supply lines to supply different threshold values to BOARD1 and BOARD2. At the end of the data taking period all the components of MD have been dismounted and taken back to INFN laboratories in Torino, where they are kept in a fridge to stop reverse-annealing process. Immediately after the end of the exposure period some detectors have been extensively tested to evaluate the global effects of radiations on them. Fluence values and inversion have been investigated using three different experimental methods:

- Leakage current measurement
- Voltage depletion measurement
- High voltage scans.

For what concerns the current measurements, they have been performed using the same experimental set–up used for the detectors tests. The measurement is different in case of DET1 and of DET2. Since the DET1 strips are all connected to the same bias line it is not possible to measure the value of the leakage current strip by strip but only to measure the total current.

With this measurement it has been possible to see the increase of the current value with the increase of the duration of the exposure to radiation and the reverse annealing effect. Three BOARD1s have been chosen among the MD modules: one was used only in 1996 and always kept in the fridge after exposure, the second one was used both in 1995 and 1996 and had been kept at room temperature for one year. The third one was used also in 1994. The results show that the last two present a very high value of leakage current compared to the one used only in 1996. This confirms both the effect of radiation and of reverse annealing.

On DET2s, however, it has been possible to verify the behaviour of leakage current on different strips. The shape of the I-V curves shows the point at which the detector is completely depleted. Starting from the most internal strips and going towards the external ones the value of V_{dep} grows.

The second kind of performed measurement is the Capacitance versus Voltage curve (C-V), deducing from it the value of V_{dep}. In this case it has been possible to measure the C-V characteristic strip by strip also on DET1. The result show a complete different behaviour among the two devices. In fact the C-V curves confirm the result found with I-V measurements on DET2: going from inner to outer radius the value of V_{dep} grows. On the opposite, on DET1 V_{dep} grows going closer to the beam axis. This confirms the hypothesis that type inversion occurred on DET1s.

To evaluate the point at which this happens, i.e. the strip that has V_{dep}=0, another method has been used. During the last hours of beam time of the 1996 run we performed some High Voltage (HV) scans, starting with a 0V bias value and

going up to the maximum value allowed by the CAEN SY527 i.e. 200 V. Analysing the hit maps of the detectors it is possible to see at which level of bias the bulk under each strip is fully depleted. The results of this analysis confirm the previous ones. Starting from the value for $I_{leakage}$ and V_{dep} measured with these 3 methods we can estimate the value of fluence and dose taken by the MD. The fluence is determined using the formula 4.2, in which we used the values of α, β, c found in [6]. For the DET2, starting from the value of $I_{leakage}$ measured before and taking into account some corrections for the self-annealing process, we obtain a fluence of 3×10^{12} hadrons/cm^2 for a radius of 3-4 cm and 1×10^{12} hadrons/cm^2 for a radius of 8 cm. This result is confirmed if we use the HV scans data. In addition using this method we get also an estimate of the fluence on DET1s: it varies from 1×10^{13} hadrons/cm^2 at the outer radius to 1×10^{14} hadrons/cm^2 for the innermost strips. If we want to give an estimate of the value of dose starting from the fluence we must take into account the fact that the total fluence is made not only by hadrons but also by electrons and photons. On average we will assume

$$\Phi_{tot} \approx 2 \cdot \Phi_{had} \tag{4.5}$$

The resulting dose received by MD on the innermost strips turned out to be close to 3M rad (or 3×10^4Gray). Summarising the results obtained by these post–exposure measurements:

- The DET1 resulted to be type-inverted
- The Type inversion point could not be determined very precisely but it seems to be on the most external strips of DET1.
- The BOARDs used also in 1995 are so damaged that will not be used in 1998 run and must be substituted.
- The leakage current increases strongly with the increase or the duration of exposure period and with reverse annealing
- The estimated values for fluence and dose are close to the ones determined by simulations

For more details on these studies see [4].

4.7.2 Radiation damage on digital chips

In this section I will briefly describe the effects of ionizing radiation on MOS (Metal Oxide Semiconductor) devices, since our digital chips are made with CMOS tecniques. These effects can be divided in TDE, Total Dose Effect and SEE, Single Event Effects. The damages caused by first category consist in a permanent modification of the characteristics of the oxide layer, the second one can cause temporary or permanent malfunctions and also a sudden loss of data in the memory. For what

concerns the problems occurred to our detector, they are mainly due to SEE. Hence I will not describe the TDE, a good report can be found in [7].

We talk about SEE when a single particle loses a big amount of energy in the device, in a very short time. In fact this process becomes dangerous for a MOS device when the rate at which the dose is deposited is close to 10^6, 10^7 rads/sec. The amount of energy loss by a ionizing particle inside a medium is measured in terms of LET (Linear Energy Transfer) in units of eV $\times$ mg$^{-1}\times$ cm^{-2}. Along the trajectory of the ionizing particle a cylindric shaped region is created. Inside this region the charge density decreases going towards the outside as r^{-2}. Hence the particle trajectory can be seen as a conductive wire connecting two points of our device. Of course usually this perturbation is not enough important to modify substantially the shape of the potential in the device. However sometimes this happens, and the hole-electron couples created by the ionizing particle are separated by the electric field present in the MOS structure and become parassitic currents whose intensity is proportional to the dose deposited by the incident particle. If the dose is very high, the value of this currents can be bigger than the ones characterizing the circuit, and modify the working parameters of the circuit itself. There are three main effects due to this process:

- Single Event Upset (SEU): it can modify the data in some memories, but usually has only temporary effects that do not damage permanently the circuit
- Single Event Latch–up (SEL):it is maybe the most interesting effect observed during 1996 run on MD CDPs. It corresponds to the activation of parassitic transistors which put the circuit in a stable state, but with very high values of the current. The only way to make the circuit work again is to switch off and on again the power supply of the chip.
- Single Event Burn–out (SEB): this occurs when the deposited dose and the corrisponding parassitic current is so high that metal lines and junctions are destroyed.

We already told that the SEL, also called simply latch–up, is a very interesting phenomenum. In fact a lot of studies have been carried on for the development of rad-hard circuits to be used in LHC experiments, and one of the problems to be analyzed is the latch–up.

During the 1996 run we observed that 7 CDPs (out of 216) presented a strange behaviour: sometimes they simply stopped to respond properly, and the current on the power supply line suddenly increased. This conditions stayed the same until the power supply was switched off and on again. At the end of the run the BOARDs on which these chips were mounted have been carefully tested to verify if the cause of this phenomena was really latch–up. In particular we checked if the CDPs on which the latch–up had been observed were rad-hard Honeywell chips or non rad-hard prototypes by HPMOSIS. It turned out that 5 were HPMOSIS, the other 2 HONEYWELL. In addition, these two were mounted on the same BOARD together

with 2 HPMOSIS chips. Since there were only 5 non rad–hard chips on the whole detector we can conclude that the special technology used by HONEYWELL is really rad-hard. In fact only 1% of HONEYWELL chips were affected by latch-ups, and we must remember that these 2 were placed close to 2 HPMOSIS chips that, being almost permanently in latch-up state, heated the region around them. High temperature can influence the performance of a chip increasing the currents and thus preparing good conditions for a SEL to occur. For what concerns the HPMOSIS prototypes, 100% of them were in permanent latch–up conditions at the end of the run, also because they had been used already in 1994 and 1995 runs. The latch–up study is described in an exhaustive way in [5].

Bibliography

[1] W. Dabrowski and J. DeWitt, Nucl. Instr. and Meth. A326 (1993), 82

[2] A.Dondo, Thesis, Torino University, 1995.

[3] R.Crovato, Thesis, Torino University, 1994.

[4] E.Crescio, Thesis, Torino University, 1997.

[5] F.Prino, Thesis, Torino University, 1997.

[6] S.J.Bates et al., Damage induced by pions in silicon detectors, CERN-ECP/95-03.

[7] S.J.Bates, PhD Thesis, Canbridge University, 1993.

[8] Testing Digital ASIC's (FDB64), COREP–LETEO, Release 1.0, April 30, 1993.

[9] Test of Digital ASIC's (FDB64), COREP–LETEO, Release 3.0, November 5, 1993.

Chapter 5

The MD data analysis

The primary goal of the multiplicity detector is the measurement of the number of charged particles produced in the interaction (N_{ch}) in different pseudorapidity regions, numbers that can be used to determine the centrality of the interaction. The charged multiplicity variables together with E_t and E_{ZDC} constitute the so–called "global variables".

The second aim of MD is the recognition of the subtarget in which the interaction took place. The 2 planes of silicon detector can in fact be used as a tracking tool to determine the interaction vertex. This is an alternative tool to the standard quartz blades sub–target determination system, which loses efficiency for peripheral events.

Before producing final results we had to evaluate the performance of our detector. Unfortunately the high dose of radiation deposited on the MD during the 1996 data taking period caused a progressive degradation of efficiency. Hence we must evaluate this efficiency along the whole period and correct the raw multiplicity on a run by run basis.

Another problem to be taken into account is the non perfect alignment on the beam axis of the centre of MD. This affects the choice of the strips to be used for the evaluation of multiplicity in different intervals of pseudorapidity.

In the following sections I will explain the different steps carried on to obtain a correct value of the multiplicity global variables.

5.1 Definition of MD global variables

The charged multiplicity has been evaluated in different intervals of pseudorapidity. The first one, originally foreseen as $2.7 \leq \eta \leq 3.9$ (changed to 2.5–3.5 because of the detector offset), corresponds to the spectrometer acceptance and the associated multiplicity variable is called MDMUL1. MDMUL2 corresponds to the number of charged particles on MD1 (BOARD1s only) and so the pseudorapidity interval varies according to the sub–target in which the interaction took place. MDMUL3 is the multiplicity corresponding to backward pseudorapidity (1.65–2.5). In fig.5.1 there is a simple sketch of the choice of the range of strips on each MD plane used to

evaluate MDMUL1. This range of strips is not exactly the same for each sector

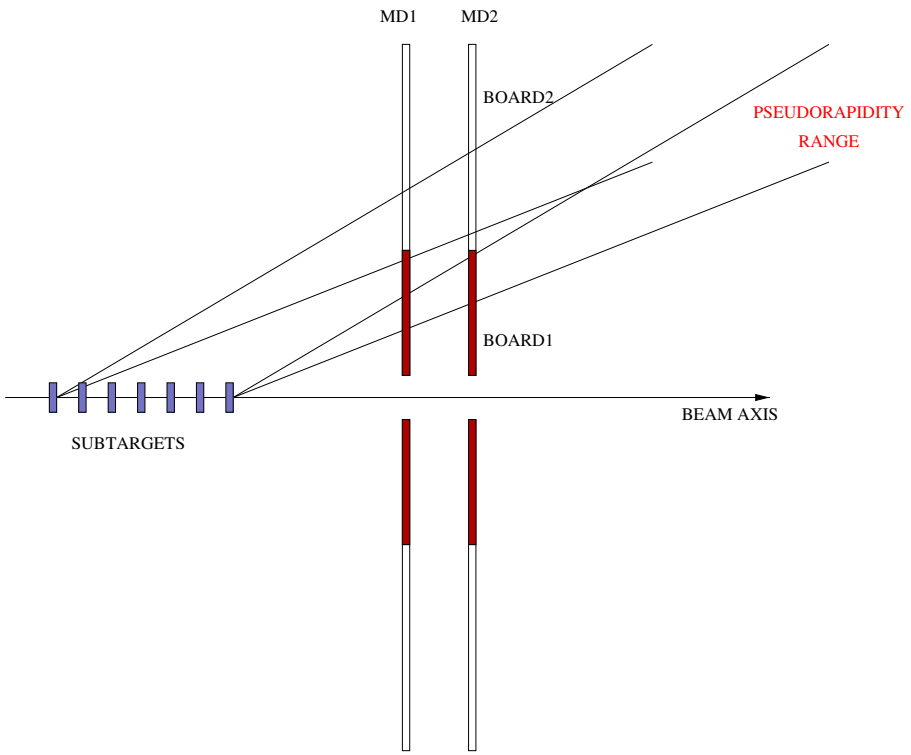

Figure 5.1: *Sketch of the possible choice of strips to be used for different pseudorapidity ranges on MD1 and MD2*

because of the misalignment of the MD with respect to the beam axis.

5.2 The evaluation of multiplicity

To get the correct number of charged particles in the desired range of pseudorapidity it is necessary to correct the **raw multiplicity** N_{ch} (i.e. number of hits) according to the estimated value of efficiency.

The efficiency ϵ depends on the different components of the detector:

- the silicon detector itself
- the analog chip (FABRIC)
- the digital chip (CDP)

In addition to the correction for efficiency it is necessary to take into account also the non–responding and the noisy channels. A detailed study has been carried out to define criteria to identify dead strips, and to fix a threshold to separate noisy channels. It is described in the next section.

The last correction to be applied is the one for the multiple occupancy of strip, determined by simulations based on the Poisson distribution.

All these corrections are computed and applied to groups of strips rather than to the whole detector, to take into account variations within the detector.

Then the correct **multiplicity per sector** is formed using good sectors and the obtained value is the global variable. The choice of good sectors is made by fixing a threshold for ϵ and discarding the ones with ϵ below this threshold. Moreover we exclude the sectors in which there are many groups of dead strips. At the and of all these correction procedures we obtain 3 values for the multiplicity (MDMUL1-2-3) that can be used as centrality estimators. In the following sections I will explain how we computed the different correction factors.

5.3 Definition of dead and noisy strips

The first correction applied to the raw multiplicity is the definition of non–working and noisy strips. A non–working or dead channel is a strip with a very low (even 0) occupancy as compared to nearby strips. The main reasons for this to happen are:

- a broken bonding
- charge collection inefficiency in the detector
- malfunctioning FABRIC channel
- malfunctioning CDP channel (usually the whole input stage, see previuos chapter).

A noisy channel is a strip for which the occupancy is always close to 100% or that has a number of counts much greater than the others. We must get rid of these malfunctioning channels because their presence in the computation of N_{ch} could lead to an over/under estimation of the multiplicity itself.

It is also very important for the target recognition algorithm, because, to use the detector as a tracking system, we must know very precisely the position of bad channels to avoid fake tracks. To recognize dead and noisy strips an algorithm that analyses the hit–maps (i.e. maps of hits on each DET1 and DET2, see fig. 5.9) of the 72 sectors of MD1 and MD2 was used. The logic scheme of the algorithm is the following:

- grouping of the 192 strips of each sector in 6 groups of 32 strips.
- computation of the average value of multiplicity $\bar{M}$ for each group.
- exclusion of sectors for which the number of recorded events is less than 25% of the total number of events.
- exclusion of noisy channels: a channel is noisy if

  - the occupancy is higher than 72%
  - the number of counts is higher then $4 \cdot \bar{M}$

- new computation of $\bar{M}$ (after noisy strips exclusion)
- search for dead channels. A channel is dead if
  - the occupancy is less than 0.5%
  - the number of counts is less than $35\% \cdot \bar{M}$

The choice of these value has been done analyzing the results obtained varying the value of the threshold. As an example the plot 'number of dead channels versus threshold value' is shown in fig.5.2. It is clear that the threshold value of 35% is

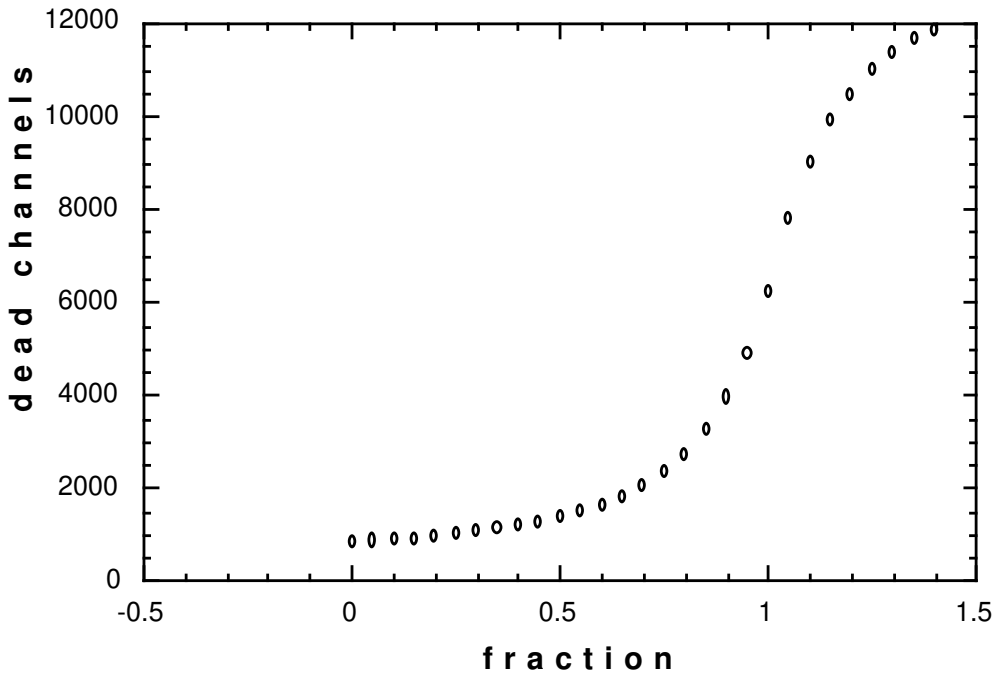

Figure 5.2: *Number of dead channels versus threshold value*

below the zone in which, together with effectively dead strips, we start to exclude also a big number of good strips.

The analysis has been performed on almost 70 runs distributed along the data taking period. This allows us to verify the performance of our detector, since the strips becoming inefficient at a certain point will be considered dead, and hence the number of dead strips should be increased. On the opposite, the number of noisy channels is decreased when the gain of the FABRIC pre–amplifier decreases. As

explained in the previous chapter, the progressive increase of the leakage currents (see fig.4.1) due to radiation damage, changes the working point of the amplifier. In fig.5.3 and fig.5.4 the behaviour of the dead and the noisy strips values during the run is shown.

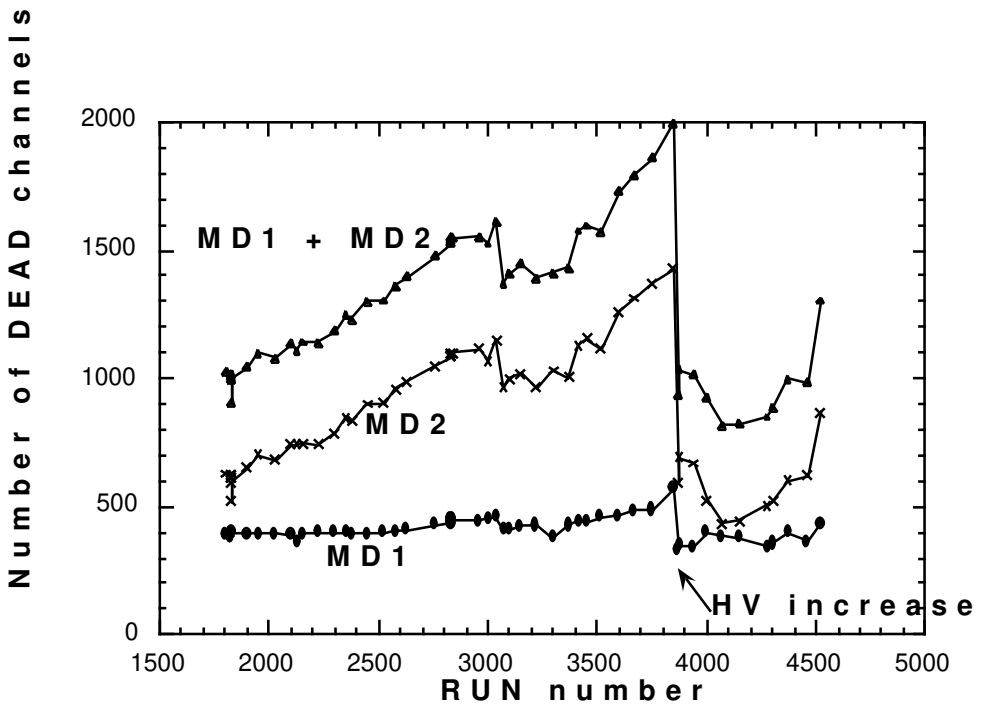

Figure 5.3: *Number of dead strips vs run number*

5.4 Definition of MD efficiency ϵ

The MD efficiency ϵ can be defined as the product of 3 factors: ϵ_{DET}, which is the efficiency of the silicon detectors, ϵ_{FABRIC} the efficiency of the analog chips on the BOARD2s and then ϵ_{CDP}, the efficiency of the digital chips.

5.4.1 Silicon detectors efficiency

The efficiency of the silicon detectors is strictly dependent on the concentration of doping impurities in the silicon bulk.

As explained before, the enhancement of the number of acceptor–like impurities leads to a condition of type-inversion of the detector bulk. The effect of this, is that the V_{dep} increases and there are zones of the detector in which the bulk is not completely depleted at the standard values of bias voltage. The depletion voltage

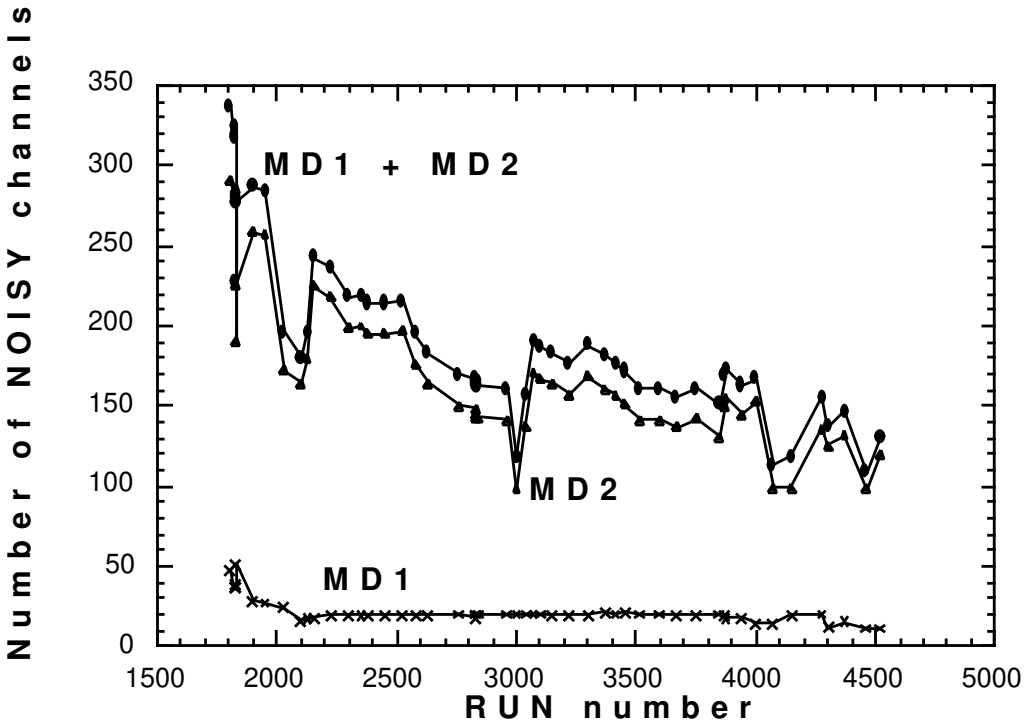

Figure 5.4: *Number of noisy channels vs run number*

after type-inversion is roughly proportional to the fluence, hence it is more evident for the innermost strips, and only for the DET1. The fact that the bulk is not empty of free charges makes easy the recombination of the electron-hole couples created by the passage of a ionizing particle. It is clear now that this was the main reason for the process of efficiency loss of the MD during the data taking period. The initial efficiency value could be restored (not completely) increasing the HV. However the limits of the CAEN A520 power supply module (V_{max}=200V) and the continuous increase of the leakage current prevented us to keep a good level of efficiency till the end of the run.

In order to better understand the type–inversion phenomenon, at the end of the data taking an HV scan study was performed: the bias voltage of the detectors was increased starting from 0 V up to 200 V, and then we analyzed the hit–maps obtained for different values of the bias voltage. From these data (see fig.5.5) it is possible to evaluate the occupancy value for different strips of the same detector. Starting from the innermost strips (5-65) we can see that the occupancy value is very low for low values of HV and then it grows increasing the voltage. It is clear that for the detectors irradiated in 1995 and 1996 the innermost strips are never depleted. For this reason these detectors will not be used anymore; they will be replaced by new ones for the 1998 run. The detectors irradiated only in 1996 can be fully depleted with a relatively low value of HV, almost 120 V. Hence they will be used again in 1998 run. Another way to see which is the depletion value for each

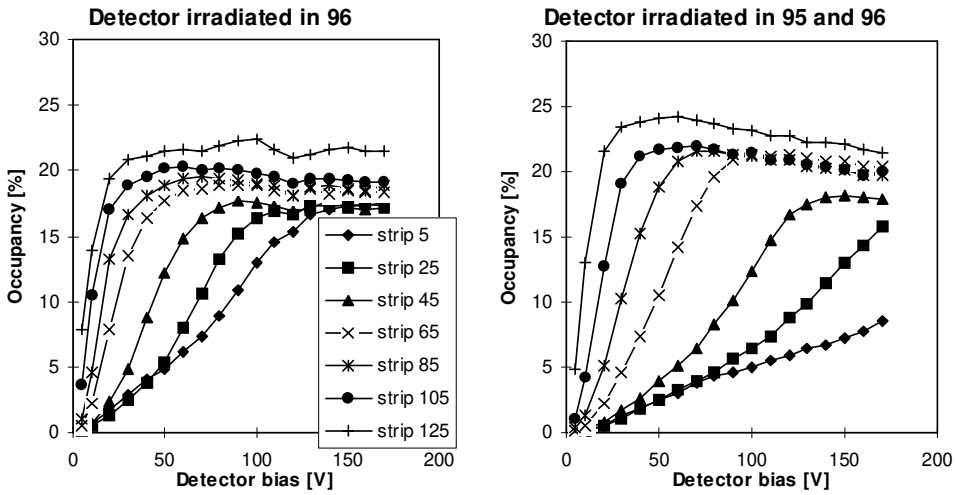

Figure 5.5: *Detector bias voltage scans on 2 detectors: occupancy vs bias for different strips, from internal ones (5-65) to outermost ones (85-125)*

strip is shown in fig.5.6: for the first 3 groups of strips, in case of detectors irradiated in 2 years, the depletion voltage is higher then 160 V.

5.4.2 Analog chips efficiency

The direct evaluation of the FABRIC efficiency in Pb run data is not easy. In fact the data we have shown about the efficiency variation of the detectors were due not only to DETs, but also to FABRICs and CDPs. The only possibility we have to understand the FABRIC efficiency is to study the data taken with proton beam impinging on some BOARDs of MD1 and MD2.

These scans have been done varying the differential threshold of the FABRIC discriminator. Plotting the number of counts on a given group of strips versus the threshold, we can see, as shown in fig5.7, the deacrease of counts corresponding to the increase of the threshold. If we plot the differential curve of the counts we can get rid of noise and see easily the Landau curve of the beam energy deposition in the detector bulk. Now, assuming to be in the same detector and CDP conditions as in the Pb run, we can see at which point of the Landau peak we fixed the threshold in 1996 Pb run, and thus we can understand the value we got for ϵ_{FAB}. As a first approximation we decided to fix ϵ_{FAB} to 1, except for the cases in which a big difference of gain was seen at hit–maps level, and for the BOARD2s for which there was a detector current induced gain change (due to DC coupling).

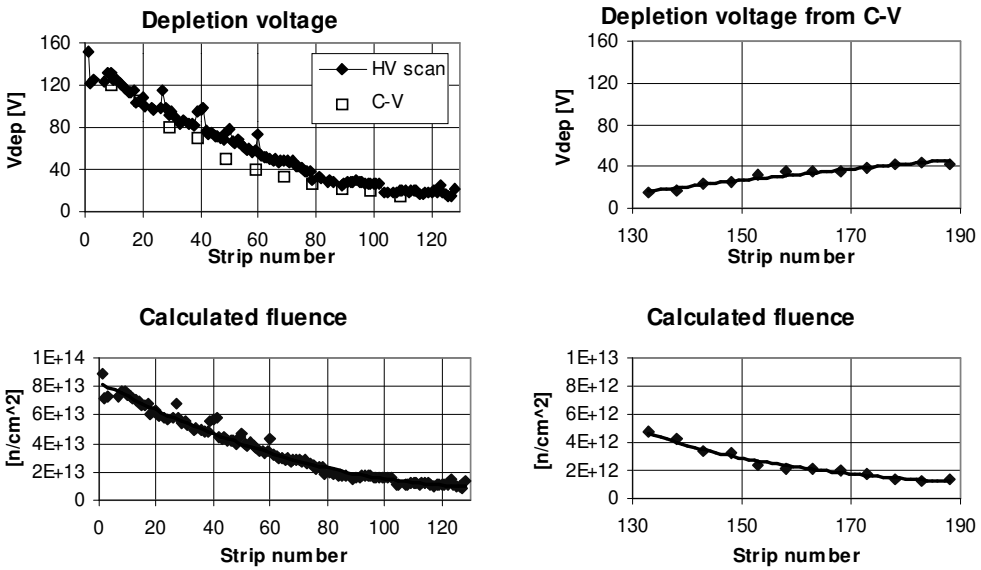

Figure 5.6: *Detector bias voltage scans: depletion voltage vs strip number for different detectors*

5.4.3 Digital chips efficiency

The efficiency of CDPs (apart from individual bad channels) is determined by the synchronization of MD read–out system with the general trigger signal. The different steps needed to synchronize the MD trigger with the general trigger are described in sect.3.9. To control the synchronization a TDC module was installed, to measure the time difference between the MD trigger and the general one. Unfortunately the

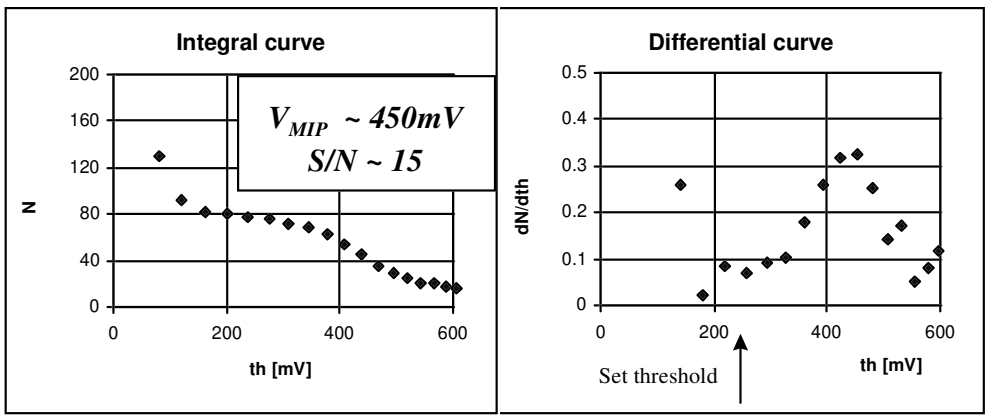

Figure 5.7: *Number of counts for a given group of strips versus threshold value: intergral and differential curves*

Timing–Unit used to compensate for the length of cables was not very stable and the center of the TDC distribution does not corrispond always to the same channel. This must be taken into account before applying any timing efficiency correction to our data.

The synchronization must be analyzed event by event and CDP by CDP, since unfortunately the digital components of the read–out chain are slighly different and cause systematic errors in the synchronization of the 216 CDPs.

To evaluate the right trigger delay for each CDP, a series of 3 trigger delay scans has been performed. This means that we measured the mean multiplicity for each CDP as a function of different values of the trigger delay.

The result of this scan for CDP 1 is plotted in fig.5.8: a plateau in the multiplicity distribution is visible in correspondence of the correct delay for this chip.

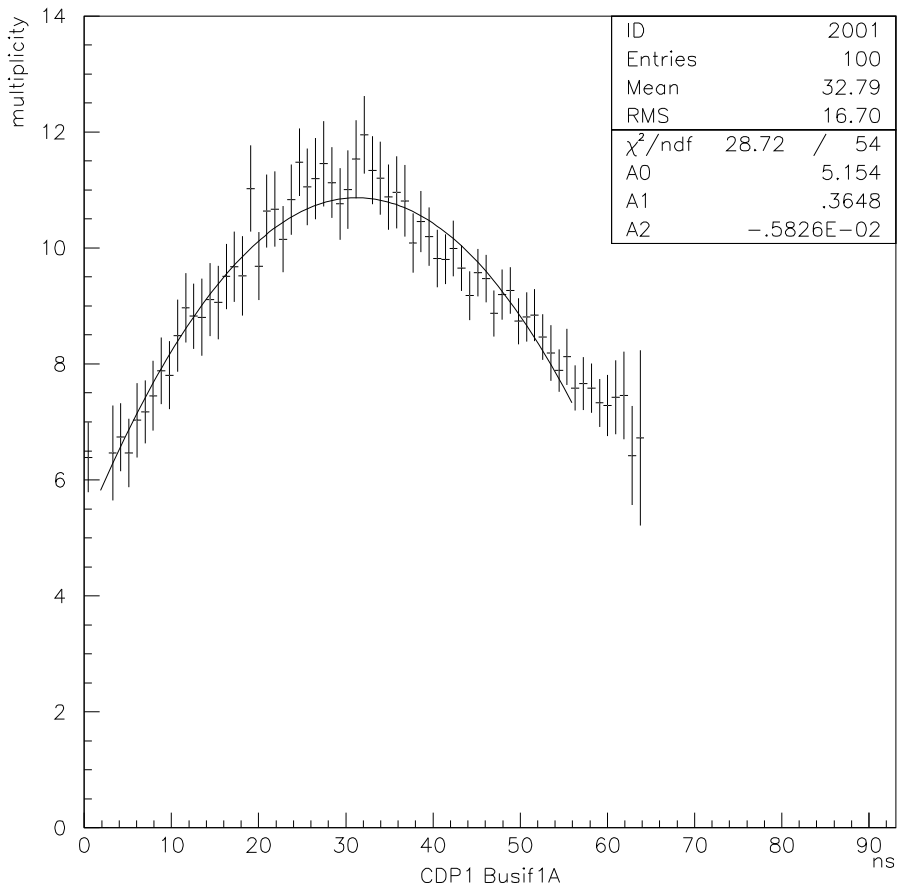

Figure 5.8: *Distribution of multiplicity vs trigger delay for CDP1*

Since the delay value is common to all the CDPs of each BUSIF(BUS), it is not possible to fix the optimal trigger delay for each CDP. In other words, one of the CDPs of a board could be in a region different from the plateau, that is we are not

always reading the right column (the one corresponding to the event that triggered the apparatus). We want then to correct for this inefficiency using the results of the delay scans as a reference. As a first step we fit the multiplicity distributions versus delay with a parabola and insert the parameters of the fit in the correction algorithm. The formula used for the fit for each CDP is the following

$$\epsilon^i_{TDC} = \frac{y^i_{max} + c^i(X - x^i_{max})^2}{y^i_{max}} \tag{5.1}$$

where X is the TDC value (including the Δx correction due to the timing unit), y is the multiplicity, c is the negative curvature of the parabola and i is the CDP index (1-216). Then, event by event, the program uses the x^i_{max} of a given CDP, inserts the common value of the TDC in the above formula, and extracts the corrisponding ϵ_{TDC}.

5.5 Efficiency corrections

As explained above, we correct our data for efficiency losses in the following way:

$$M = N_{ch}\epsilon \tag{5.2}$$

where ϵ is obtained by

$$\epsilon = \epsilon_{DET} \times \epsilon_{FAB} \times \epsilon_{CDP} \tag{5.3}$$

We started by applying this method but the problems found trying to distinguish the two first terms of the above formula lead us to a different approach. It is a rather empiric method, based on the assumption that the new BOARDs must have efficiency equal to 1 at the beginning of the 1996 Pb run. In addition, if the MD is perfectly aligned on the beam axis, also the shape of the hit–maps should be the same for different sectors. Hence we chose a reference sector (no.4 for MD1, no.13 for MD2) to which we compared the shapes of the other sectors. Of course, since the detector is not aligned on the beam axis, the comparison must not be done on the occupancy versus strip number but on N, defined as $N = N_{hits}/event \cdot cm^2$, versus R, where R is the radial distance (measured in cm) from the beam. In fig.5.9 the difference between a sector corresponding to a new BOARD and one corresponding to an old one is shown.

A polinomial fit is done on the $N(R)$ distributions for the reference sectors. Then the $N(R)$ distribution for the other sectors are compared to the function obtained from the fit, and, in the hypothesis that the new BOARDs have efficiency ϵ_{new} equal to one, from the comparison we obtain the efficiency of the old BOARDs ϵ_{old}. This equalization procedure is done making an average on the data in the first 5 runs (1805-1810).

The next step is the evaluation of the efficiency variation along the data taking period. For a given run we must compute the so–called **relative efficiency** ϵ_{rel},

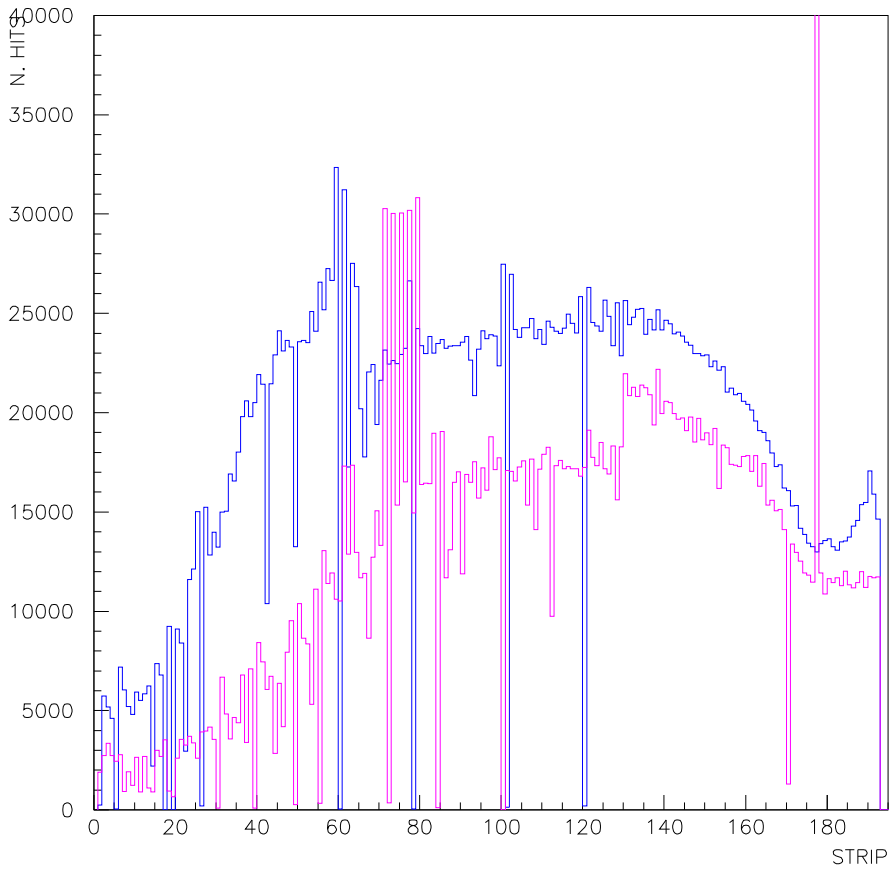

Figure 5.9: *Hit-maps of two different efficiency sectors*

defined as the ratio between the number of counts per number of events for a given strip in a given run, and the correspondent frequency of counts measured in the reference runs (1805-1810). The number of hits of a strip is determined fitting the hit–map of the sector with a polinomial function (as already done for the initial equalization procedure).

Since the number of hits on one strip is affected by statistical fluctuations, it was decided to make an average over 16 strips: each MD sector was then divided into 12 groups of 16 strips each. The dead and noisy strips are excluded from the average. The **mean relative efficiency** $\bar{\epsilon}_{rel}$ is then defined by the following formula:

$$\bar{\epsilon}^{s}_{rel,gr} = \frac{1}{K} \sum_{i=imin}^{imax} \epsilon^{s}_{rel,i} \tag{5.4}$$

where:

- s: sector index (s=1,36)
- gr: group index (gr=1,12)

- i: strip index
- K: number of good strips
- imin = (gr-1)*16+K
- imax = imin + 15

To compute the **absolute efficiency** ϵ_{abs} for a given run we use the following formula:

$$\epsilon_{abs}(run(n)) = \frac{\epsilon_{rel}(run(n))\epsilon_{det}(4460)\epsilon_{CDP}(4460)\epsilon_{FAB}(1805)}{\epsilon_{rel}\left(\frac{4460}{1850}\right)} \tag{5.5}$$

where 4460 is the run in which the delay scans and the HV scans were used to determine ϵ_{CDP} and ϵ_{det}, 1805 indicates the group of initial reference runs. The ϵ_{FAB} was assumed to be equal to 1 also beacause it is almost impossible to separate its contribute from the detector one. In addition the definition of the denominator is given by:

$$\epsilon_{rel}\left(\frac{4460}{1850}\right) = \frac{\epsilon_{det}(4460)\epsilon_{CDP}(4460)}{\epsilon_{det}(1805)\epsilon_{CDP}(1805)} \tag{5.6}$$

The values of the different efficiency are stored in data files used by the analysis algorithm to compute ϵ_{abs} on a run by run basis.

5.6 The MD target identification algorithm

The MD target identification algorithm is based on the reconstruction of tracks pointing to the subtargets made by putting in coincidence strips of the 2 planes of MD. We start by looking for a "firing" strip on MD1. In the hypothesis that the interaction took place in subtarget number N (N=1, ..7), we draw a straight line between this subtarget and the firing strip on MD1. Then we extend this line to MD2. If the intersection point belongs to a sensitive region we look at the strip corresponding to this point and the 2 adjacent ones, as is shown in fig.5.10. We fix a threshold ($\approx 30\%$) on the efficiency of MD2, and, if the efficiency of a strip which is "candidate" for a coincidence with MD1 is higher than the threshold, a counter called POSCOI(N) is incremented by 1/3 (by one if the three strips are above threshold). Then we see if these strips are firing: if this happens, another counter, called TROCOI(N), is incremented. We increment TROCOI 3 times if all the 3 strips are firing. This triple incrementation is useful because it is an indirect method to take into account the very low mean efficiency of MD2. Then we create a target estimator called TARTES(N), according to the formula:

$$\text{TARTES} = \frac{\text{TROCOI}}{\text{POSCOI}} \tag{5.7}$$

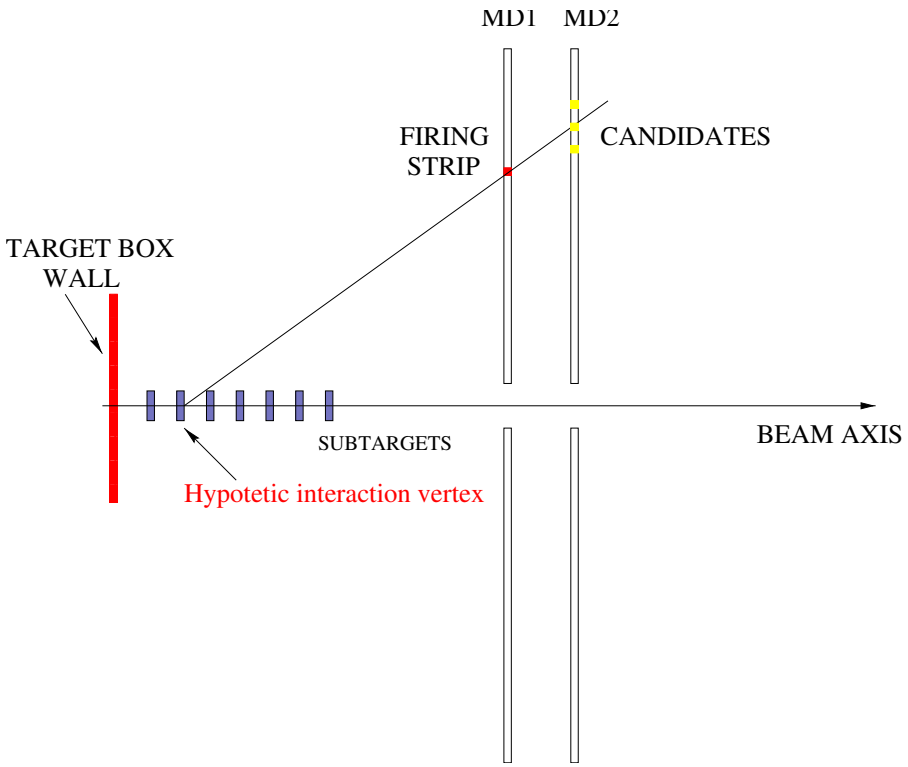

Figure 5.10: *Schematic drawing of the MD target identification algorithm geometry*

We repeat this process for 7 positions corresponding to the 7 subtargets, plus other two positions corresponding (1) to the wall of the target box, an aluminum layer in which some interactions take place (upstream interactions), and (2) to a very upstream interaction. For a given event, the position for which TARTES has the highest value is the one corresponding to the interaction vertex. To detect the non interacting ions we fix a threshold value for TARTES. If TARTES does not reach the threshold we say that the ion did not interact. The results are used to define a new variable used during the data analysis to determine the interaction vertex. This variable is called NOCIMD (Number of subtarget determined by MD) and can assume 9 values: 0 corresponds to upstream interactions, 8 corresponds to non interacting ions and 1-7 is the number of the identified subtarget. In fig.5.11 two distributions of the target estimator highest value (among the 9) are plotted: in the top part no selection on the target value has been done. This means that also the non-interacting ions are included. In fact a peak at very low values is visible, but it vanishes if we select events in which the target has been identified, and this is clear in the second distribution in fig.5.11.

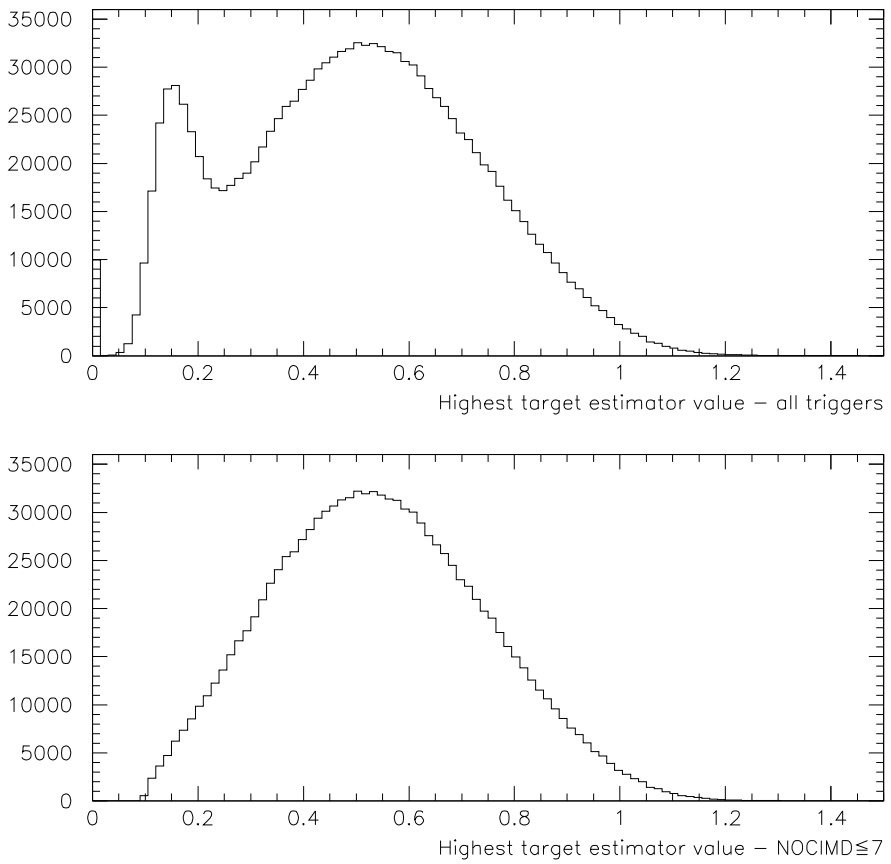

Figure 5.11: *Distributions of the target estimator highest value*

5.6.1 Corrections for radiation damage

As written above, the innermost strips were heavily damaged during the run and their efficiency become lower. The consequence of this affects the target identification algorithm in the sense that, given a certain threshold on the MD efficiency, the innermost strips on MD1 will not be recognized as "firing". This leads to the artificial increase of the number of upstream interactions (NOCIMD=0). To avoid this error we compute the average value of TARTES in the subtargets and, if the value of TARTES for upstream interactions is slightly higher then this average, we do not count this as an upstrean interaction but we decide that the interaction took place in the subtarget fot which TARTES reaches the maximum. To test this procedure we make a comparison between NOCIMD and NOCIBI (the subtarget identification variable obtained using the active target quartz blades system) in central collisions, for which NOCIBI has a good efficiency. This test confirmed the validity of our assumptions and in this simple way we were able to correct our identification method for the effects due to radiation damage.

Chapter 6

The MD as a centrality detector: data analysis and results

6.1 Raw Data treatment and event selection

During the data taking period the raw data are stored on tapes called RDT (Raw Data Tapes), according to a structure containing three hierarchical levels: run, bursts and events. These data undergo a long process of reduction, in which the experiment reconstruction program, called DIMUREC, extracts higher level information: the kinematical variables of the muons, the interaction vertex, the transverse neutral energy in the electromagnetic calorimeter, the forward energy in the zero degree calorimeter, the charged multiplicity in different η intervals measured by the multiplicity detector, and some control variables used for later analysis.

Using the reconstructed quantities different selections are applied:

1. selection on the global quality of the run (stable beam intensity, good beam alignment, good number of reconstructed J/ψ's per unit of incident beam);

2. event by event selection requiring a single interaction in a subtarget, no pile–up in the BH, no pile–up in the ZDC, no beam halo;

3. event by event selection on muon kinematical quantities.

This last selection is the most important one from the physics point of view, and is made using the informations coming from the muon spectrometer. The selected events must have two tracks reconstructed in the MWPCs (they must point to the target region) with the the corresponding hodoscope slabs fired and satisfying offline the trigger requirements. Events in which one muon (or both) had azimuthal angles corresponding to the iron pieces of the magnet, or had trajectories going outside of the fiducial region where the chambers and hodoscopes have $\approx 100\%$ efficiency, are rejected (these cuts are called fiducial cuts). Another kinematical cut, called image cut, is then applied: it rejects events in which changing the charge sign of either

muon, the resulting trajectory goes out of the spectrometer fiducial region. The image cut is very important for the treatment of combinatorial background, since it ensures that the acceptance for convergent and divergent tracks is the same.

The DIMUREC program determines the position of the interaction vertex using the pulse height information from the active target quartz blades. The knowledge of the vertex position is very important in the evaluation of the dimuon mass because the correction for multiple scattering in the absorber is based on it. The experimental resolution in invariant mass gets a contribution from the error on the vertex position, which increases in the case of peripheral events, for which the target recognition is not reliable (when the target recognition by quartz blades fails completely, the central subtarget is assumed).

For each of the selected events, a restricted set of variables are written to the final analysis data files (the so called micro Data Summary Tape or μDST). When reading back a μDST, some additional cuts on the dimuon kinematical variables can be applied, namely on invariant mass, rapidity, transverse momentum and polar and azimuthal angles in the Collins–Soper reference frame Θ_{CS} and Φ_{CS}. In this analysis the high mass ($\geq 2GeV/c^2$) region has been chosen, together with a dimuon kinematical window defined by $3 \leq y_{lab} \leq 4$ and $-0.5 \leq cos(\Theta_{CS}) \leq 0.5$. In fact out of this region the value of the acceptance is very low.

6.2 Event selection in centrality bins

In Pb-Pb (or other ion–ion) studies it is possible to determine the event centrality by means of dedicated detectors, which in the NA50 apparatus are the electromagnetic calorimeter, the zero degree calorimeter and the multiplicity detector.

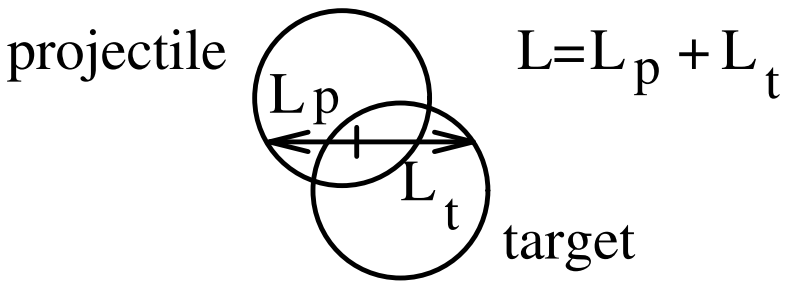

Figure 6.1: *Schematic drawing of the L variable*

The value of each one of the centrality variables can be related to the impact parameter b, as explained in the following. By selecting specific intervals of a global

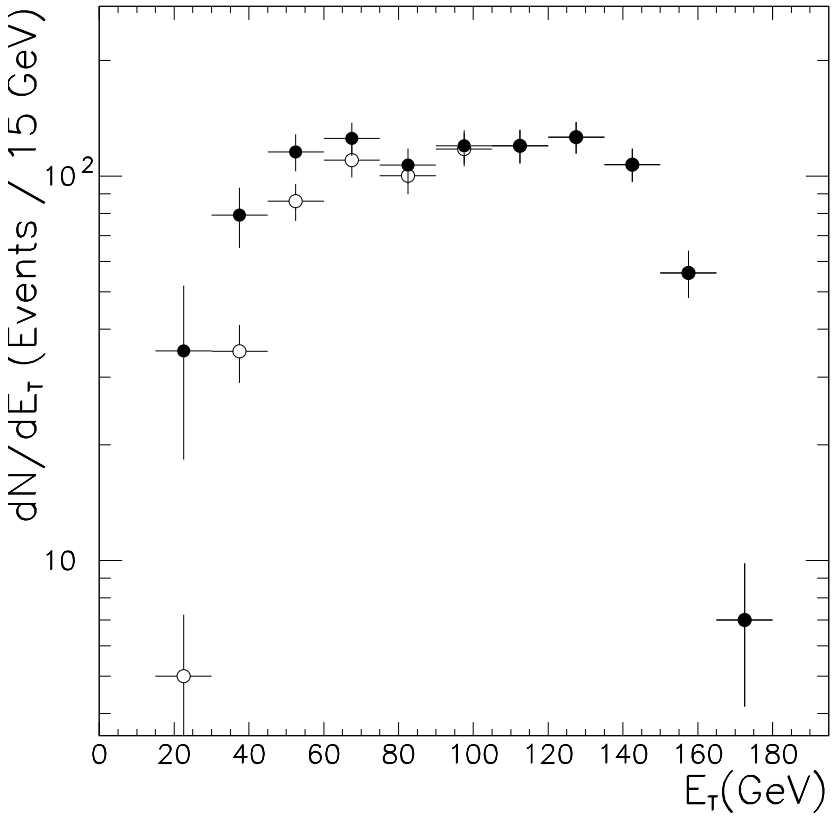

Figure 6.2: *E_t distribution for 1995 data: the white circles correspond to double blade information, the black ones to single blade information*

variable it is possible to select given ranges of b, the higher centrality corresponding to lower impact parameter.

Whichever global variable is chosen to estimate the impact parameter, it is useful to introduce another geometrical variable, which is the average path L of the produced charmonium (or Drell–Yan pair) through nuclear matter, see fig. 6.1. This variable L is more useful than b, or than a global variable like E_t, to compare the charmonium production in different systems. L depends on the impact parameter b and can be calculated using a simple geometrical model.

6.2.1 Centrality selection in E_t bins

The E_t distribution used for the analysis of the data taken in 1995 Pb run is plotted in fig. 6.2. In this figure the E_t distributions in the case of standard target identification system (signal coming from both blades placed left and right behind each target) an in the case in which only one blade is used, are shown. It is clear that the double blade identification system is fully efficient only for (semi–)central

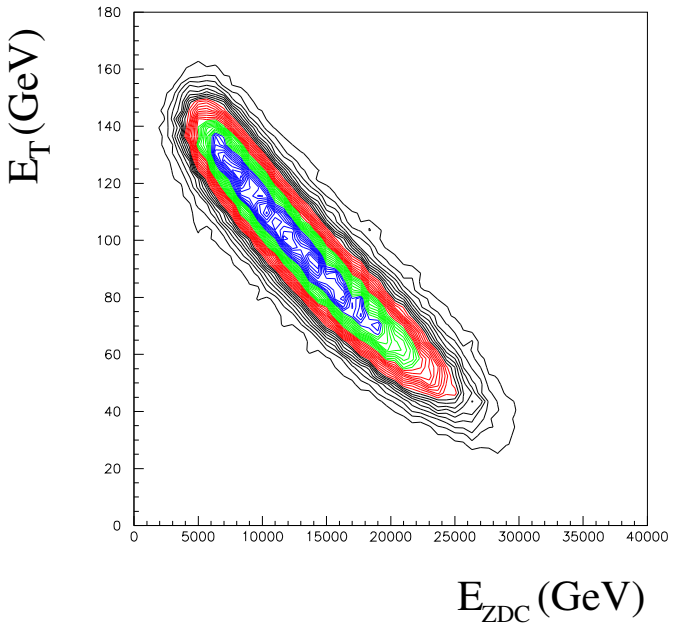

Figure 6.3: *E_t vs E_{ZDC} for events with identified target (1996 data)*

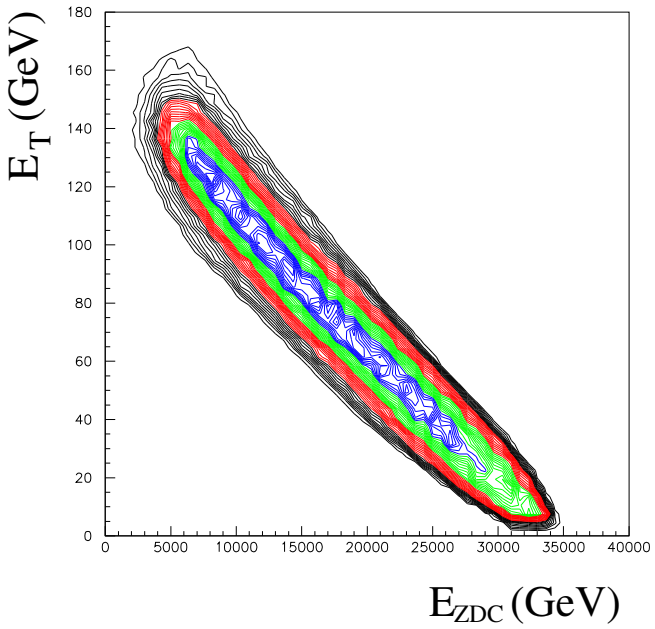

Figure 6.4: *E_t vs E_{ZDC} with the graphic cut (1996 data)*

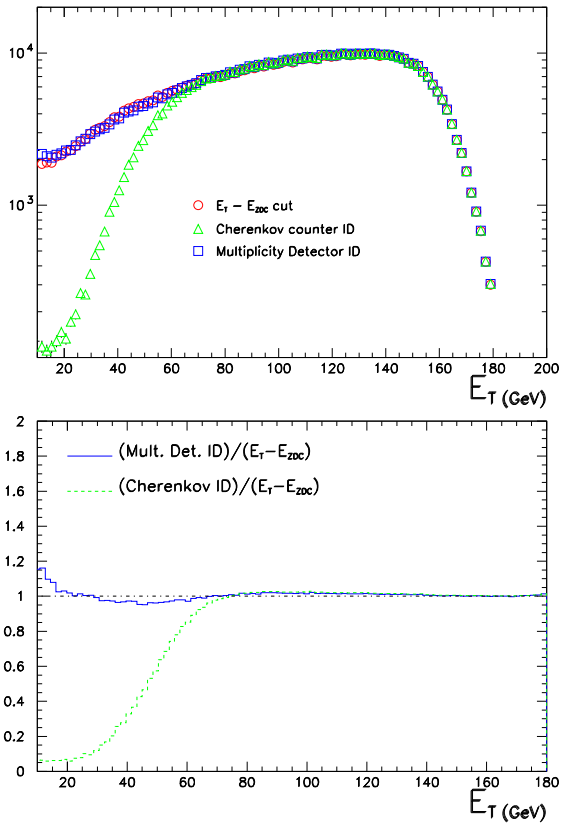

Figure 6.5: *E_t distribution for different event selection methods, and ratio between the different curves.*

interactions, while for peripheral ones we need to rely on the single blade events to gain statistics ($\approx 65\%$ of events are single blade ones in the peripheral bins).

Another way to understand if the interaction took place in the target, is to look at the relation between the transverse energy and the forward energy. If we plot the distribution in which we select only the events in which the target has been identified, see fig. 6.3, it is clear that peripheral events (the ones with very low E_t are discarded). This loss was greater in the 1996 run because the increased number of δ rays (due to thicker subtargets) affected the performance of the quartz blade algorithm.

Considering the fact that the correlation seems to be good even for peripheral events, it was decided to apply an empiric contour cut to data without requiring explicit target identification.

The cut excludes events with E_t less then 5 GeV and events out of the correlation area, see fig. 6.4, and selects any event with E_t and E_{ZDC} inside the main correlation region.

An alternative method to test the efficiency of the contour cut is the MD target identification algorithm. Looking at the E_t distribution in the 3 cases, see fig. 6.5, it is clear that both the graphic cut and the MD target identification algorithm are

more efficient for peripheral events. The similarity of the distribution for these two methods confirms that the contour cut, even if very empiric, is able to select "good" events.

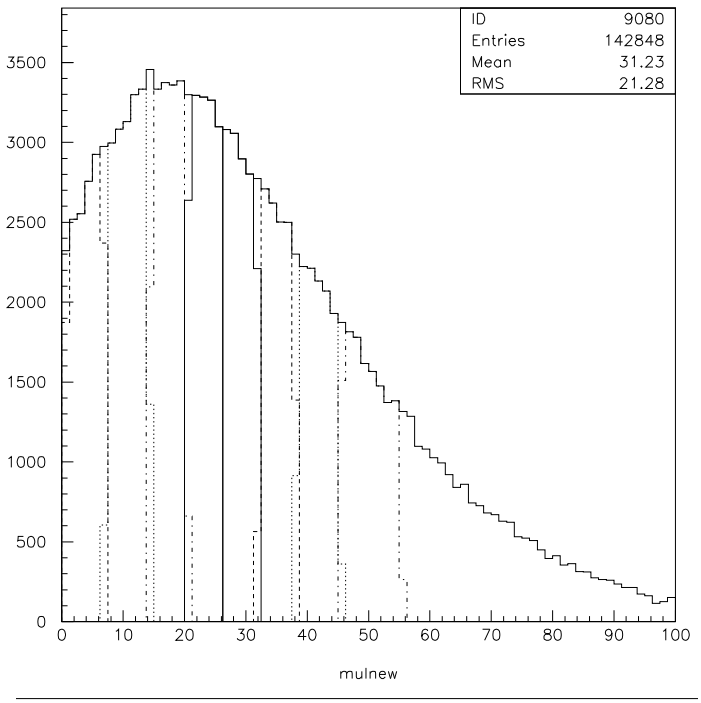

Figure 6.6: *Mul2 distribution and bin selection*

6.2.2 Centrality selection in multiplicity bins

The multiplicity global variable chosen for this analysis is MDMUL2. This choice is due to the fact that to evaluate MDMUL2 only the inner crown of MD1 has been used, and MD1 turned out to be the most efficent of the 2 MD planes. The multiplicity distribution has been corrected subtracting the δ rays contribution, which turns out to be important for low values of MDMUL2. Since the mean value of the δ ray multiplicity distribution is 12, we subtracted 12 to the MDMUL2 variable. The resulting distribution of MDMUL2 is shown in fig. 6.6, where the vertical lines represent the multiplicity bin limits.

In tab. 6.1 the limits of the bins and the numbers of fitted J/Ψ, Ψ' and DY pairs for each bin are reported (the fit procedure is explained in the next section).

Our purpose is now to correlate the multiplicity variables with the geometry of the collision, namely with the impact parameter b. In order to do that we used a minimum bias sample of data, since in this case, if we assume that the impact

Bin	bin limits	$< M >$	$N_{J/\Psi}$	$N_{\Psi'}$	N_{DY}
1	0-7	3.8	15839	156	605
2	7-14	10.8	18209	135	829
3	14-20	17.2	15889	107	944
4	20-26	23.2	15280	88	822
5	26-32	29.2	13165	105	790
6	32-38	35.1	11754	58	738
7	38-45	41.6	11108	91	669
8	45-55	50	11914	94	803
9	¿ 55	70	19762	78	1440

Table 6.1: Multiplicity bins, average multiplicity and different contributions to the signal

parameter b is a monotonic function b(m_{ch}) of the charged multiplicity m_{ch}, we can write:

$$\int_{m_{ch}}^{m_{ch,max}} \frac{d\sigma}{dm}\, dm = \int_0^b \frac{d\sigma}{db}\, db = \pi b^2 \tag{6.1}$$

from which, by inversion we get:

$$b(m_{ch}) = \left[\frac{1}{\pi}\int_{m_{ch}}^{m_{ch,max}} \frac{d\sigma}{dm}\, dm\right]^{\frac{1}{2}} \tag{6.2}$$

As a first step we extracted from the minimum bias data sample a multiplicity distribution, and then we converted it into a differential cross section $\frac{d\sigma}{dm}$, given as a function of charged multiplicity, as shown in Fig.6.7.

That was done by using a proper normalization factor, given by:

$\frac{1}{N_{Pb}N_t} = 1.26\,10^{-28} cm^2 = 1.26\,10^{-2} fm^2$ where,

$N_{Pb} = 201891$ is the number of triggers in the selected minimum bias sample;

$N_t =$ number of target nuclei / $cm^2 = \rho N_{Av} l/A = 3.943\,10^{22} cm^{-2} = 3.943\,10^{-4} fm^{-2}$

(l is the total target thickness, ρ the target density, N_{Av} the Avogadro number and A the target mass number).

Then, by integrating this multiplicity spectrum from different values of m_{ch}, we obtained, by using formula (6.2), the function b(m_{ch}) that is shown in fig.6.8.

From this curve we extracted the values of b corresponding to the average values of the multiplicity in the bins used for our charmonium analysis.

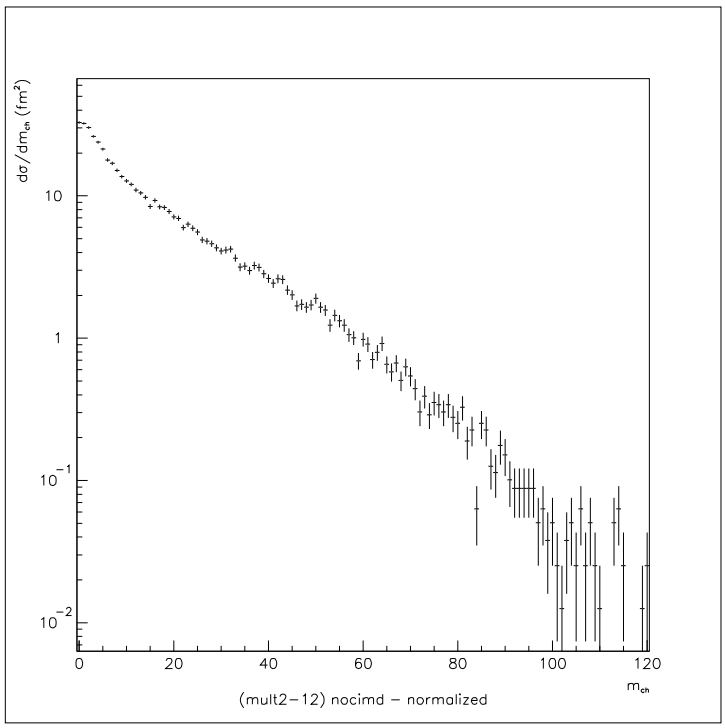

Figure 6.7: Differential cross section versus multiplicity

To test the accuracy of this procedure, a comparison with events generated using VENUS has been performed: in fig. 6.9 the distribution of simulated multiplicity versus b is plotted together with the result of our procedure. The resulting $b(m_{ch})$ curve reproduces accurately the shape of the VENUS correlation.

6.3 The dimuon mass spectra analysis

A dimuon invariant mass spectrum is plotted in fig. 6.10.

The dimuon invariant mass is the essential variable which allows us to distinguish among different contributions (sources) to the signal. To extract the strength of the various sources, measured spectra have to be compared to simulated ones, obtained using known characteristics of the sources and Monte–Carlo techniques.

The events are simulated with a program called DIMUJET, and then reconstructed with the same procedure used for the experimental data. At the end of this simulation–reconstruction chain, we obtain the invariant mass spectra separately for each contribution, now reflecting the apparatus acceptance and smearing. The different simulated mass spectra thus obtained will be fitted with analytical functions [4]. The analytical shapes found in this way will be used to fit the measured spectra and extract the contribution of the single processes.

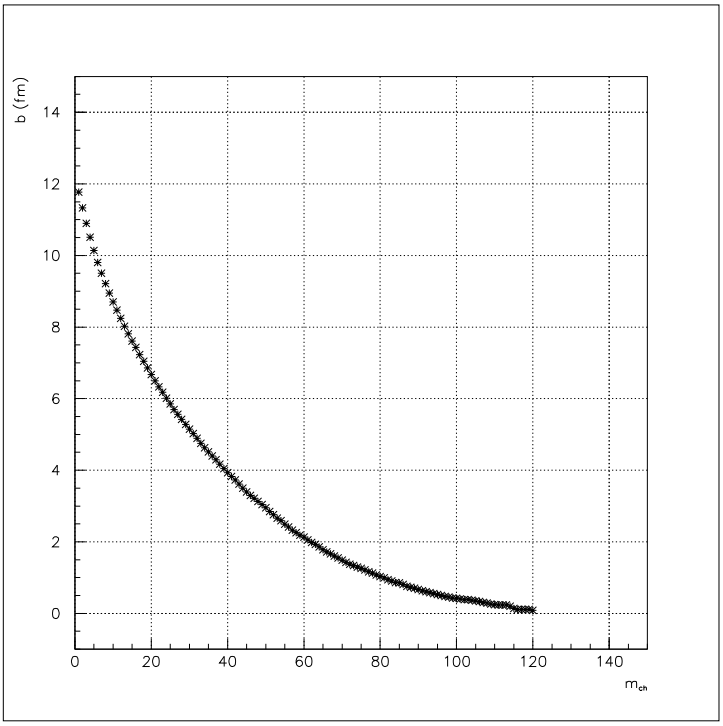

Figure 6.8: Impact parameter b versus multiplicity

The aim of the present analysis is the measurement of the ratio of J/Ψ and Drell–Yan cross sections. The choice of studying ratios and not absolute cross sections is due to the fact that in this way we get rid of systematic errors due to the evaluation of the luminosity of the experiment. In fact, any systematic error on the incoming flux normalization should cancel in the ratio of cross sections, leaving statistical errors as the biggest contribution to final errors. The Drell–Yan process is used as a reference between different systems, because it is not sensitive to the medium in which it is produced, but it is obtained summing over all the elementary nucleon-nucleon interactions. The production cross section of Drell–Yan events is proportional to the AB product, where A is the number of nucleons in the projectile, B is the number of nucleons in the target [3].

6.3.1 Contributions to invariant mass spectrum

The main contributions to the invariant mass spectrum in the region of mass above $2.0 GeV/c^2$ are the dimuon decays of J/Ψ and Ψ', the Drell–Yan pairs and the semileptonic decays of $D\bar{D}$ mesons. In addition a combinatorial background due to pions and kaons decays to muons is present. In the following paragraphs the procedure adopted for the dimuon mass spectra analysis is explained.

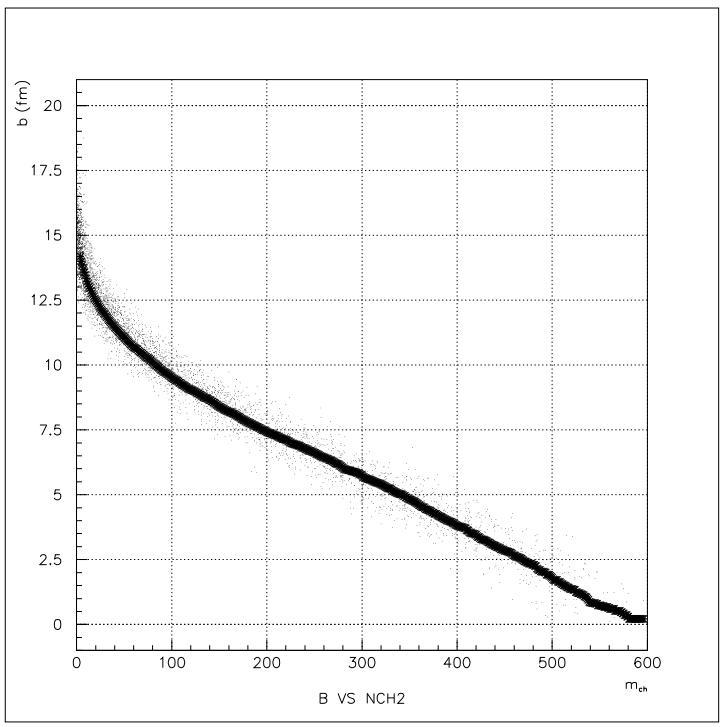

Figure 6.9: Simulated impact parameter b versus multiplicity

Combinatorial Background

The combinatorial background due to pions and kaons in–flight decays is numerically the most important contribution to the "opposite sign" ($\mu^+\mu^-$) low and intermediate mass continuum. Due to the high pion and kaon multiplicity in Pb–Pb interactions, its contribution is still important even in the high mass region up to $3.5 GeV/c^2$, in which the J/Ψ is situated. Therefore a detailed understanding of the background subtraction procedure is essential.

In the present analysis we consider as background all the processes which contribute in equal way to the opposite–sign and to like–sign dimuon spectra. For istance, it can happen that one of the two opposite–sign muons comes from the decay of a $D\bar{D}$ meson, while the other comes from a kaon or pion decay. In this case both opposite–sign and like–sign events will be produced, therefore this will be considered as a background contribution.

The combinatorial background in the $\mu^+\mu^-$ spectra can be estimated by the following combination of like–sign spectra, where the subscript indicates the sign of the spectrometer magnetic field:

$$\frac{dN^{bck}}{dM} = 2R^{bck}\left\{\sqrt{\left(\frac{dN}{dM}\right)^{++}_{\oplus}\cdot\left(\frac{dN}{dM}\right)^{--}_{\oplus}} + \sqrt{\left(\frac{dN}{dM}\right)^{++}_{\ominus}\cdot\left(\frac{dN}{dM}\right)^{--}_{\ominus}}\right\} \tag{6.3}$$

The value of R^{bck} depends on the number of accepted positive and negative

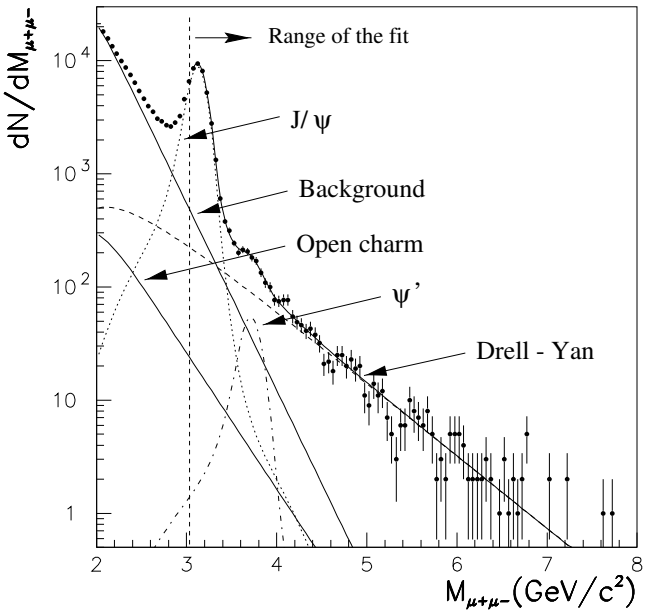

Figure 6.10: *Dimuon invariant mass spectrum and the analitical shapes of the different contributions*

muons. The R^{bck} is expected to be 1 if the parent π and K mesons are (charge) uncorrelated, have poissonian multiplicity distribution and there is no acceptance bias. This last point is ensured by the "image cut" explained in the event selection section, which means that all muon pairs are treated the same way, irrespective of their charges. In fig. 6.11 the four components of the like–sign contributions are shown.

There are two main ways to extract the "signal" distribution from the opposite–sign spectra: the first consists in subtracting background directly using equation 6.3, and is useful to provide a first look to the data, but it has not a good accuracy, since it destroys the poissonian distribution of data. In fact the difference between two Poisson distributions is no longer a Poisson distribution. Moreover, this direct subtraction procedure gives an overestimated signal, since bins with zero events in the $\mu^-\mu^-$ sample but not in the $\mu^+\mu^+$ sample (or viceversa) give zero background. A way to avoid this problem is "smoothing" the like–sign distributions before subtraction, hence fitting them and then subtracting the fitted function from the opposite–sign spectra.

The second method consists in the simultaneous fit of opposite–sign and like–sign distributions.

We chose to use the first method with the "smoothing" of the like–sign distributions before subtraction. This method has many steps: in the first, we fit the like–sign spectra with a functional form, see fig. 6.12, then we proceed fitting step

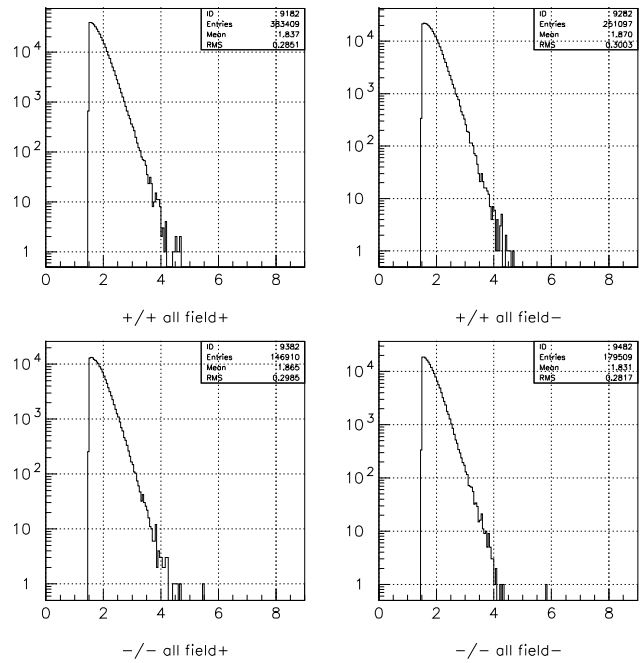

Figure 6.11: *Combinatorial background spectra for the different configurations*

by step the other contributions to the spectra, as explained later on.

J/Ψ and Ψ'

The J/Ψ and Ψ' spectra are described by "pseudo–gaussian" functions, reported in eq. 6.4

$$f(M) = A_0 \times exp\left(-0.5\frac{(M-\mu)^2}{\sigma(M)^2}\right) \tag{6.4}$$

$$\begin{aligned} \sigma &= \sigma_0 && if\ y_1 < M < y_2 \\ \sigma &= \sigma_0(1+[a_1 \times (y_1 - M)^{[a_2 - a_3(y_1 - M)]}) && if\ M < y_1 \\ \sigma &= \sigma_0(1+[a_4 \times (M - y_2)^{[a_5 - a_6(M - y_2)]}) && if\ M > y_2 \end{aligned} \tag{6.5}$$

where y_1=0.97μ, y_2=1.07μ, a_1=2.158, a_2=1.44, a_3=0.44, a_4=1.39 a_5=1.55, a_6= 1.63 for the J/Ψ.

Drell–Yan

The shape of the Drell–Yan distribution is parametrized using the PYTHIA generator which is based on the GRV LO set of structure functions of the colliding nuclei.

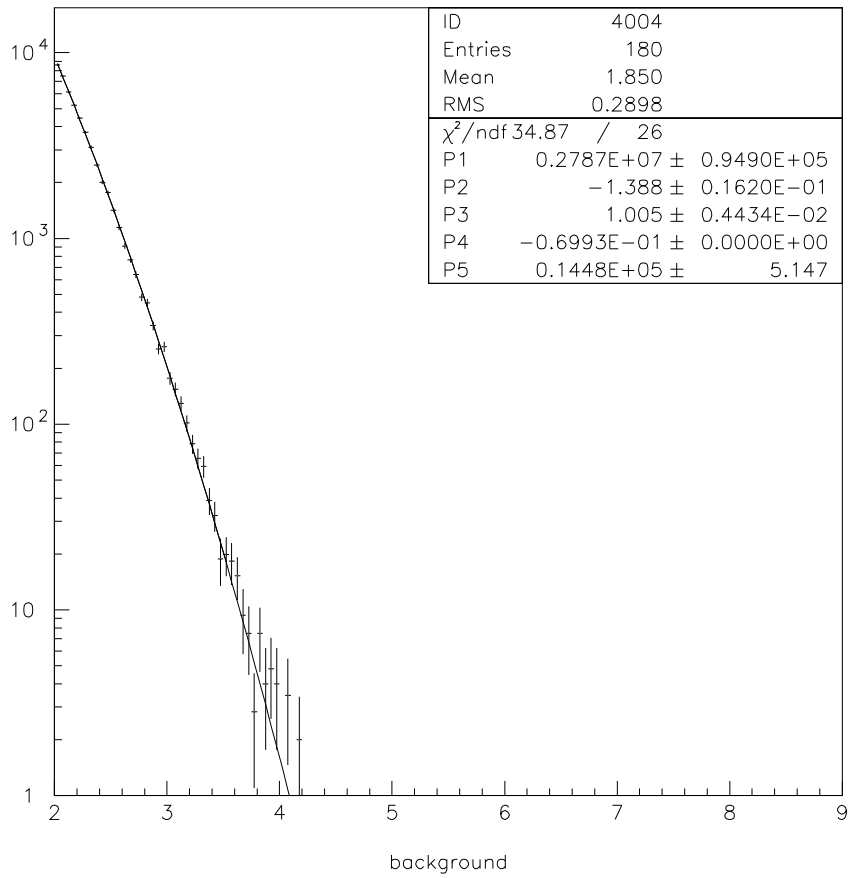

Figure 6.12: *Example of the fit to a background spectrum*

The Drell-Yan process in nucleus-nucleus collisions is simulated supposing a linear dependence on the nucleon-nucleon cross–section, that is neglecting the nuclear effects on the quark distributions. The p-p p-n and n-n interactions are simulated to keep into account the isospin effects of this process. The Drell-Yan continuum can be described for high masses by an exponential function. For a range of mass below 2.5 GeV/c^2 the exponential is attenuated to take into account the spectrometer acceptance. The resulting function is:

$$f(M) = P_1 \times exp(-M \times P_2) - P_3 \times exp\left(-(M - P_4)^2\right) \tag{6.6}$$

where P_1 is determined by a 5 parameter fit in a mass region above $3.05 GeV/c^2$, P_2 =1.463, P_3 =0.2395, and P_4 = 0.5281.

Open charm

The generation of $D\bar{D}$ and its decay in muons is made using PYTHIA and JETSET codes. The form of the function used for the reconstruction of the spectrum is the following:

$$f(M) = P_1 \times exp\left(-0.5 \times \left(\frac{M - P_2}{\sigma(M)}\right)^2\right) \tag{6.7}$$

where

$$\sigma(M) = P_3 \qquad if \quad M < P_5$$

$$\sigma(M) = P_3 \times (1 + P_4 \times (M - P_5)) \qquad if \quad M > P_5 \tag{6.8}$$

where P_1 is determined by a fit in a mass region between 2.2 and 2.6 GeV/c^2, P_2 =1.765, P_3 =0.289, P_4 = 0.5159, and P_5 = 1.456.

6.3.2 The fit procedure

The fit procedure can be divided into 4 steps. In step zero the combinatorial background is subtracted, then the DY normalisation is fixed in a mass region above $3.05 GeV/c^2$ with a 5 parameter fit. The functional form used is the sum of 3 different contribution: the Drell–Yan, the J/Ψ and the Ψ'. Here is the expression of the function used for the fit:

$$\frac{dN^{+-}}{dM} = N_{J/\Psi}\frac{dN_{J/\Psi}}{dM} + N_{\Psi'}\frac{dN_{\Psi'}}{dM} + N_{DY}\frac{dN_{DY}}{dM} \tag{6.9}$$

The result of this step one is plotted in fig. 6.13. At this point we make (step two) another fit to the spectrum in the mass region $2.2 GeV/c^2 \leq M \leq 2.6 GeV/c^2$, to evaluate the contribution of the $D\bar{D}$, see fig. 6.14. Given the "charm-excess" in the intermediate mass region [2], the absolute normalization of the distribution will be left free in the fit procedure, to better interpolate the data. This fit is done using the expression obtained summing $D\bar{D}$, DY and J/Ψ contributions, with only one free parameter, the $D\bar{D}$ normalization, and keepig the contributions of DY and J/Ψ, fixed at the values obtained in the previous step.

The last step (three) is the final fit to the spectrum: fixing $D\bar{D}$ normalisation from the previous step, we leave free the normalisation parameters of DY, J/Ψ and Ψ', and also the mass and the width of the J/Ψ. The function used for the fit is given by:

$$\frac{dN^{+-}}{dM} = N_{J/\Psi}\frac{dN_{J/\Psi}}{dM} + N_{\Psi'}\frac{dN_{\Psi'}}{dM} + N_{DY}\frac{dN_{DY}}{dM} + N_{D\bar{D}}\frac{dN_{D\bar{D}}}{dM} \tag{6.10}$$

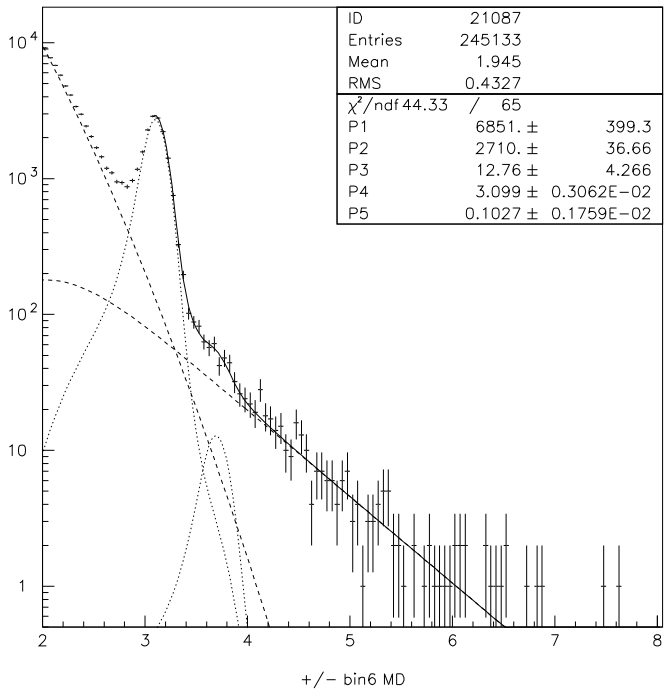

Figure 6.13: *Example of the step one fit to the signal distribution*

In fig. 6.15 the last fit called "global" is plotted.

From this fit we extract the values of the parameters defining the contributions to the invariant mass spectrum of the different processes. Then we use these values to evaluate the number of events corresponding to each process ($N_{J/\Psi}$, $N_{\Psi'}$ and N_{DY}.

6.4 Results

Here I report the results of this analysis: The behaviour of the ratio J/Ψ/DY has been evaluated in different centrality bins and using different target identification algorithms. In the first part I will present the results obtained using the E_t centrality selection, in the second the multiplicity variable is used.

6.4.1 E_t bins

The bins used for the E_t centrality selection are the same already used in preavious NA50 analysis, see tab.6.2.

In fig. 6.16 the comparison between the results obtained with the 2 different event selection methods is plotted: the "banana" cut results are plotted in black dots, the MD selection in open ones. It is evident the difference between the two results in the region of intermediate centrality. At the moment we are still not able

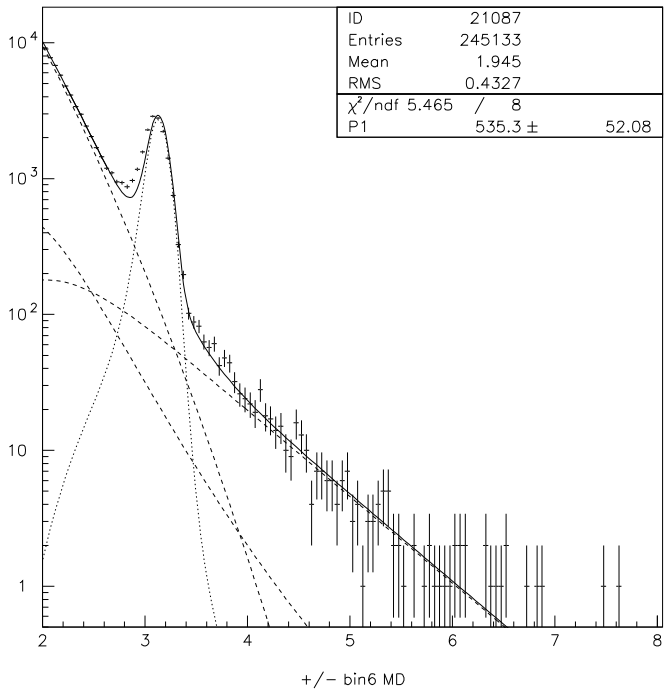

Figure 6.14: *Example of the step two fit to the signal distribution*

to explain this difference which seems to be due only to the different method of target identification. It is still clearly visible a sudden change of slope above 50GeV.

6.4.2 Multiplicity bins

In fig. 6.17 we plot the ratio J/Ψ/DY in 9 multiplicity bins, where as a multiplicity variable we used MULNEW=MUL2-12. In this plot there is no visible difference between the two different method of target identification. Also in this case a change of slope is visible for a multiplicity value of 15. As a control of the fit procedure we report the values obtained in the different bins for the width of the J/Ψ, in the different analisys. In fig. 6.18 the $\sigma(J\Psi)$ is plotted for the E_t analisys, while in fig. 6.19 for the multiplicity bins. Both plots show a common trend in the sense that the width increases for peripheral bins. This can be due to the fact that in peripheral collisions the target identification system has a lower efficiency, and this leads to a greater uncertainty of the J/Ψ mass value.

6.4.3 Comparison with lighter systems

In order to compare our results to the ones obtained by the NA38 collaboration in O-U and S-U collisions at 200GeV per nucleon, it is necessary to relate the centrality variables E_t and N_{ch} to the variable L. Once this has been done we can plot our

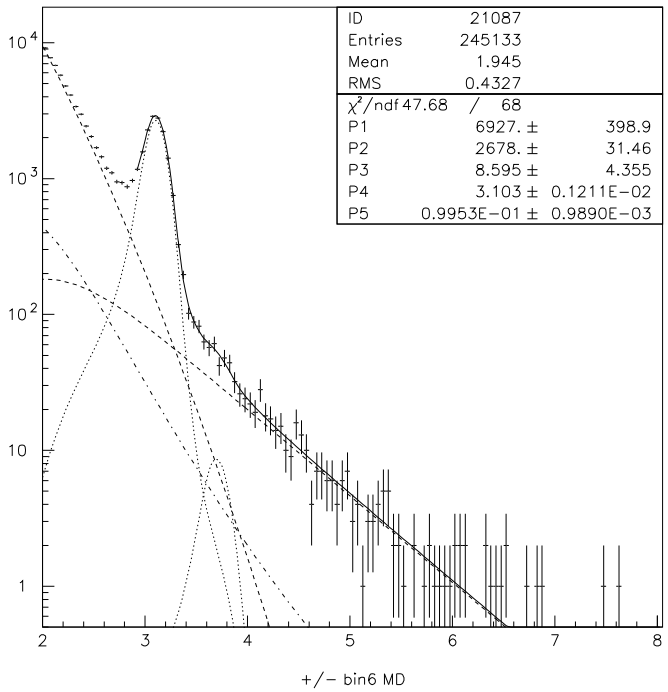

Figure 6.15: *Example of the global fit to the signal distribution*

data together with the NA38 ones, as in fig. 6.20 and 6.21. An exponential fit of the type $\exp(-\rho\sigma L)$ to the NA38 data has been plotted to better evaluate the behaviour of our data. In the first plot we compare the two E_t analysis with the NA38 data. The plot confirms the sharp change in the behaviour of the ratio of J/Ψ and DY cross section, already observed in the E_t bins analysis of 1995 data [1]. The "banana" cut selection actually shows a bigger difference between the fitted line and the Pb-Pb data above L=8fm. In the next plot we compare the NA38 data to the results obtained with the multiplicity centrality selection. Also in this case a change of behaviour is present for $L > 8$fm.

6.5 Conclusions

The NA50 multiplicity detector has been successfully used both as a centrality detector and as a target identificator.

The problems due to radiation damage have been taken into account with a careful evaluation of the efficiency behaviour along the data taking period. The detectors for which the depletion voltage has reached the value of 200 V (limit of the power supply system) will be changed with new ones in the 1998 Pb-Pb run.

The analysis of the ratio of J/Ψ and DY cross–sections using either E_t or multiplicity as a centrality measure shows an anomalous suppression of the J/Ψ production for very central collisions. Further investigations are necessary to better

Bin	$< Et >$	$N_{J/\Psi}$	$N_{\Psi'}$	N_{DY}
1	17	11608	136	300
2	30	8818	100	279
3	40	10820	84	464
4	50	11253	74	558
5	60	9107	84	500
6	70	9507	50	524
7	78	9668	82	535
8	87	9308	37	580
9	96	9300	96	533
10	104	10120	103	587
11	113	7433	15	584
12	123	9884	32	764
13	135	11053	50	774
14	147	6898	66	479
15	161	5539	21	429

Table 6.2: E_t bins, average E_t and different contributions to the signal

understand the small discrepancy measured for peripheral and intermediate centrality bins between different interaction identification methods. A deeper knowledge of the different target identification methods is needed to improve their efficiency and thus the mass resolution of the J/Psi.

The abrupt change of slope of the ratio of J/Psi and DY cross–sections for L values above 8 fm is difficult to be explained in a standard nuclear absorption scenario. Several theoretical interpretation of this result have been proposed in the last year.

Some authors try to explain the anomalous suppression observed by NA50 in terms of absorption of the J/Ψ inside the hadron gas due to interactions with the "comovers" (hadrons produced in the interaction with rapidity very close to the J/Ψ's one) [5],[6]. The alternative scenario is the formation of a deconfined phase of matter: for example, the simple model presented in [7] explains the anomalous suppression in terms of QGP, because in Pb-Pb collisions at small impact parameter the energy density is 35% higher than the maximum energy density obtained in S-U interactions, enhancing the probability of plasma formation. The analysis tools based on the multiplicity detector and developed in this work should give a decisive contribution to the understanding of Pb-Pb data from the 1996 and from the forthcoming 1998 run.

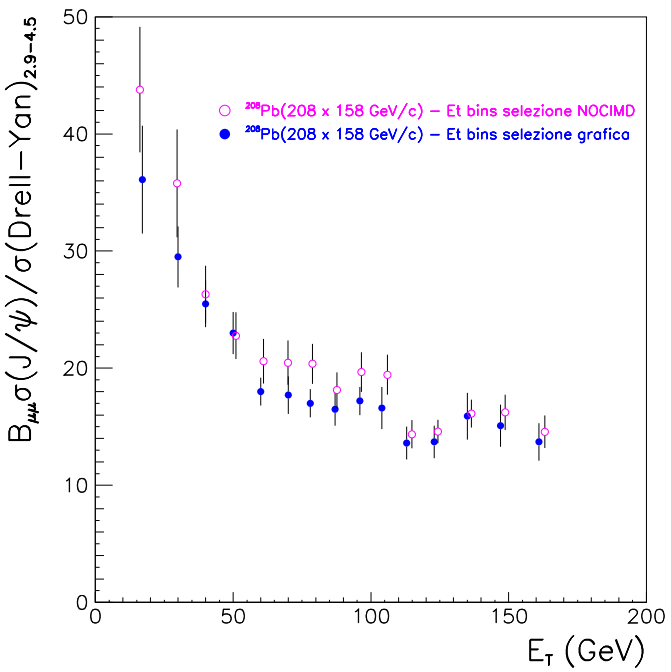

Figure 6.16: *$J/\Psi/DY$ cross sections versus E_t*

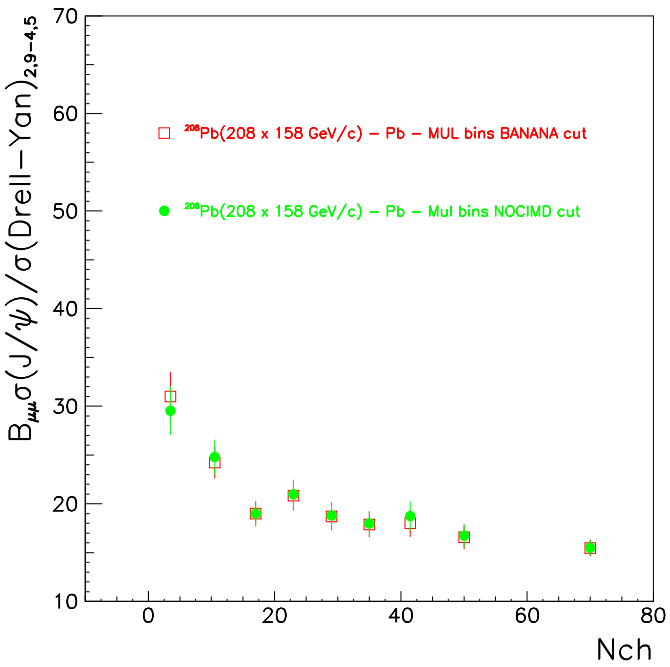

Figure 6.17: *$J/\Psi/DY$ cross sections versus N_ch*

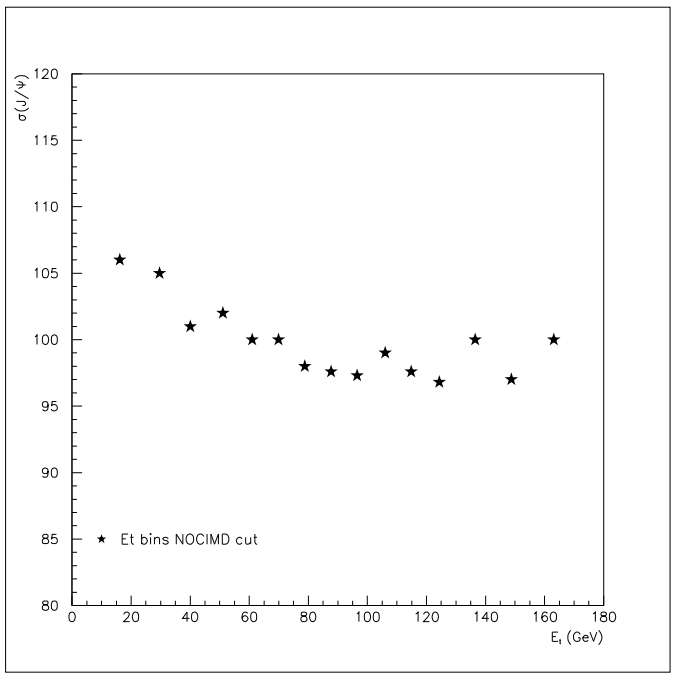

Figure 6.18: *J/Ψ width values for different E_t bins*

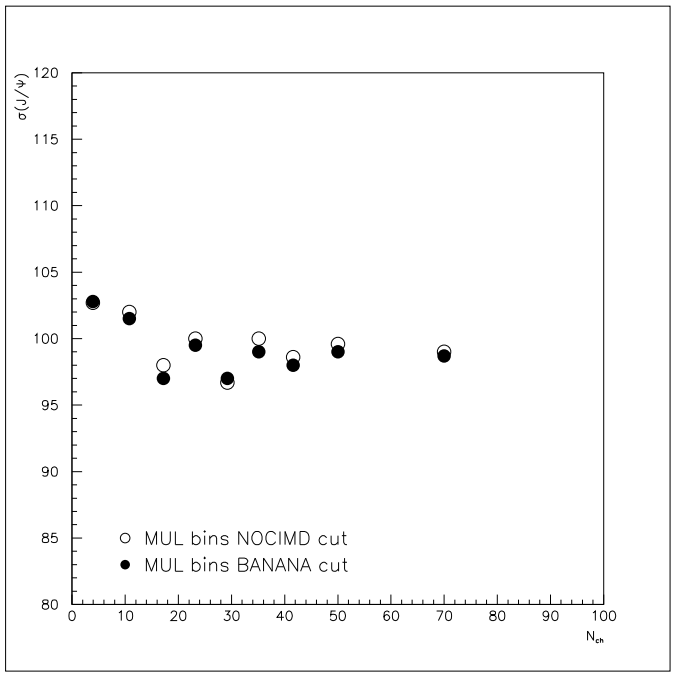

Figure 6.19: *J/Ψ width values for different N_{ch} bins*

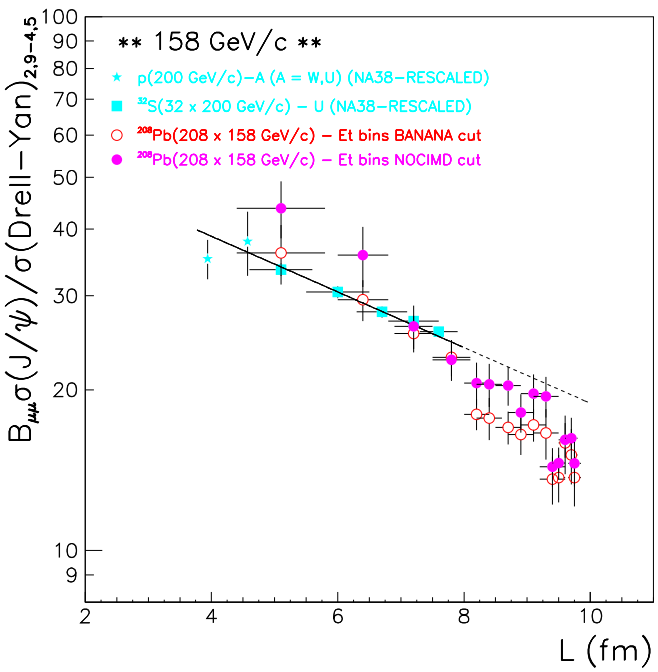

Figure 6.20: *Ratio between J/Ψ and DY cross sections, E_t bin selection and "banana cut" (open circles) and E_t bin selection and NOCIMD cut (black circle), compared to NA38 data*

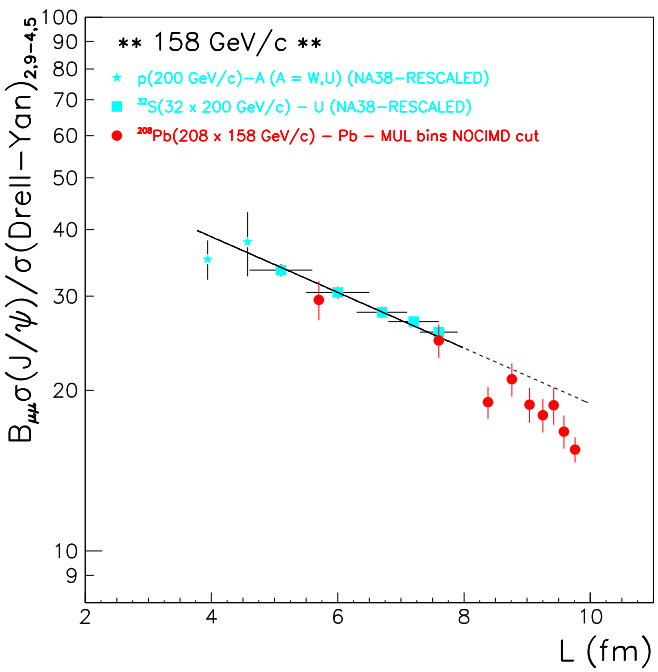

Figure 6.21: *Ratio between J/Ψ and DY cross sections, N_{ch} bin selection and NOCIMD cut (black circle), compared to NA38 data*

Bibliography

[1] M.Abreu et al., Anomalous J/Ψ suppression in Pb-Pb interactions at 158 GeV/c per nucleon, Phys.Lett.B, (1997), 331c-341c

[2] M.Abreu et al., Intermediate mass muon pair continuum in Pb-Pb collisions at 158 GeV/c, Nucl.Phys.A610, (1996), 331c-341c.

[3] F.Fleuret, PhD. Thesis, Ecole Politecnique, Paris, France.

[4] F.Bellaiche, PhD. Thesis, Claude Bernard University, Lyon, France.

[5] S.Gavin and R.Vogt, Phys.Rev.Lett.78,(1996) 1006.

[6] A.Capella et al., Phys.Lett.B393,(1997) 431.

[7] J.P.Blaizot et J.Y.Ollitrault, Phys.Rev.Lett.77,(1996)1703.